Universidade de Brasília
Instituto de Geociências
Programa de Pós-Graduação em Geologia

Efeitos geoquímicos, mineralógicos e petrofísicos de soleiras máficas em rochas reservatório siliciclásticas da Bacia do Parnaíba: implicações para o sistema petrolífero

Dissertação de Mestrado nº 454

Henrique Araújo Lopes

Orientadora: Prof. Roberto Ventura Santos

Brasília – DF
2019.

Efeitos geoquímicos, mineralógicos e petrofísicos de soleiras máficas em rochas reservatório siliciclásticas da Bacia do Parnaíba: implicações para o sistema petrolífero

Henrique Araújo Lopes

Dissertação submetida à Coordenação do Programa de Pós-Graduação em Geologia, Universidade de Brasília, como requisito parcial para obtenção de grau de Mestre em Geologia.

Área de Concentração: Geoquímica

Orientador: Prof. Dr. Roberto Ventura Santos
Co-orientador: Prof. Dr. Carlos Emanoel de Souza Cruz

Banca Examinadora:

Prof. Dr. Roberto Ventura Santos (Orientador IG/UnB)
Prof. Dr. Egberto Pereira (Membro externo - UERJ)
Prof. Dr. Valmir da Silva Souza (Membro interno - Unb)

Brasília-DF
2019

Ficha Cadastral

Lopes, Henrique
Le Efeitos geoquímicos, mineralógicos e petrofísicos de soleiras máficas em rochas reservatório siliciclásticas da Bacia do Parnaíba: implicações para o sistema petrolífero / Henrique Lopes; orientador Roberto Santos Ventura; co orientador Carlos Emanoel Souza Cruz. -- Brasília, 2019.
129 p.

Dissertação (Mestrado - Mestrado em Geologia) -- Universidade de Brasília, 2019.

1. Rochas Reservatório. 2. Hidrotermalismo. 3. Bacia do Parnaíba. 4. Diagênese. I. Santos Ventura, Roberto , orient. II. Souza Cruz, Carlos Emanoel, co-orient. III. Título.

AGRADECIMENTOS

Primeiramente, eu agradeço à empresa ENEVA, à Agência Nacional do Petróleo (ANP), à Fundação de Empreendimentos Científicos e Tecnológicos (FINATEC) e à Universidade de Brasília (UnB) pelo suporte técnico e financeiro para o desenvolvimento desta pesquisa.

Este trabalho é fruto de um projeto de Pesquisa e Desenvolvimento (P&D) realizado pelas instituições e empresas citadas acima. Portanto, sou grato à transição do Regulamento Técnico ANP nº 05/2005 para o nº 03/2015 que tornou mais eficiente a implementação de projetos de pesquisa e desenvolvimento, e contribuiu para o aumento da independência financeira das universidades públicas e para o desenvolvimento científico no Brasil.

Agradeço à CAPES e ao CNPq por terem participado da minha formação acadêmica e pelos investimentos diretos e indiretos na Universidade de Brasília que foram essenciais para o desenvolvimento desta pesquisa. O presente trabalho foi realizado com apoio da Coordenação de Aperfeiçoamento de Pessoal de Nível Superior – Brasil (CAPES) – código de financiamento 001. Estes órgãos que são de suma importância para a produção científica brasileira foram alvos da inconstitucional PEC 95 e estão sendo alvo de cortes direcionados e inescrupulosos pelo atual governo em nome de um projeto ideológico que presa pela ausência de pensamento crítico. Pensamento este que fundamenta todas as áreas da ciência e nos permite crescer não só na ciência, mas como sociedade. Esta pesquisa foi realizada graças aos investimentos e políticas públicas anteriores a este período em que houve uma ampliação, estruturação e melhora na qualidade das universidades públicas. As universidades públicas são uma amostra que boas políticas públicas podem ajudar a romper barreiras de desigualdade social no Brasil. Por meio da ampliação dos investimentos, políticas de cotas sociais, raciais e auxílios aos alunos, as universidades públicas mudaram o perfil dos alunos que a integram, agregando as porções mais marginalizadas da sociedade brasileira. As universidades públicas brasileiras exercem papéis fundamentais em diversos setores extremamente carentes e problemáticos da sociedade brasileira, como: educação, saúde, desenvolvimento tecnológico, economia, entre outros. Elas são responsáveis por quase que a totalidade da produção científica brasileira, formam profissionais para a sociedade, atuam em projetos de extensão prestando assistência direta e indireta a sociedade, e ainda tem o papel social de educação para a maior parcela da sociedade brasileira. Portanto, as universidades públicas brasileiras devem ser defendidas e tratadas como um patrimônio de nossa sociedade.

Quanto às pessoas que participaram desta pesquisa, eu gostaria de agradecer primeiramente aos meus orientadores, Roberto Santos Ventura e Carlos Emanoel Souza Cruz. Aos professores Carlos Jorge Abreu, Farid Chemale Júnior, Nilo Chagas de Azambuja Filho e Paola Ferreira Barbosa pelo suporte dentro do Projeto Poti.

Ao corpo técnico do Instituto de Geociências, que foi de suma importância para o aprendizado teórico e prático associado a cada uma das metodologias utilizadas. Agradeço à Dona Francisca, Isabela Moreno, Iris, Letícia, Matthews e Eduardo. Ao meu companheiro de trabalho e estagiário do projeto Luiz Fernando Tabosa.

Aos meus companheiros de pós-graduação por compartilhar das dificuldades do dia a dia, pelos conselhos imprescindíveis e trocas de conhecimento. Em especial, agradeço àqueles que participaram do Projeto Poti; Ricardo, Valessa e Márcio; e àqueles que, por vezes, deram conselhos não só acadêmicos, mas também pessoais.

Por último, porém não menos importante, à minha família por ter me dado todo o apoio, carinho, educação e formação. Além de ter dado condições extremamente privilegiadas que permitiram que eu sempre pudesse me dedicar ao máximo aos estudos.

RESUMO

Rochas ígneas intrusivas compõem sistemas petrolíferos ígneo-sedimentares atípicos em bacias sedimentares. Na bacia do Parnaíba, as rochas ígneas são responsáveis pela maturação das rochas geradoras, atuam como camadas selantes e formam estruturas de trapeamento. Além disso, este estudo propõe que as rochas ígneas intrusivas e a migração de fluidos hidrotermais a elas associada afetem as rochas reservatório da bacia. A composição mineralógica das rochas reservatório é alterada por uma mineralização autigênica associada à migração de fluidos hidrotermais concentrados em meios permeáveis e limitados por barreiras hidráulicas. Assim, a história diagenética dos sedimentos estudados foi dividida em três fases: 1) soterramento progressivo normal; 2) induzida por mecanismos de transferência de calor e massa associados às rochas ígneas mesozoicas; 3) telodiagenêse. A segunda fase é caracterizada pelas maiores mudanças mineralógicas e químicas dos sedimentos estudados que é marcada pelo aumento na composição modal de clorita, pirita, albita, calcita e óxidos de ferro e sulfetos menores proporções. Esta fase também está associada a formação de três tipos de fraturas hidráulicas. Os dados de geotermometria de clorita geraram dois *plateaus* de temperaturas médias, 150°C ±49 e 250°C ±37, que indicam que as temperaturas máximas anômalas para um contexto de soterramento progressivo apenas. Dados de isótopos estáveis de C, O em calcita e S em pirita em amostras de rochas ígneas e sedimentares sugerem origem predominantemente magmática para estes elementos em ambos os casos. Dados petrofísicos sugerem que houve diminuição da qualidade do reservatório em direção a rocha ígnea e nos níveis em que há maior mineralização autigênica. Com isso, dados petrológicos, geotermométricos e de isótopos estáveis indicam uma assinatura hidrotermal associado aos efeitos das rochas intrusivas nas rochas reservatório. A mineralização induzida por hidrotermalismo preenchem os principais espaços porosos, as fraturas hidráulicas e um melhor entendimento dos processos associados tem aplicações para diminuir os riscos exploratórios e de produção. As sugestões apresentadas neste trabalho podem ser aplicadas aos sistemas petrolíferos atípicos ígneo-sedimentares da Bacia do Parnaíba e demais bacias análogas ao redor do mundo.

ABSTRACT

In many sedimentary basins with hydrocarbon exploration and production, igneous intrusions add some complexity to atypical igneous-sedimentary petroleum systems. In the Parnaíba basin, igneous intrusions generate the main trap and seal structures and trigger organic matter maturation when intruded within source rocks. This study presents petrographic, chlorite geothermometer, stable isotopes (C, O, and S) and petrophysical (K and Φ) analysis on samples collected from a shallow well core (337.5 m) in the Parnaíba Basin. Based on these data and the literature, the diagenetic history of the studied sedimentary sequence was divided into three phases: 1) normal burial diagenesis; 2) heat flow and hydrothermally induced diagenesis; and 3) telodiagenesis. The second phase is marked by a change in bulk mineral composition with an increase in chlorite, pyrite, calcite, illite, albite and minor iron oxides content compared to similar sedimentary interval in the literature. In addition, three types of hydrofracturing structures are described and their non-stratabound interconnection may have implications to increase in reservoir permeability. Temperature formation of chlorite resulted in two average temperature plateaus of 150°C ±49 and 250°C ±37 that are much higher than those expected for progressive burial diagenesis. Stable isotopic data of calcite and pyrite samples collected from sedimentary rocks suggest a major C and S isotopic magmatic source. In conclusion, stable isotope, geothermometry, petrological and petrophysical data shows a hydrothermal alteration fingerprints on reservoir rocks. Discussed petroleum system implications and insights brought by this study can be applied to the Parnaíba basin and analogue basins worldwide with atypical igneous-sedimentary petroleum systems to decrease exploratory and production risks.

Sumário

ÍNDICE DE FIGURAS

1 Apresentação

1.1 Introdução

Este trabalho faz parte do Projeto “Arquitetura deposicional e qualidade dos reservatórios das formações Poti e Cabeças, Bacia do Parnaíba” formulado por um convênio entre a PGN S/A, atual ENEVA S/A, a ANP, a UnB e a FINATEC (Finatec – Projeto 6008/IG/2015). Este projeto é composto, em seu corpo discente, por quatro estudantes de mestrado, três na Universidade de Brasília (UnB) e um na Universidade do Vale do Rio dos Sinos (UNISINOS). O projeto contemplou estudos estratigráficos, de petrografia sedimentar, geotermocronológicos e, especificamente nesta dissertação, caracterização geoquímica, petrográfica e petrofísica dos efeitos das rochas máficas intrusivas nas rochas-reservatório siliciclásticas da Bacia do Parnaíba.

A Bacia do Parnaíba é uma bacia Paleozoica intracratônica situada nas regiões Nordeste e Norte do Brasil que compreende uma área de aproximadamente 600.000 km^2 e tem uma espessura de 3500m em seu depocentro. O registro sedimentar é composto por cinco supersequências, sendo as quatro primeiras depositas durante fases de *sag* e a última durante fase rifte. Dois eventos magmáticos diacrônicos associados à abertura dos oceanos Atlântico Central (ca. 200Ma) e Atlântico Sul (*ca.* 134 Ma) são registrados na bacia como rochas ígneas máficas extrusivas e intrusivas (Vaz et al., 2007).

A complexidade dos sistemas petrolíferos, questões econômicas e logísticas fizeram com que a exploração de hidrocarbonetos na bacia não tenha prosperado até o início deste século. Os estudos relacionados à exploração de hidrocarbonetos na Bacia do Parnaíba se iniciaram na década de 1950 pelo Conselho Nacional do Petróleo (CNP) e sucedidos pela Petrobrás, quando esta foi criada. No início da década de 1980, a ESSO e a Anschutz iniciaram uma campanha exploratória. Até então, nenhuma acumulação comercial de hidrocarbonetos tinha sido descoberta, apenas ocorrências subcomerciais feitas pela

Petrobras. Em 1997, com a criação da ANP, os estudos da bacia foram retomados e desde então foram investidos cerca de US $100 milhões. Foram perfurados 154 poços (93 exploratórios, 49 pioneiros e 12 estratigráficos), além da aquisição de 14.000 km de dados de sísmica 2D, 480 Km^2 de sísmica 3D e dados gravimétricos e magnetométricos (Abelha et al., 2018; Araújo, 2017). O resultado destes estudos foi a descoberta 7 campos de gás (comerciais) com uma reserva recuperável de 27 Bcm que corresponde a 5% de toda a produção de gás natural do Brasil. A produção de gás de 8,4 MM^3/dia abastece usinas termoelétricas que geram 1,4 GW de energia elétrica para abastecer os sistemas norte e nordeste de distribuição de energia (Miranda et al., 2018).

Este aumento nos investimentos na década de 1990 tem ligação com a crescente demanda mundial de energia que consequentemente permitiu a exploração de hidrocarbonetos em sistemas mais complexos, como no caso de bacias afetadas por magmatismo. Acumulações de hidrocarbonetos em bacias com rochas magmáticas foram identificadas em mais de 100 países, porém, poucas bacias desenvolveram produção comercial (Schutter, 2003). As rochas ígneas intrusivas podem afetar os cinco principais componentes de um sistema petrolífero: geração, migração, reservatório, trapa e selo (Senger et al., 2017). Na Bacia do Parnaíba, as rochas ígneas intrusivas têm papel essencial nos principais sistemas petrolíferos atuando como: (1) principal fonte de calor para a geração de hidrocarbonetos (Rodrigues, 1995); (2) principal camada selante da bacia (Miranda et al., 2018); (3) principal formadora de estruturas trapeadoras de hidrocarbonetos (Miranda et al., 2018; Trosdtorf et al., 2018); (4) importantes meios de migração de fluidos (Trosdtorf et al., 2018). Configurando assim, um sistema petrolífero ígneo-sedimentar atípico (Magoon and Dow, 1994a). Quando intrudidas em rochas reservatório, as rochas ígneas impactam a diagênese, geram metamorfismo de contato, compartimentalização do reservatório, e induzem a migração de fluidos hidrotermais (Ahmed, 2002; Brauckmann and Fuchtbauer, 1983; Haile et al., 2019; Rateau et al., 2013). O entendimento destes processos e as alterações das características petrofísicas das rochas reservatório são de suma importância

para melhor previsibilidade da qualidade dos reservatórios e diminuição dos riscos exploratórios e de produção não só na Bacia do Parnaíba, mas em todas as bacias com magmatismo associado.

1.2 Objetivos e Justificativas

Esta dissertação de mestrado tem como objetivo principal caracterizar os processos associados e efeitos na qualidade de rochas reservatório causados por rochas ígneas intrudidas em rochas reservatório. Para isso, foram realizadas análises petrográficas, petrofísica, de química mineral, e de geoquímica de isótopos estáveis. A partir destes dados são discutidos os principais mecanismos de dissipação de calor envolvidos, os principais produtos diagenéticos associados ao hidrotermalismo, a ocorrência de mineralização associada aos fluidos hidrotermais e as principais consequências para o sistema petrolífero.

O tema deste projeto encontra-se em uma das fronteiras mais importantes do conhecimento da exploração de hidrocarbonetos, que é a interação das rochas ígneas com sistemas petrolíferos. No caso dos processos e produtos da influência de rochas ígneas intrusivas em reservatórios, ainda há poucos estudos sobre os mecanismos de dissipação de calor associados a este contexto; diagênese induzida por hidrotermalismo comparada a diagênese por soterramento; e sobre os efeitos das rochas ígneas na qualidade de rochas reservatório sedimentares.

Em geral, estudos sobre os processos e produtos da interação rocha ígnea-rocha sedimentar são mais abundantes acerca de rochas geradoras em relação a rochas reservatório. Na Bacia do Parnaíba, este é um dos primeiros estudos com esta abordagem. Este tema é de suma importância para a redução dos riscos exploratórios em sistemas petrolíferos ígneo-sedimentares. Os resultados e conclusões aqui apresentados se aplicam não só à Bacia do Parnaíba, mas a todas aquelas que apresentam um contexto similar, e podem servir de base para futuros modelamentos dos processos aqui descritos.

1.3 Escopo do Trabalho

Esta dissertação de mestrado está estruturada em quatro seções. A primeira seção consiste na apresentação e introdução ao tema de estudo com os objetivos, justificativas e metodologias deste trabalho. A segunda seção, escrita em língua inglesa, constitui a pesquisa em si, na forma de artigo científico a ser submetido para publicação em periódico científico internacional. Em sequência, a terceira seção contém em forma de tópicos as conclusões demonstradas em detalhe na segunda seção e sugestões para trabalhos futuros. Por último, a quarta seção é composta pelos dados de química mineral de clorita; análises isotópicas de carbono e oxigênio em calcita e de enxofre em pirita.

1.4 Metodologia

O objeto de estudo deste trabalho foi o testemunho contínuo do poço BG-1-MA (337,50m de profundidade), localizado na porção leste da Bacia do Parnaíba, que foi realizado pelo Projeto “Arquitetura deposicional e qualidade dos reservatórios das formações Poti e Cabeças, Bacia do Parnaíba” e encontra-se armazenado no Laboratório de Testemunhos da Universidade de Brasília. O testemunho leva este nome porque foi perfurado no município de Barão de Grajaú, Maranhão. Perfis de raios gama, resistividade e sônico foram executados em toda a sua extensão.

As análises deste trabalho foram realizadas nos laboratórios da Universidade de Brasília, sendo elas: (1) descrição macroscópica; (2) petrografia microscópica; (3) análises quantitativas de composição modal mineralógica QEMScan; (4) análise de química mineral (*Electron Probe Microanalysis - EPMA*); (5) análises petrofísicas – permeabilidade e porosidade; (6) análises isotópicas de carbono, oxigênio em calcita e enxofre em pirita.

1.4.1. Descrição Macroscópica

O testemunho foi descrito macroscopicamente em escala de detalhe (1:40) sendo analisado quanto à textura, composição, estruturas sedimentares, diagênese, estruturas ígneas e granulação. Durante esta etapa, foram configurados álbuns de fotografia de conjunto e de detalhe para registrar fotograficamente as principais feições descritas do testemunho de forma contínua e demonstrativa. Esta etapa direcionou a amostragem para as demais análises posteriores.

1.4.2. Petrografia

Para análise petrográfica, foram confeccionadas 75 lâminas polidas de rochas sedimentares incluindo amostras de contatos superiores e inferiores de rochas sedimentares com soleiras de diabásio. Todas as lâminas foram descritas e fotografadas utilizando o microscópio Zeiss Scope A.1 Axio e o *software* ZEN 2.3 *Blue Edition*. As fotomicrografias foram nomeadas seguindo a seguinte sigla: Nome do testemunho: profundidade_campo_posição dos polarizadores (Nx- polarizadores cruzados e Np- polarizadores paralelos)_número da lente de aumento_principal característica petrográfica (e.g. BG-1-MA_166,00_1_Np_10x_sobrecrescimento de albita em K-Feldspato). Foram analisadas as composições modais do arcabouço, matriz, cimentos e minerais acessórios, as relações texturais e granulométricas visando complementar as análises macroscópicas prévias.

1.4.3. QEMScan

As análises de QEMScan (*Quantitative Evaluation of Materials by Scanning Electron Microscopy*) foram feitas em todas as 75 lâminas petrográficas utilizando o equipamento

QEMScan 650F no Laboratório QemLab na Universidade de Brasília. As condições analíticas foram 15keV de aceleração de voltagem, 9 nA de corrente, e uma distância de trabalho de 13mm. Este tipo de análise utiliza o cruzamento de dados de intensidade de sinal de elétrons retroespalhados e análises de sinal de energia dispersiva de raio-X para a identificação das fases minerais em escala micrométrica. Este tipo de análise foi utilizado para complementar de forma quantitativa a porosidade e a composição modal dos minerais identificados nas análises petrográficas realizadas com microscópio óptico. A identificação dos minerais foi feita com base no banco de dados O&G v 3.7 Sedimentary Rocks SIP, baseado em 1000 contagens e 19 elementos. Dados de composição modal, área superficial de minerais e tamanho de grãos foram determinadas a partir dos dados de porcentagem de área.

Para associar a porosidade aos minerais que ocorrem como arcabouço, matriz e cimento, foram feitas seis combinações de imagens de falsa cor contrastando a composição mineralógica com a porosidade, sendo uma de composição mineralógica total e outras cinco destacando grupos minerais específicos em relação aos demais, sendo eles: feldspatos; carbonatos; cloritas; argilominerais; e óxidos sulfetos.

Problemas analíticos podem ocorrer no caso de partículas menores que 5µm. Neste caso, os problemas podem estar relacionados a análises pontuais insuficientes para uma definição precisa da composição da partícula analisada ou a feixe de elétrons que analisam partículas de níveis abaixo da fase superficial gerando uma mistura de raios X como resposta. Neste caso ou quando os dados de intensidade de sinal de elétrons retroespalhados e análises de sinal de energia dispersiva de raio-X não correspondem aos minerais e elementos presentes no banco de dados utilizado, as partículas/fases minerais são identificadas como minerais não classificados (*unclassified minerals*).

Em todas as amostras, uma porcentagem da área analisada foi composta por partículas /fases minerais não identificados. Considerando que as fases minerais identificadas em análises petrográficas não diferiram das encontradas pelas as análises de QEMScan, as composições modais quantitativas dos minerais identificados foram normalizadas para 100

assumindo-se que as fases minerais não identificadas (*unclassified minerals*) têm composição semelhante e em proporção semelhante às demais fases minerais identificadas.

1.4.4. Análise de Química Mineral & Geotermometria em Cristais de Clorita

Amostras de lâmina polida foram selecionadas e metalizadas com carbono para análise de química mineral de cristais de clorita em microssonda eletrônica. A identificação destes minerais foi feita na etapa de petrografia micrográfica e foram identificados como campos numerados. Devido a diferença de escalas entre as análises de petrografia micrográfica e as de análise de química mineral, foram feitos mapas das lâminas na posição de inserção do equipamento de microssonda eletrônica e os campos foram marcados acima da metalização para que fossem visíveis durante a locação dos pontos a serem analisados.

Cristais de clorita foram analisados em 16 lâminas utilizando a microssonda eletrônica JEOL JXA-8230 SuperProbe com cinco espectrômetros WDS (*wavelength dispersive spectometer*) no Laboratório de Microssonda Eletrônica da Universidade de Brasília. As condições analíticas para cloritas foram de 15kV de aceleração de voltagem, 10nA de corrente de feixe de elétrons, 1 µm de diâmetro do feixe de elétron.

As análises de geotermometria em clorita foram realizadas a partir dos dados de química mineral utilizando o *software* WinCcac, desenvolvido por Yavuz et al.(2015). O *software* WinCcac classifica as cloritas com base em fórmulas com 18 ânions (i.e., $O_{10}(OH)_8$) = 14 oxigênios equivalentes) e estima as porcentagens de Fe_2O_3 e H_2O.

A partir dos dados composicionais e de ocupação dos sítios tetraédricos e octaédricos da clorita, a temperatura de formação de cristais de clorita é calculada por meio de 12 geotermômetros empíricos e os classifica quanto aos minerais do grupo da clorita em diversos diagramas binários e ternários.

De forma pioneira, Cathelineau & Nieva (1985) desenvolveram um método empírico de geotermometria de clorita baseado no posicionamento do alumínio no sítio tetraédrico. A partir

deste método, outros autores o refinaram acrescentando a variação do conteúdo de Fe e Mg que depende da composição da rocha total. Sendo assim, para cada contexto geológico há uma variação da razão Fe/Fe+Mg associada. Além disso, cada estudo tem o seu intervalo de temperatura associado ao contexto geológico em que está inserido. Baseado na variação da razão Fe/Fe+Mg e no intervalo de temperatura associado ao contexto geológico, foram selecionados e utilizados quatro métodos empíricos de geotermometria em clorita que mais se adequaram ao contexto geológico estudado. O intervalo de temperatura associado a este contexto na Bacia do Parnaíba foi baseado no estudo de Cardoso Jr. et al. (2020) que varia aproximadamente entre 123-367°C °C . Três dos métodos empíricos selecionados são baseados na ocupação de alumínio no sítio tetraédrico desenvolvidos por Kranidiotis and Maclean (1987), Cathelineau (1988) e Zang and Fyfe (1995), e um baseado na ocupação de silício no sítio tetraédrico desenvolvido por Kavalieris et al. (1990).

Para estabelecer a temperatura de formação dos cristais de clorita, seguiu-se os critérios propostos por Bourdelle et al.(2013) para que não se analisasse cristais de clorita com contaminação. Estes critérios foram: (1) apenas cristais autigênicos foram analisados; (2) apenas amostras que continham quartzo foram analisadas; (3) a química mineral da clorita deveria ter $K_2O + Na_2O + CaO < 1\%$.

1.4.5 Petrofísica (permeabilidade e porosidade)

Análises de permeabilidade foram feitas utilizando o permeâmetro portátil PPP250 CoreLab no Laboratório de Descrição de Testemunhos da Universidade de Brasília. As análises foram feitas de forma sistemática, aproximadamente, a cada 30 cm, considerando as mudanças de fácies sedimentares, somando um total de 682 amostras. Cada amostra foi analisada de três a sete vezes, e a medida mais representativa foi utilizada.

As análises de porosidade foram feitas utilizando o porosímetro UltraPore 300 e o *software* WinPore no Laboratório de Propriedades Físicas de Rocha da Universidade de Brasília. As amostras (*plugs*) foram preparadas na forma de cilindros de uma polegada de

diâmetro e altura entre uma e três polegadas utilizando coroa diamantada Person Bouquet. Um total de 513 amostras de rochas sedimentares foram coletadas ao longo do testemunho. Após serem coletadas, as amostras foram secas a 40°C durante 24 a 48 horas para eliminar qualquer água retida nos poros. Antes de serem analisadas, as amostras tiveram seus diâmetros e alturas medidos com paquímetro (precisão de 0,01mm), e pesadas em balança de precisão (0,01g). Estes dados foram utilizados como dados de entrada no *software* WinPore para o cálculo de dados de volume, densidade e porosidade. Os dados de permeabilidade e porosidade foram utilizados para o cálculo de parâmetros petrofísicos como índice de qualidade de reservatório (*Reservoir Quality Index -RQI*), índice de porosidade normalizado (*Normalized Porosity Index – NPI*) e indicador de zona de fluxo (*Flux Zone Indicator – FZI)*. Amaefule et al. (1993) definiu o índice de qualidade de reservatório (RQI) como:

$$RQI = 0.0314\sqrt{\frac{k}{\Phi}} \ ; \tag{1}$$

O indicador de zona de fluxo ou porosidade normalizada (NPI ou Φ_z) é definido como:

$$NPI(\Phi_z) = \frac{\Phi}{1-\Phi} \quad ; \tag{2}$$

Ambos parêmetros são úteis para a análise quantitativa e relativa da variação das propriedades de porosidade e permeabilidade. O indicador de zona de fluxo (FZI) fornece informações sobre as diferentes estruturas de geometria de poro considerando textura e mineralogia e é definido pela equação:

$$FZI = \frac{RQI}{NPI} \tag{3}$$

Considerando que a produtividade total de um poço corresponde a combinação linear de cada zona de fluxo, Siddiqui et al. (2003) propôs que a soma dos parâmetros RQI normalizados da base para o topo do poço fornecem uma comparação adequada em um gráfico de soma cumulativa dos índices de qualidade de reservatório normalizados pela profundidade do poço. Neste gráfico, zonas de propriedades semelhantes são caracterizadas por linhas retas dentro de um certo intervalo de profundidade em que a inclinação da reta indica a qualidade do reservatório. A inclinação da reta é inversamente proporcional a

qualidade do reservatório. Ou seja, quanto maior a inclinação da reta, pior a qualidade do reservatório.

Diferentes zonas de fluxo dentro de um intervalo de profundidade são marcadas por mudanças bruscas na inclinação da reta. A soma cumulativa dos índices de qualidade de reservatório normalizados é definida pela equação:

$$RQI_{nc} = \frac{\sum_{x=1}^{i}\sqrt{\frac{k_i}{\Phi_i}}}{\sum_{x=1}^{n}\sqrt{\frac{k_i}{\Phi_i}}} \quad ; \qquad (4)$$

Em que,

i: número de dados em etapas sequenciais de um cálculo;

n = número total de dados;

x = 1.

1.4.6 Isótopos Estáveis de Carbono, Oxigênio e Enxofre

Análises de espectrometria de massa de razão isotópica (*Isotopic Ratio Mass Spetrometry* – IRMS) de carbono ($^{13}C/^{12}C$) e oxigênio ($^{16}O/^{18}O$) foram realizadas em 15 amostras de veios e cimentos de calcita. Foram determinados também a composição isotópica de enxofre ($^{34}S/^{32}S$) em 17 amostras de veios e cimentos de pirita. Estes dados foram gerados no Laboratório de Geocronologia da Universidade de Brasília. As amostras foram pulverizadas utilizando-se broca odontológica diamantada Carbide (tamanhos 4 a 8) acoplada a um MicroMotor Beltec LB 3000 nos mesmos intervalos em que foram feitas lâminas petrográficas, a fim de relacionar os dados isotópicos aos de textura e hábito das amostras de calcita e de pirita descritos na etapa de microscopia ótica.

Amostras de veios e cimentos de calcita coletadas, pesando aproximadamente 500µg, foram armazenadas em tubos de ensaio com tampa rosqueável com septos emborrachados para serem introduzidas no espectrômetro de massa. As amostras foram analisadas quanto ao CO_2 liberado por meio de ataque da amostra com ácido fosfórico ($H3PO_4$) concentrado

utilizando-se o espectrômetro de massa de fluxo contínuo e fonte gasosa com setor magnético DeltaVPlus acoplado ao acessório Thermo Gas Bench II, um sistema de injeção de gás em ciclo repetitivo. As amostras introduzidas no espectrômetro passam por três agulhas cromatográficas. Na primeira, gás hélio é injetado dentro do frasco com amostra para retirar interferentes atmosféricos. Na segunda, ácido fosfórico (H_3PO_4) é injetado para extrair CO_2 da amostra. Na terceira agulha cromatográfica, o gás gerado é coletado e enviado para uma coluna cromatográfica de purificação por meio do fluxo contínuo de hélio, eliminando vapores d'água e gases indesejados. As massas 44, 45 e 46 de CO_2, geradas a partir das diferentes combinações de massas dos isótopos mais abundantes de C e O ($^{12}C^{16}O^{16}O$; $^{13}C^{16}O^{16}O$; $^{12}C^{18}O^{16}O$) são determinadas. As demais massas correspondem a combinações improváveis e insignificantes devido à precisão do método. Os valores de $\delta^{13}C$ e $\delta^{18}O$ são apresentados em per mil (‰) com base no padrão VPDB (Vienna-PeeDee Belemnite) usado para rochas carbonáticas.

Os padrões internacionais NBS18 e NBS19 foram igualmente distribuídos entre amostras. A precisão analítica foi calculada pela média do desvio padrão da medida de 10 ciclos dos padrões, atestando a precisão (reprodutibilidade) e exatidão (acurácia) do equipamento. Foi obtida uma precisão de ±0.06% para os valores das razões isotópicas de $^{13}C/^{12}C$ e ±0.07 para os valores de $^{18}O/^{16}O$, para as amostras contendo no mínimo 100µg de carbonato de cálcio.

Amostras de veios e nódulos de cimento de pirita foram pulverizados e pesados, entre 300 e 400µm, e misturadas com pentóxido de vanádio em cápsulas de estanho. As amostras e padrões (NZ1, S-2, S-3, SO-5, SO-6, CdS e GF1) foram intercalados de forma sistemática. As amostras e padrões foram introduzidos no analisador elementar (TC/EA) Thermo Scientific Flash 2000 utilizando amostrador automático Thermo Scientific MAS 200R. Uma vez no TC/EA o enxofre presente na amostra é convertido em SO_2 por combustão dinâmica em atmosfera de oxigênio e a uma temperatura de 1020ºC. Os produtos gasosos da combustão são então carreados por um fluxo de gás hélio através do trióxido de tungstênio (catalisador

de combustão) e em seguida reduzidos por fios de cobre de alta pureza. A água é removida por uma armadilha de perclorato de magnésio. O SO_2 é separado por uma coluna cromatográfica empacotada a uma temperatura isotérmica. O SO_2 resultante é então enviado para a fonte de íons do Thermo Scientific MAT 253 IRMS, onde é ionizado e acelerado. As espécies gasosas de massas diferentes são separadas em um campo magnético e em seguida são medidas por um arranjo de coletores do tipo copos de Faraday. Para o SO_2, as massas 64, 65 e 66 são monitoradas pelas mesmas razões citadas anteriormente para o carbono e oxigênio. O processamento dos dados assim como o controle do espectrômetro de massa e seus periféricos são realizados pelo software Isodat 3.0, que garante a qualidade analítica dos dados e o monitoramento dos parâmetros durante a análise. Os dados puros das amostras foram corrigidos pelo fator de correção entre os valores de $\delta^{34}S$ das amostras padrões e os seus respectivos valores tabelados (Craig, 1957). Os resultados de $\delta^{34}S$ estão apresentados em unidade por mil (‰) com base no padrão Canyon Diablo Troilite (CDT) e o erro analítico foi de ±0.2‰.

2. GEOCHEMICAL, MINERALOGICAL AND PETROPHYSICAL EFFECTS OF BASIC SILLS ON SILICICLASTIC SEDIMENTS OF THE PALEOZOIC PARNAÍBA BASIN: IMPLICATIONS TO PETROLEUM SYSTEMS.

Abstract

In many sedimentary basins with hydrocarbon exploration and production, igneous intrusions add some complexity to atypical igneous-sedimentary petroleum systems. In the Parnaíba basin, igneous intrusions generate the main trap and seal structures and trigger organic matter maturation when intruded within source rocks. This study presents petrographic, chlorite geothermometer, stable isotopes (C, O, and S) and petrophysical (K and Φ) analysis on samples collected from a shallow well core (337.5 m) in the Parnaíba Basin. Based on these data and the literature, the diagenetic history of the studied sedimentary sequence was divided into three phases: 1) normal burial diagenesis; 2) heat flow and hydrothermally induced diagenesis; and 3) telodiagenesis. The second phase is marked by a change in bulk mineral composition with an increase in chlorite, pyrite, calcite, illite, albite and minor iron oxides content compared to similar sedimentary interval in the literature. In addition, three types of hydrofracturing structures are described and their non-stratabound interconnection may have implications to increase in reservoir permeability. Temperature formation of chlorite resulted in two average temperature plateaus of 150°C ±49 and 250°C ±37 that are much higher than those expected for progressive burial diagenesis. Stable isotopic data of calcite and pyrite samples collected from sedimentary rocks suggest a major C and S isotopic magmatic source. In conclusion, stable isotope, geothermometry, petrological and petrophysical data shows a hydrothermal alteration fingerprints on reservoir rocks. Discussed petroleum system implications and insights brought by this study can be applied to the Parnaíba basin and analogue basins worldwide with atypical igneous-sedimentary petroleum systems to decrease exploratory and production risks.

2.1 Introduction

In the last decades, petroleum systems with associated igneous rocks has increased its importance due to the rise in the energy demand and to the many commercial hydrocarbon accumulations discoveries world-wide For instance, Liaohe and Songliao basin, East China (Chen et al., 1999; Liu et al., 2013); Neuquén basin, Argentina (Rodriguez Monreal et al., 2009); Jatibarang basin, West Java (Farooqui et al., 2009); Yurihara field, Northeastern Japan (Mitsuhata et al., 1999); Taranaki basin, New Zealand (Stagpoole and Funnell, 2001); Faroe-Shetland and Rockall Trough basins, North Atlantic (Rohrman, 2007; Schofield et al., 2017); Tunguska basin, Siberia (Svensen et al., 2009); Campos basin, Solimões, Amazonas and Parnaíba basins (Eiras et al., 2003; Miranda et al., 2018). A petroleum system comprises five main elements: 1) a source rock, from which hydrocarbon may be generated; 2) migration of hydrocarbons, which comprises the expelling of hydrocarbons from source rocks and its movement to and within reservoir rocks; 3) reservoir rock, which are porous and permeable rocks where hydrocarbon may accumulate; 4) a trap, an enclosing structure; 5) and a seal, a low permeability surface (Magoon and Dow, 1994). Igneous rocks may directly represent an element or indirectly affect any of the five elements of a petroleum system. Senger et al. (2017) have summarized and pointed out many positive and negative effects of igneous rocks on each component of a petroleum system. On reservoir rocks, igneous intrusions may affect sedimentary rocks diagenesis (Ahmed, 2002; Girard et al., 1989; Haile et al., 2019), thermal history (Aarnes, 2010; Cardoso Jr. et al., 2020), lead to reservoir and source rocks compartmentalization (Holford et al., 2013; Rateau et al., 2013) generate contact metamorphism aureole (Aarnes, 2010; Aarnes et al., 2011b; Miranda et al., 2018; Souza, 2017), and create or reactivate fluid migration medias (i.e. hydrocarbon or hydrothermal fluids) (Bjørlykke, 1993; Einsele, 1982; Rateau et al., 2013).

These effects of igneous intrusions on reservoir rocks are associated with heat transfer by conduction (Barker et al., 1998; Ferry and Dipple, 1991; Wang et al., 2012) and/or heat and

mass flow by convection mechanism (Dutrow et al., 2001; Einsele, 1982; Genthon and Rabinowicz, 1990; Polyansky and Reverdatto, 2007; Taylor, 1977; Wilson et al., 2007). In both cases, physicochemical and petrophysical changes in sedimentary rocks caused by heat flow and mass transfer associated with igneous intrusion causes an authigenic mineralization and a recrystallization of original minerals. These mineralogical changes may affect porosity and permeability of host rocks and consequently affect reservoir quality and cause reservoir compartmentalization (Genthon and Rabinowicz, 1990; Grove et al., 2017; Haile et al., 2019).

In the Parnaíba basin, igneous intrusions occur in stacked geometry and presents a close relationship with the petroleum systems as they trigger the source rock maturity (Rodrigues, 1995) and represent the main seal layers and trap structures when intruded in reservoir rocks (Miranda et al., 2018; Trosdtorf et al., 2018) (Fig1B). The Parnaíba basin atypical petroleum systems present an ideal geological setting to investigate the heat flow and hydrothermal fluid migration processes and its effects on siliciclastic reservoir rocks associated with mafic igneous intrusions. In order to characterize and evaluate processes associated with igneous intrusions effects on reservoir rocks, petrographical, petrophysical, mineral geochemistry, and stable isotopes (C, O and S) data were performed. Used methodology proved to be a useful tool to differentiate burial diagenesis process from hydrothermal-related processes. Integrated petrological, petrophysical, geothermometry and isotopic data analysis were used for a local and regional discussion of possible consequences for petroleum systems. The insights brought by this study can be applied to the Parnaíba basin and analogue basins worldwide with atypical igneous-sedimentary petroleum systems to decrease exploratory and production risks.

2.1.1. Parnaíba basin Geological Setting and Stratigraphy

The Parnaíba basin is a Paleozoic cratonic basin that extends over 600.000km^2 in the north and northeastern regions of Brazil. It has a maximum thickness of 3500m and consists of a sedimentary succession deposited between the Silurian and the Cretaceous that was

crosscut by two different Mesozoic magmatic events. The whole sequence can be divided into five depositional megasequences (Goés and Feijó, 1994; Vaz et al. 2007) (Fig.1).

The Silurian Megasequence of the Serra Grande Group is composed of alternating thin and thick siliciclastic rocks deposited in continental to shallow marine environments. This megasequence comprises the Tianguá-Ipu succession, which is a potential petroleum system (Abelha et al., 2018). However, Rodrigues (1995) shows that although most of the source rocks are mature to overmature, total organic carbon is usually lower than 1%. The second megasequence is represented by the Devonian/Carboniferous rocks of the Canindé Group, which is composed of continental to shallow-marine sedimentary deposits. It comprises the main petroleum systems of the basin, in which the source rocks are the Devonian shales of the Pimenteiras Formation and the reservoirs are siliciclastic rocks of the Cabeças, Longá and Poti formations. The Early Carboniferous/Triassic megasequence is represented by the Balsas Group rocks, which are characterized by continental to shallow marine siliciclastic deposits that mark the desertification of the basin (Vaz et al., 2007). The fourth megasequence comprises delta-lacustrine siliciclastic rocks of the Jurassic Pastos Bons Formation (Cardoso et al., 2017). The fifth megasequence is represented by Eo- to Neocretaceous siliciclastic rocks of the Corda, Grajaú, Codó and Itapecuru formations (Fig.1) (Vaz et al., 2007).

The basin was affected by two Mesozoic mafic magmatic events: the Mosquito Formation event (ca. 201 Ma) which is related to the Central Atlantic Magmatic Province (CAMP) magmatism (Baksi and Archibald, 1997; CPRM, 2015; Fodor et al., 1990; Oliveira et al., 2018); and the Sardinha Formation (*c.* 134-110 Ma) event which is coeval with Paraná-Etendeka and Equatorial magmatisms (Baksi and Archibald, 1997; Fodor et al., 1990; Hollanda et al., 2019; Janasi et al., 2011; Oliveira et al., 2018) (Fig.1A). Both events are mainly composed of mafic rocks, with minor subalkaline composition, and occur as extrusive and intrusive rocks (Oliveira et al., 2018). Igneous intrusions presents parallel, saucer-shaped, planar transgressive and fault block geometries in seismic data (Trosdtorf et al., 2018). Igneous

rocks mainly intrudes the Canindé and Serra Grande groups, but are very rare in the Balsas Group (Vaz et al., 2007) (Fig. 1B).

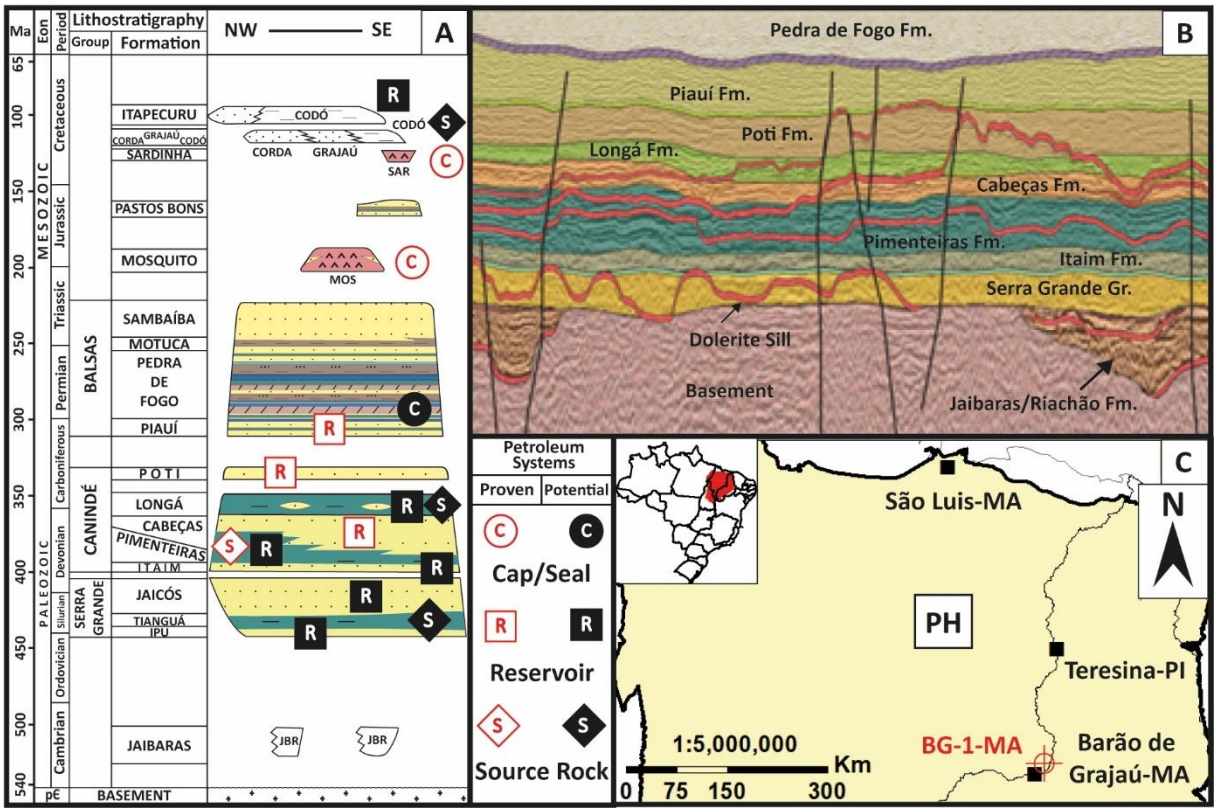

Figure 1. A) Stratigraphic chart of the Parnaíba Basin with the main proven and potential petroleum systems elements, modified from Miranda et al. (2018) and Vaz et al. (2007). **B)** Randomly orientated interpreted 2D seismic line with the lithostratigraphic units represented highlighting sills stacked geometry within the sedimentary sequence. Random orientation of the seismic line may gather non-connected intrusions resulting in false geometries. For further igneous geometry considerations, 3D seismic data should be used, modified from Miranda et al. (2018). **C)** Localization map of the BG-1-MA well and the main producing area, the Park of the Hawks (PH), in the Parnaíba basin at the north-eastern region of Brazil.

2.1.2 Atypical igneous-sedimentary petroleum systems

The main petroleum systems of the Parnaíba basin are related to Devonian shales source rocks of the Pimenteiras Formation and sandstones reservoir rocks of the Poti and Cabeças formations. The Piauí sandstones and the Longá heterolithic sandstones present secondary

reservoirs. (Miranda et al., 2018) (Fig.1 and 2). Mafic igneous intrusions occur preferentially within thick shale layers or along shale-sandstone contact surfaces (Miranda et al., 2018; Trosdtorf et al., 2018). When igneous rocks are intruded into Silurian-Devonian organic-rich layers of the Tianguá, Longá and Pimenteiras formations, they supply heat to trigger maturity of previously immature source rocks. In contrast, when intruded into Devonian-Carboniferous sedimentary siliciclastic rocks of the Cabeças, Longá and Poti formations (Canindé Group), they generate the main seal and trap structures associated with the transgressive behaviour of the sills (Miranda et al., 2018; Trosdtorf et al., 2018).

Five different scenarios of gas accumulation are reported in the Parnaiba basin petroleum systems by Miranda et al. (2018)(Fig. 2). In all scenarios, the Pimenteiras Formation shales are the source rocks and the igneous intrusions have a major role as sealing and trap structures, except for one scenario in which mudstones of the Longá Formation seal and trap the reservoir sandstones of the Cabeças Formation. Miranda et al. (2018) reported that the contact metamorphism formed variable-thickness hornfels aureole beneath the igneous sill, obliterating porosity and permeability owing to quartz overgrowth. The decrease in reservoir quality related to the sealing layer/ trap structures formed by mafic sills were limited and considered of minor importance.

In the Parnaíba basin petroleum systems, different types of heat transfer mechanism may occur because igneous rocks intrude sedimentary rocks with contrasting petrophysical properties (i.e. source and reservoir rocks). When igneous rocks are intruded into low permeability host rocks (e.g. source rocks as shales), the heat is mainly transferred by conduction (Aarnes, 2010). In this case, the thermal effects on host rocks are associated with a contact metamorphism processes (Aarnes, 2010; Holness, 2002; Holness and Isherwood, 2003; Jamtveit, 1992) and overpressure structures as hydrothermal vent complexes (Aarnes et al., 2012; Iyer et al., 2017; Jamtveit et al., 2004) and beefs (Cobbold et al., 2013; Rodrigues et al., 2009). Both overpressure structures are associated with the expansion caused by

hydrocarbon generation (Aarnes et al., 2011a; Jamtveit et al., 2004; Rodrigues et al., 2009; Sydnes et al., 2017)

When intruded in rocks with high porosity and permeability, the igneous intrusions may cause pyrometamorphic contact metamorphism, where partial melt occurs (Bufe et al., 2014; Grove, 2014; Holness, 2002; Holness and Isherwood, 2003), or non-pyrometamorphic contact metamorphism, which involves compaction and hydrothermal process associated with pore water content of the host rock (Aarnes et al., 2011b; Ahmed, 2002; Brauckmann and Fuchtbauer, 1983; Grove, 2014). The last may affect greater volume compared to the first, due to pore water and hydrothermal fluid migration by convection cells along sedimentary strata and/or faults (Bjørlykke, 1994; Duddy et al., 1994; Einsele, 1982; Einsele et al., 1980; González-Acebrón et al., 2011; Holness and Isherwood, 2003; Middleton et al., 2001).

The thermal aureole thickness caused by conduction heat transfer is generally 30 to 250% of the associated igneous intrusion thickness (Aarnes et al., 2010; Barker et al., 1998; Raymond and Murchison, 1988). In contrast, convective heat and mass transfer related to the upward and lateral migration of hot fluids associated with faults and high poroperm layers (aquifers or not) may cause thermal anomalies at distances of up to 10’s of kilometres (Duddy et al., 1994; Genthon and Rabinowicz, 1990; Parnell, 2010). Convective cells may form even in medium with high porosity and permeability anisotropies. In addition, a slight slope of the order of a few percent may favours the occurrence of long convective cells (Genthon and Rabinowicz, 1990). In this case, the heat flow and hydrothermal fluid migration occur through focused medias (e.g. sedimentary stratas, aquifers or faults) and may be limited by previously formed flow baffles (Bjørlykke, 1994; Deloule and Turcotte, 1989; Haile et al., 2019; Wilson et al., 2007).

The transient and episodic heat flow and hydrothermal fluid migration triggered by igneous intrusion may cause the authigenic pore occluding mineralization which may degrade the quality of potential reservoirs (Ahmed, 2002; Holford et al., 2013; Mckinley et al., 2007)and

generate the compartmentalization of reservoirs (Genthon and Rabinowicz, 1990; Grove et al., 2017; Haile et al., 2019).

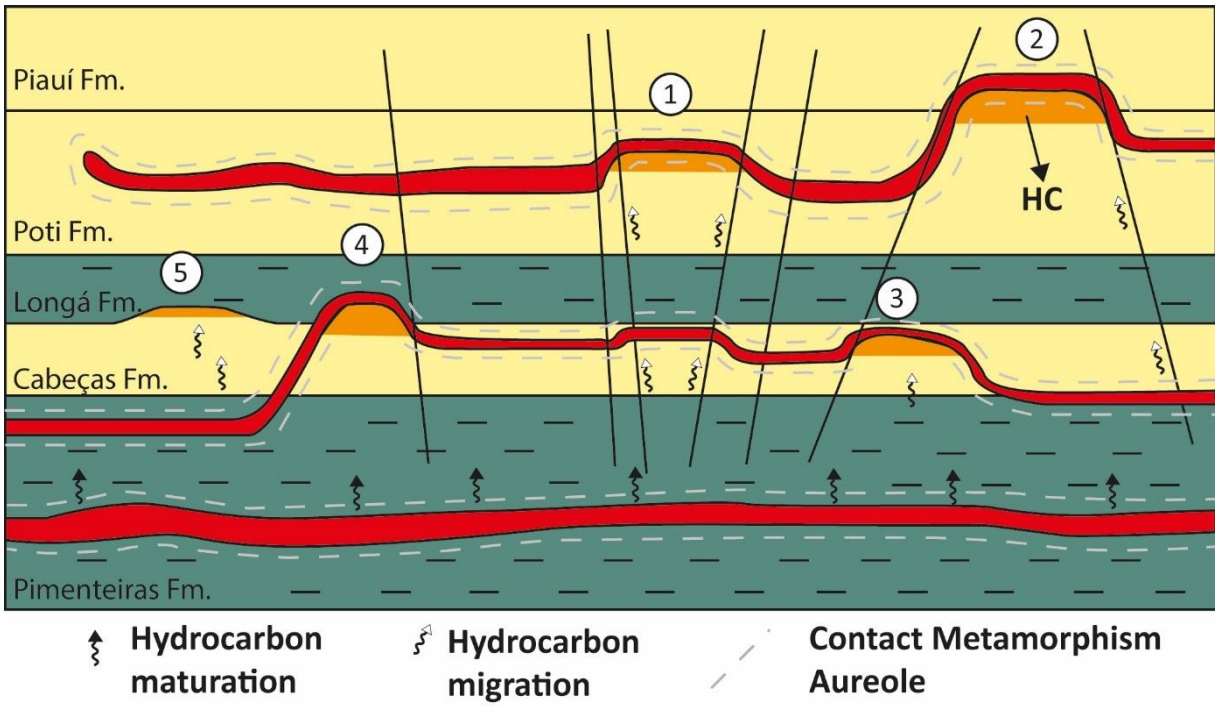

Figure 2. Schematic illustration of the five proven hydrocarbon systems in the Parnaíba basin based on 2D seismic data presented by Miranda et al. (2018). 1) Pimenteiras-Poti system. 2) Pimenteiras-Poti/Piauí system. 3 Pimenteiras-Cabeças system. 4) Pimenteiras-Cabeças/Longá system 5) Pimenteiras-Cabeças system with the Longá Formation stratigraphic sealing.)

In addition, the migration of CO_2 into hydrocarbon-filled reservoirs caused by the magma degassing (Holford et al., 2012) may cause the remigration of previously accumulated hydrocarbons. The heat flow itself from igneous intrusions may increase reservoir temperatures causing hydrocarbon cracking (Cardoso Jr. et al., 2020; Vandenbroucke et al., 1999). Therefore, the recognition and characterization of hydrothermal circulation mechanisms associated with igneous intrusions and its implications to potential reservoir rocks are important to predict reservoir prospectivity in the Parnaíba basin and other analogue sedimentary basins with atypical petroleum systems.

2.2 Sampling and analytical strategy

Samples for this study were collected from the BG-1-MA borehole which was drilled to 337,50m and is located on the eastern region of the basin at the Barão do Grajaú city, Maranhão State (lat 6º43'42,4"; long 43º01'21") (Fig. 1C). The drill core crosscut sedimentary rocks of the Piauí, Poti and Longá formations until it reached a level of dolerite intrusion at the bottom which was drilled for 31m down from sedimentary-igneous rock contact. The core is stored at the core library of the Geosciences Institute of the University of Brasília. Petrophysical logs (gamma-ray, resistivity, self-potential and sonic) were carried out and a detailed macroscopic core description (1:40 scale) was performed regarding grain size, textures, sedimentary and non-sedimentary structures. Core description and the petrophysical logs data were used to make a stratigraphic column (1:800) with stratigraphic cycles and depositional environments.

2.2.1 Petrography, Electron Probe and QEMScan analyses

A total of 75 polished and impregnated with blue resin (blue dyed Araldite) thin sections of sedimentary rocks and of sedimentary-igneous rocks contact samples were prepared at the University of Brasília and analysed using petrographic microscope Zeiss Scope A.1 Axio coupled with a Zeiss Axiocam 105colour. Following these procedures, all the 75 polished thin sections were prepared with a carbon coating and were analysed for the bulk mineralogy analysis mode using a QEMScan 650F at the QemLab of the University of Brasília. The analytical conditions consisted of 15 kV of acceleration voltage, 9nA of beam current and 13mm of work distance. Back Scattered Electrons (BSE) and Energy Dispersive (EDS) X-ray spectra were used to create digital mineral images with mineral identification using the O&G v 3.7 Sedimentary Rocks SIP database, which is based on 1000 counts and 19 elements. QEMScan images represent a link among core description, core petrophysics analyses,

petrography and mineralogy. Modal abundance, particle and surface areas, mineral associations, grain and particle sizes are determined considering the area percent data. Six different false-colour maps were generated to highlight fabric and thin section-scale mineral distributions: total mineral assemblage; feldspars; carbonates; clay minerals; chlorites; and oxides & sulphides. Particle sizes less than 5µm, which were too small to be properly identified by the analytical procedure or have generated mixed BSE and EDS signals were identified as *unclassified minerals*. Since all mineral phases identified in QEMScan bulk composition analyses were the same as those identified in the petrographic work, it was assumed that unclassified minerals may have a similar composition and in similar proportions of those identified in QEMScan analyses. Therefore, total area percent data of all identified minerals were normalized to 100% proportionally reclassifying *unclassified minerals* into identified mineral phases.

Chlorite major element compositions of 16 samples were determined by Electron Probe Microanalysis (EPMA) using a JEOL JXA-8230 SuperProbe Electron Probe Micro of the Geosciences Institute of the University of Brasília by means of a 5-spectrometer analyser. The analytical conditions were 15kV of acceleration voltage; 10nA of beam current; and 1µm of electron beam diameter for chlorite crystals and the count times for peaks and backgrounds for all elements were 10s. Results not constrained between 98 and 102% were discarded.

Chlorite geothermometric data were obtained based on major element composition using four out of the twelve different empirical methods available in the WinCcac software (Yavuz et al., 2015). Considering the geological setting, the Fe/Fe+Mg ratio ranges and the temperature ranges, we have used the methods proposed by Kranidiotis and Maclean (1987), Cathelineau (1988) and Zang and Fyfe (1995), which are based on chlorite tetrahedral Al occupancy (Al^{IV}); and by Kavalieris et al. (1990), which is based on chlorite tetrahedral Si occupancy (apfu). In order to avoid contamination, this study followed Bourdelle and Cathelineau (2015) recommendation to analyse only authigenic material; quartz-bearing samples; and with total $K_2O + Na_2O + CaO$ below 1% wt.

Compositional data were processed using the WinCcac software (Yavuz et al., 2015) that classifies chlorite data based on 18 anions (i.e. $O_{10}(OH)_8$) = 14 oxygen equivalents); estimates the Fe_2O_3 (wt%) and H_2O (wt%) and calculate twelve different empirical chlorite geothermometers. Two to fourteen chlorite crystals were analysed in each sample and each analysis resulted in four geothermometric data (i.e one for each of the selected methods). Average temperature was calculated for each analysis considering the four methods of geothermometric data. Then, an average and standard deviation were calculated for each sample (i.e. thin section) considering the average temperature of each individual analysis of the same sample (i.e. each chlorite crystals in the same thin section) that was previously calculated.

2.2.2 Stable Isotope Analyses

Isotopic ratio mass spectrometry (IRMS) analyses of sulfur isotopes in pyrite and of carbon and oxygen isotopes in calcite were determined at the Geochronology and Stable Isotope Laboratory at the University of Brasília to investigate the source of these elements. A total of 17 sulfur isotope analyses of pyrite and 15 carbon and oxygen isotope analyses of carbonate were performed along the drill core. The samples were collected using a diamond coated dental microdrill bit coupled to a micromotor Beltec LB3000 in depth intervals where thin sections were made in order to integrate both results.

For sulfur isotopic analyses, an aliquot of 300 to 400 µm of each sample was loaded with a similar or higher amount of V_2O_5 in a tin cup that was crimped. Then, the samples were loaded together with international standard samples (NZ-1, S-2, S-3, SO-5, SO-6, CdS and GF1) in an automated continuous flow system consisting of an elemental analyser Thermo Scientific Flash 2000 and a MAS 200P Thermo Scientific IRMS. In this system, the total sulfur of the sample is converted into SO_2 by dynamic combustion and carried by He flush to be analysed by mass spectrometer. Water is removed by a manganese perchlorate trap.

The SO_2 is separated on a gas chromatographic column (GC), and is ionized and accelerated at the ion source of the Thermo Scientific MAT 253 IRMS. The different gas phases are separated by a magnetic field and measured by the Faraday cup collector. Measured $^{34}S/^{32}S$ ratios are obtained by comparing the integrated peak areas of *m* = atomic number 66 divided by *m* = atomic number 64 for the pulses of SO_2 of sample versus the analysed standards. Data processing, IRMS, its coupled equipment control, analytical parameters monitoring during analyses were performed by the Isodat 3.0 software. Raw sample data were corrected using the calibration of measured and standard values of the international standard materials. The $\delta^{34}S$ results are expressed in ‰ based on the Canyon DiabloTroilite standard and the analytical error was of 0.2 ‰.

For oxygen and carbon isotopic analyses, an aliquot of approximately 300 µg of each sample was placed in glass vials that were subsequently submitted to a He flush at 72°C. After flushing, the carbonate aliquots were reacted with concentrated phosphoric acid, and the CO_2 released was analysed for carbon and oxygen isotopes in the continuous flow isotopic ratio mass spectrometer (IRMS). The analyses were performed in a Thermo Fisher Delta V Plus connected to a Gas Bench II. Analyses of the international standards NBS 18 and NBS 19 were carried out alternated with the studied samples. The $^{13}C/^{12}C$ and $^{18}O/^{16}O$ are obtained by comparing integrated peak areas for *m* = atomic number 44, 45 and 46 of the sample CO_2 pulses compared to those for the sample and references gases. The $\delta^{13}C$ and $\delta^{18}O$ are expressed in ‰ based on the VPDB (Vienna-PeeDee Belminte) standard. The analytical precision was of ±0.1% for $^{13}C/^{12}C$ and of ±0.1 for $^{18}O/^{16}O$, calculated by the average of the standard deviation of the analysed standards.

2.2.3 Petrophysics

A total of 513 core plugs of 1-inch (c. 2.54cm) diameter were horizontally drilled from the BG-1-MA core using a diamond impregnated core bit Person Bouquet at the Thin Section and Sample Preparation Laboratory at the University of Brasília. After drilling, core plugs

rounded edges were cut to square edges, resulting in a length range from 0.57 to 1.60 inches (1.45 to 4.05cm). After preparation, samples were washed and then dried in an oven at c. 40°C for 24 to 48 hours in order to eliminate any water from the pores. Prior to analysis, individual core plugs were weighed using a precision balance (precision of 0.01g), and lengths and diameter measured with a high precision calliper (0.01mm). All individual core plugs were analysed for helium porosity at ambient pressure and temperature (20-25°C) using the porosimeter UltraPore 300 in the Rock Physical Properties Laboratory at the University of Brasília. Individual samples were analysed from three to seven times and the most representative value was considered. Pore volume, grain density, grain volume and effective porosity were calculated using the WinPore software.

Horizontal permeability analyses were carried out in 682 samples collected along 300m of the BG-1-MA well core using a portable air permeameter PPP250 Core Lab in the Rock Physical Properties Laboratory at the University of Brasília. Individual samples were analysed from three to nine times and the most representative value was considered.

The permeability (k) and porosity (Φ) data were used to calculate petrophysical parameters of samples. For instance, the Reservoir Quality Index (RQI) expressed in μm ($1x10^{-6}$m) and defined as (Amaefule et al., 1993):

$$RQI = 0.0314\sqrt{\frac{k}{\Phi}}; \quad (1)$$

The Normalized Porosity Index (NPI or Φ_z), is defined as:

$$NPI(\Phi_z) = \frac{\Phi}{1-\Phi}; \quad (2)$$

The Flux Zone Indicator (FZI) gives information about the structure of distinct pore geometrical facies considering texture and mineralogy attributes and is defined from the equation:

$$FZI = \frac{RQI}{NPI} \quad (3)$$

Considering that the total productivity of a well is a linear combination of individual flow zones, Siddiqui et al. (2003) proposed that the summation and normalization of RQI or FZI starting the bottom of the well provide a convenient comparison with the normalized cumulative plot. Zones of similar properties are characterized by straight lines with the slope of the line indicating the overall reservoir quality within a particular depth interval. Changes in the slope divide the reservoir into zones. The higher the slope the worse the reservoir quality. The normalized cumulative RQI is defined from the equation:

$$RQI_{nc} = \frac{\sum_{x=1}^{i}\sqrt{\frac{k_i}{\Phi_i}}}{\sum_{x=1}^{n}\sqrt{\frac{k_i}{\Phi_i}}} \quad ; \tag{4}$$

Where i = number of data points at sequential steps of calculation; n = total number of data; x = 1.

2.3 Results

From the top downwards, drill core BG-1-MA crosscut a sedimentary succession that includes the lower portion of the Piauí Formation (around 50m thick), the Poti Formation (175m thick) and the Longá Formation (75m thick) (Fig.3). The lowermost part of core crosscut about 31m of a dolerite sill. Above the lowermost main sill, there are four thinner splays of igneous intrusions within the Longá Formation sediments. Three are less than 20 cm thick and one is 4.4 m thick (Fig.3). The contact between the sediments of the Longá Formation and the igneous sills are sharp and the sedimentary host rock presents no evidence of partial melting generation. However, discontinuous layers of the Longá and Poti Formation are heavily cemented/filled with calcite, chlorite, illite, albite, sulfides ± oxides and present brittle and rare ductile structures. These authigenic mineral assemblage occur in anomalous contents compared to what is described in the literature for this sedimentary succession interval. Brittle structures are mainly associated with siltstones and mudstones and only occur close igneous

intrusion, whereas the cemented layers are preferably associated with sandstones in alternated levels.

This section will be divided into five subsections. The first is about the mineral composition and depositional environment of the studied sedimentary succession followed by mineralogical and petrographic characterization. The third concerns about chlorite formation geothermometric data and the fourth is composed of stable isotopes of C, O and S results. The fifth and last section presents petrophysical data of the potential reservoir rocks of the studied sedimentary rock interval.

2.3.1 Depositional Environments and Primary Composition of the Sedimentary Sequence

The studied sediments are very fine to medium-grained, moderately sorted ranging from well to poorly sorted. Quartz and feldspars are the most frequent framework components; lithic rock and intraclast fragments rarely occur. Lithic rock fragments in sandstones often occur at the base of sandstone layers deposited over mudstones. They are mainly composed of mudstone intraclasts and rarely of microcrystalline phosphates clasts. Sandstones are mostly subarkoses and arkoses; quartzarenites, sublitharenites and lithic arkoses rarely occur (Folk, 1980; Pettijohn et al., 1973). The Longá and Poti formation sandstones are mostly texturally immature, whereas the Piauí Formation rocks are sub-mature to mature. The Longá and the lower portions of the Poti formations (>130m of depth) sediments are more heterogeneous and thinly bedded (generally < 30cm) compared to the upper portions of the Poti Formation (<130m of depth) and the Piauí formation that are more homogeneous and composed of thicker sedimentary layers (>50cm to 6m) (Fig. 3).

The Longá Formation thin and heterogeneous layers are composed of very fine to fine-grained couplets (mudstone/muddy sandstones to sandstone/muddy sandstones) and

sedimentary structures indicate that they were deposited in shoreface, offshore transition and in deltas under wave and tide environments influence (Fig. 3).

The Poti Formation concordantly overlies the Longá Formation and it is mainly composed of interbedded mudstones and sandstones with subordinated mudstone and intraclastic conglomerate levels. Sedimentary and stratigraphic structures indicate that they were deposited in fluvial-estuarine, tidal deltas, fluvial-deltaic, fluvial and lagoon environments (Fig. 3).

The Poti Formation was divided into six fining- and coarsening-upwards successions that present a maximum flooding surface within it and were limited by sequence limit surfaces (Fig. 3). The lower contact with the Longá Formation is marked by a transitional sedimentary succession (Longá-Poti sequence – LP) below the sedimentary succession I of the Poti Formation. The upper contact with the Piauí Formation was not observed due to core loss. Based on heterogeneity, thickness and change in depositional environments, the Poti Formation was divided into three portions for didactic purpose. The lower portion comprises the sedimentary successions I and II; the middle portion, the sedimentary successions III and IV; and the upper portion, sedimentary successions V and VI (Fig. 3). The Piauí Formation is homogeneous and mainly composed of thick (>3m) pale yellow to brown subarkoses and quartzarenites that are very fine to coarse-grained; mudstones with anhydrite and siltstones rarely occur. Sedimentary and stratigraphic structures suggest that the Piauí Formation sediments were deposited in the fluvial-eolic environment (Fig. 3).

2.3.2. Mineralogy, Petrography, and Diagenetic Aspects

2.3.2.1 Mechanical and Chemical Compaction

Most common textures in the Longá, Poti and Piauí sediments due to mechanical and chemical compaction are tangential-, straight-, concavo-convex and rare sutured intergranular contacts; sediment floating in cement; and plastic ductile grain and intraclasts deformation (Fig. 4).

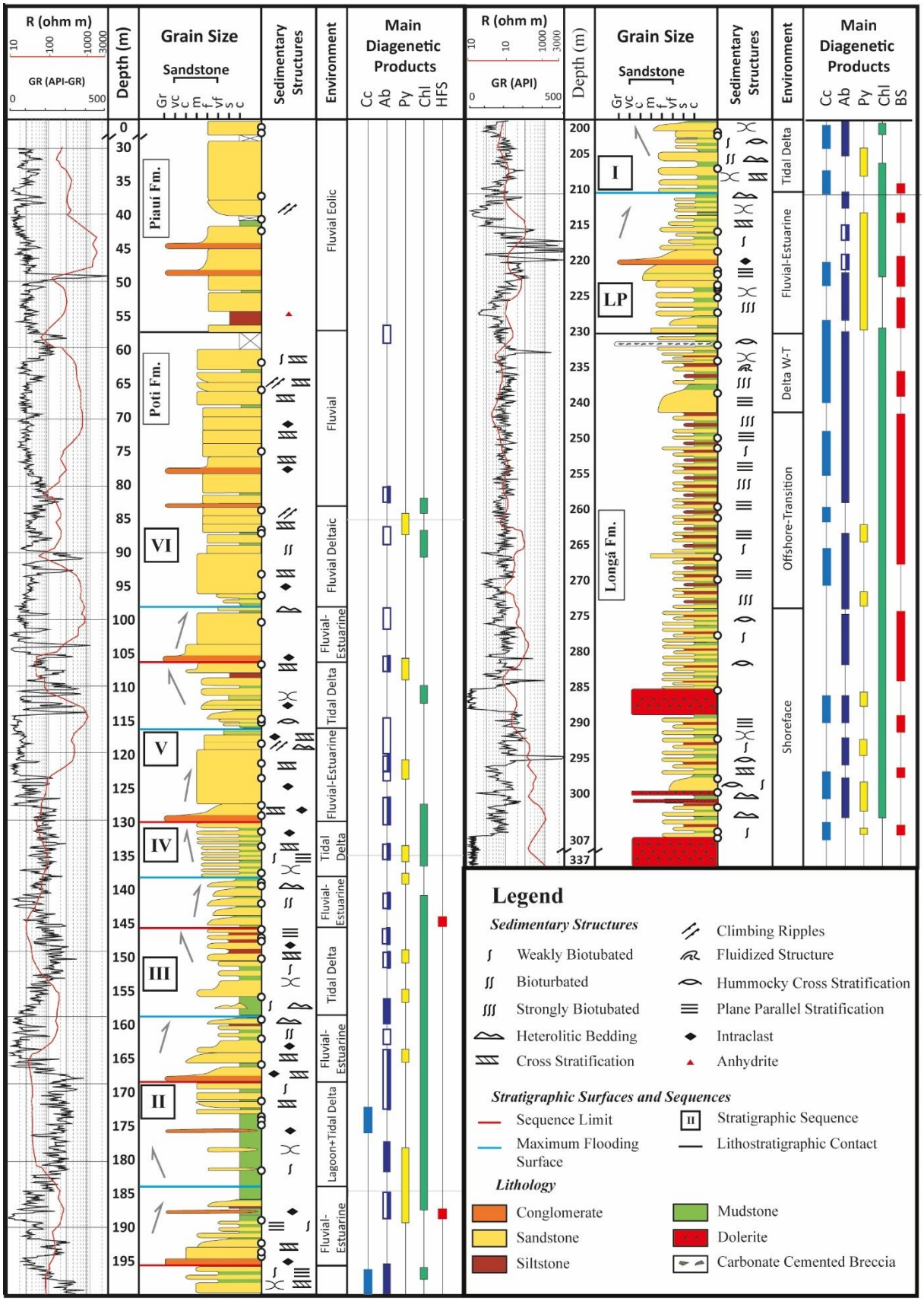

Figure 3. Sedimentary succession divided into stratigraphic sequences with sedimentary structures and depositional environments with gamma-ray and resistivity log profiles on the left-hand side and the main diagenetic products (Cc- calcite in light blue; Ab- albite in filled dark blue for albite overgrowth and

open dark blue marks for microcrystalline albite; Py- pyrite in yellow; Chl- chlorite in green; BS- brittle structures in red). Open circles on the right end of stratigraphic profile represents where thin sections were collected.

In the studied formations, chemical compaction mainly occurs (1) in quartzarenites and subarkoses in which concavo-convex- and sutured intergranular contacts occur and there is little or no presence of detrital clay minerals (Fig. 4 D, E, F, G); (2) in clay-rich and lithic sandstones, in which mica and intraclasts are deformed and have generated pseudo matrix (Fig. 4 A, B, H, I, J). In some cases, mica is altered to biotite by ductile plastic deformation (Fig. 4 A-B). Despite its many forms of occurrence, chemical and mechanical compaction occurs in restricted intervals and play a minor role in primary porosity reduction in the studied stratigraphic units.

2.3.2.2 Feldspar Dissolution and Overgrowth

Feldspar occurs as detrital grains and authigenic crystals with variable contents in mudstones and very fine to coarse-grained sandstones, composing to up to 47 % bulk mineral composition (Fig, 4 C F-J, Fig. 5 -Table 1 - Appendix A). Orthoclase and microcline are the main alkali feldspar phases and albite the main plagioclase phase. K-Feldspar occurs as very fine to medium grained detrital grains in arkosic sandstones of the Poti and Piauí formations and as clay-size grains in mudstones of the Longá and Poti formations. Albite occurs as framework grains, albite overgrowths, microcrystalline grains in bleached mudstones, microcrystalline grains in intergranular spaces and replacing intraclasts (Fig. 4.C, F-I; Fig. 6 F, H, I; Fig. 7 A, B, D). Albite overgrowths mainly occur over very fine- to medium-grained microcline and orthoclase detrital grains, and in minor content over plagioclase grains (Fig. 4 C, F-J). They are pervasive in the middle and upper portions of the Poti formation arkosic sandstones (Fig.3).

Albite overgrowths occur as thin optically discontinuous rounded rims to very large rims of pure albite composition that almost double sizes detrital grain volume. Sutured contacts between albite overgrowths from different detrital grains and with detrital grains itself often occur, suggesting that albite overgrowths occurred before mechanical compaction (Fig. 4 F-G). However, albite overgrowths also occur without the influence of mechanical compaction. Considering both cases, albite precipitation may have occurred in more than one phase or the mechanical compaction have not affected albite overgrowth due to differential mechanical compaction.

The detrital grains, overgrowths and microcrystalline albite grains tend to be less dissolved by later dissolution processes than alkali feldspars (Fig. 4 F, G). In general, K-feldspar grains are partially dissolved, but range from totally dissolved to partially preserved whereas plagioclase grains are totally to partially preserved. In some cases, dissolution process occurs along the contact between the K-Feldspar detrital grain and albite overgrowth (Fig. 4 F-G). In addition, K-Feldspar is generally altered to illite. In general, K-Feldspar and plagioclase contents are inversely proportional comparing samples along the studied sedimentary interval (Fig. 5 – Appendix A). In addition, K-feldspar content tends to increase away from igneous intrusion in sandstone samples (Table 1; Fig 5; Appendix A). K-Feldspar dissolution is the main secondary porosity generator in the subarkoses and arkoses of the Longá, Poti and Piauí formations.

Microcrystalline albite occurs: (1) as cements, filling pores in sandstones (Fig. 4); (2) replacing clay minerals of intraclasts (Fig. 4 H-I-J); (3) as a bleached aureole along mudstone-sandstone contacts (Fig. 6 E, F, H, I and Fig. 7 A, B); and (4) as a bleached aureole along vein and mudstone-host rock contact surfaces (Fig. 8). In all cases, microcrystalline albite presence was identified by means of QEMScan analysis and it occurs in the Longá and Poti formations mudstones and sandstones closer to the main igneous intrusion (Fig.3; Fig.4 H; Fig.6 F; Fig.7 B).

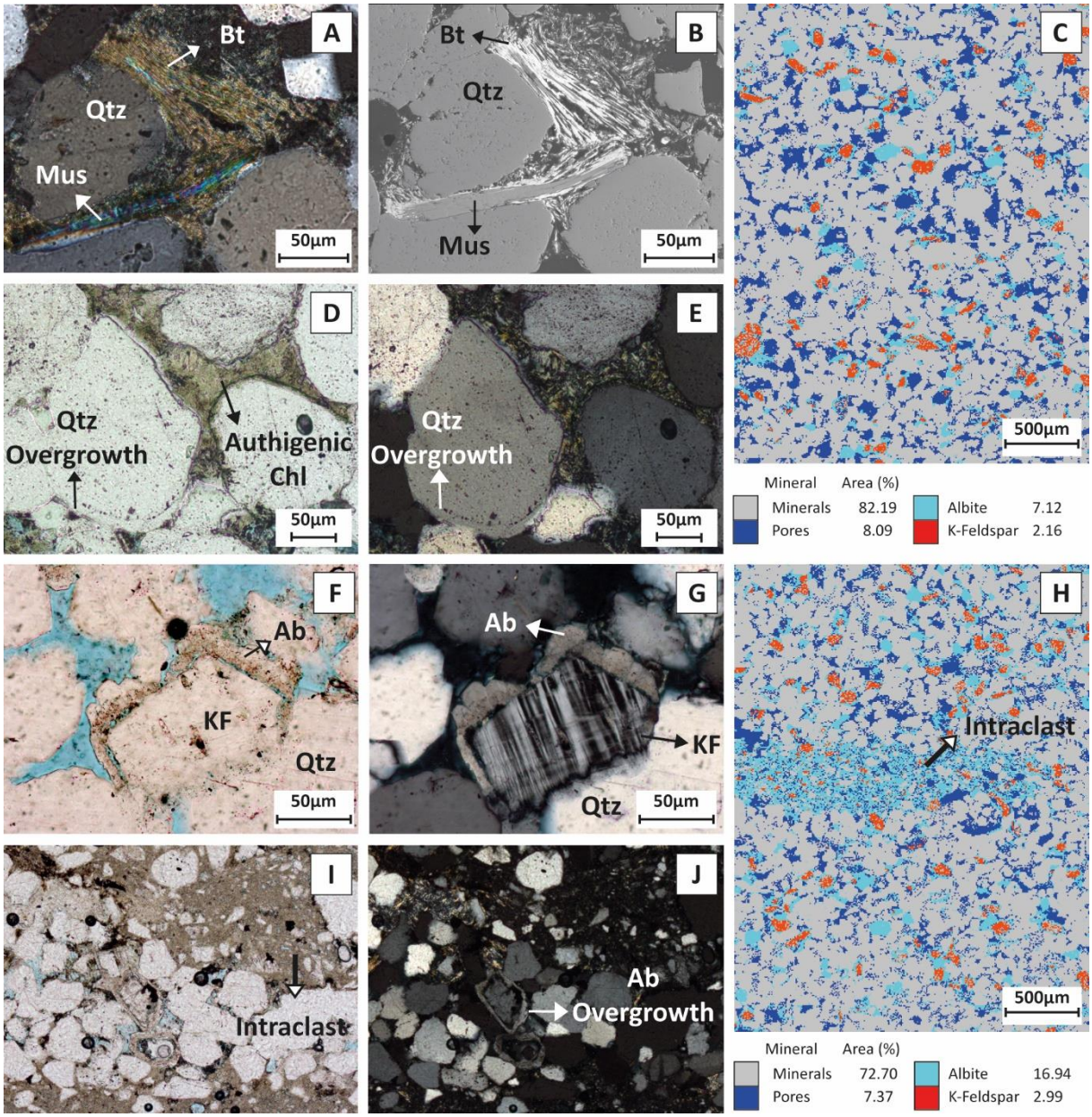

Figure 4. A-B) Photomicrographs in crossed polarized light (XPL) and backscattered electron micrograph, respectively, of ductile plastic deformation of muscovite generating biotite pseudomatrix (Sample 166.00m). **C)** False colour QEMScan image highlighting the different feldspar compositions and showing albite overgrowth (light blue) over K-feldspar detrital crystals (red) and preferential dissolution of K-feldspar compared to albite crystals and overgrowths (inner gray pixels inside K-feldspar crystals) (Sample 121.90). **D-E)** Photomicrographs in parallel polarized light (PPL) and XPL, respectively, of quartz overgrowth with a dust rim and detrital quartz grains with overgrowth corroded by the later cementation of bladed crystals of chlorite growing from quartz grain surface. (Sample 146.80). **F-G)** Photomicrographs in PPL and XPL, respectively, of albite overgrowth over K-feldspar detrital grain with preferential dissolution along their contact; and sutured contact with quartz grain (Sample 121.90m). **H)** False colour QEMScan image highlighting the different feldspar composition and showing intraclasts replacement by microcrystalline albite and albite overgrowths over K-Feldspar grains (Sample

129.10m). **I-J)** Photomicrographs in PPL and XPL, respectively, of microcrystalline albite replacing intraclasts and albite overgrowths over K-feldspar grains (Sample 129.10m).

In the first two type of occurrences, microcrystalline albite occurs associated with sandstone cemented by authigenic chlorite, calcite and pyrite. In the third case, microcrystalline albite occurs along mudstone-sandstone contacts in which the sandstone is cemented by at least two out of the three following minerals: chlorite, calcite and pyrite.

Macroscopically and microscopically, it results in a white bleached rim along the mudstone-sandstone contact (Fig. 6 E-F). In the fourth, it occurs along vein/mudstone host-rock surfaces generating a similar white aureole that marks a disequilibrium between the vein and the host rock mineral assemblage (Fig. 8 A-D).

2.3.2.3 Quartz overgrowth and dissolution

Quartz is the main framework mineral of very fine to coarse-grained sandstones, coarse siltstones and occur in smaller amounts in sandy mudstones composing an average of 47 % and varying from 3 up to 89% of the total bulk mineral composition (Table 1; Fig. 5; Appendix A). Authigenic quartz compose less than 1% of bulk mineral composition and occur as (1) overgrowths in thick subarkoses and quartzarenites with low clay mineral content (Fig. 4 D-E) deposited in fluvial environments (Upper portion of the Poti Formation); (2) filling veins (Fig. 8 A-E); (3) and associated with calcite-cemented intervals (Fig. 6 C-D). Quartz overgrowths are characterized by a discontinuous dust rim on detrital quartz grains, with a clean rim with a rounded external shape (Fig. 4 D-E).

Quartz dissolution by pressure solution associated with mechanical compaction occurs in restricted intervals as mentioned above, whereas quartz dissolution by later cementation processes occur along all the studied interval. Gulfs, corroded crystal surfaces and corroded overgrowths are the main dissolution features in quartz grains (Fig. 4 D, E; Fig. 7 C-F). Quartz overgrowths are hardly preserved, consequently

Table 1. QEMScan analysis of samples in which sandstone grains composed more than 80% of the thin section area. Porcentage values were normalized to classified minerals percentage. See methodology text and appendix A for more information.

Depth	13.8	19.5	40.6	42.7	62.7	64.9	75	84.8	88.7	88.8	93.1	101	106	115	115.6	122	123	128	129	131.9	133.4	140	142	146	147
Quartz	89.6	56.25	39	71.69	55.7	49.14	49.31	39.89	48.57	56.46	48.9	61.13	67.52	32.18	27.84	65.52	61.93	65.61	57.89	65.41	54.73	42.33	42.04	66.16	76.16
K-Feldspar	1.98	3.13	7.87	3.44	10	16.3	13.28	19.51	12.58	1.23	14.36	0.69	2.86	8.76	23.84	4.13	5.22	3.54	3.22	3.68	5.67	11.55	1.6	7.95	1.26
Plagioclase	0.01	0.01	0.05	0.03	6.83	21.18	11.77	14.83	10.78	6.6	14.06	6.21	8.89	18.09	20.28	9.14	10.03	9.41	17.61	4.93	16.87	11.42	0.47	6.93	7.96
Calcite	0	0	0.01	0	0.01	0	0.01	0.01	0.01	0	0.01	0	0	0.01	0.01	0	0	0	0	0	0	0.01	0	0	0
Dolomite	0	0	0	0	0	0	0	0	0	0	0.01	0	0	0	0	0	0	0	0	0	0	0	0	0	0
Siderite	0.02	0	0	0.07	0	0.01	0	0.1	0.46	0.03	0.05	0.02	0.07	0.04	0	0.01	0.65	0.01	0.22	0	1.02	0.02	0.12	0.01	0.03
Chlorite	0	0.01	0.01	0.01	0.01	0.15	0.01	0.18	6.15	0.16	1.66	0.05	0.02	2.07	5.77	0.38	0.1	0.14	0.96	0.42	2.4	4.68	9.93	3.17	4.06
Kaolinite	4.46	15.64	17.6	1.83	4.19	0.6	0.34	0.18	0.08	0.06	0.03	0.05	0.08	0.01	0.01	0.03	0.05	0.03	0.04	0.03	0.01	0.14	0.39	0.04	0.02
Smectite	0.01	0.04	1.87	0.01	0.12	0.49	0.11	0.34	0.3	1.04	0.17	0.77	0.28	0.29	0.32	0.08	0.11	0.06	0.2	0.25	0.24	0.19	0.02	0.1	0.18
Illite	0.68	1.83	11	0.83	2.5	5.29	2.86	5.8	4.37	17.79	2.91	11.39	3.62	16.6	14.71	0.95	0.98	1.17	1.75	2.88	6.17	15.5	6.49	3.93	1.17
Pyrite	0	0	0.01	0.01	0.01	0.01	0.01	0.06	0.02	0	0.03	0	0.03	3.08	1.88	0.02	0.01	0.06	0.01	0.01	0.02	0.03	16.72	0.05	2
Phosphates	0	0	0	0	0	0.01	0.01	0.01	0.01	0	0.01	0.01	0.01	0.21	0.4	0	0	0	0	0.01	0	0.11	0.07	0.01	0.01
Oxides	0.16	0.39	0.56	0.12	0.23	0.33	0.18	0.37	0.34	0.19	0.28	0.25	0.42	0.35	0.53	0.11	0.57	0.11	0.45	4.04	0.37	0.67	0.3	0.34	0.14
Muscovite	0.13	0.18	0.7	0.03	0.11	0.15	0.08	0.04	0.02	0.02	0.07	0.01	0.01	0.03	0.18	0.02	0.01	0.01	0.01	0.01	0.01	3.97	1.93	0	0.02
Biotite	0.1	0.01	0.09	0.05	0.05	2.14	0.04	1.4	4.25	0.09	1.46	0.02	0.09	1.37	2.62	0.51	0.44	0.3	0.33	0.52	2.57	7.36	10.02	0.12	0.96
Pores	2.81	22.47	21.2	21.85	20.1	4.09	21.94	17.11	11.33	16.28	15.8	19.34	16.02	16.86	1.55	19.01	19.73	19.48	17.28	17.69	9.56	1.87	9.72	11.13	5.98
Normalized Total %	99.96	99.96	100	99.97	99.9	99.88	99.95	99.85	99.27	99.95	99.82	99.96	99.92	99.95	99.93	99.91	99.83	99.93	99.96	99.89	99.62	99.85	99.83	99.94	99.96

Depth	148	150	156	159	166	172	175	183	189.3	190	192	194	195	207	215.9	219	221	224	232	238.3	259.8	290	298	302	306
Quartz	64.26	50.66	41.9	56.2	76.3	67.07	60.73	53.5	67.83	61.12	59.06	83.28	77.6	44.61	47.35	63.18	21.42	76.64	43.19	44.29	38.93	41.14	49.92	49.92	51.59
K-Feldspar	1.15	21.6	8.6	10.94	6.2	7.22	4.66	0.09	0.01	3.21	0.03	0.16	0	3.98	0.36	2.83	0.64	0	0	0	0.25	5.58	0.05	0	9.32
Plagioclase	4.99	15.63	4.99	9.67	5.95	9.16	3.29	11.19	5.05	6.17	2.13	1.95	0.43	17.8	25.14	9.82	4.58	4.73	26.53	3.46	36.8	15.87	10.39	25.36	23.53
Calcite	0.01	0.01	0.01	0	0	0	0.01	0	0	0	0	0	0	0.38	0	0.02	0	3.21	0.01	0.04	0.56	4.48	0.08	2.78	0.74
Dolomite	0	0	0.01	0	0	0	0.01	0.2	0	0	0	0	0	0.01	0	0.01	0	0.11	5.4	0	0	0.51	0.06	0.01	0.01
Siderite	0.01	0.01	1.19	0.02	0.09	0.01	0.19	0.04	0.72	0.01	0.04	0.01	0	0	7.5	0.01	0	0.08	1.31	1.04	0.02	0.02	0.56	0.36	0.03
Chlorite	1.65	2.23	24.3	10.04	0.12	6.19	6.78	3.17	4.51	4.41	7.77	0.21	4.3	4.94	4.64	6.58	0.29	3.59	10.64	45.22	15.84	8.51	15.51	5.75	2.27
Kaolinite	0.02	0	0.01	0.04	0.01	0.41	0.06	0.08	0.04	0.02	0.02	0.24	0.1	0.09	0.02	0.04	9.83	0.09	0.01	0	0.12	0.03	0.83	0.01	0.01
Smectite	0.04	0.03	0.38	0.16	0.02	0.28	0.34	0.11	0.07	0.03	0.28	0.13	0.5	0.61	0.23	1.05	0.19	0.09	0.25	0.1	0.61	0.12	0.14	0.29	0.13
Illite	0.94	4.07	5.69	2.89	2.22	3.2	11.06	1.54	0.07	2.37	2.28	1.21	0.07	15.43	0.48	2.77	36.55	0.02	0.06	0.01	2.21	18.82	8.91	0.02	6.99
Pyrite	0.31	0.39	0.43	0.07	0.01	0.96	0.15	0.06	9.03	5.4	4.07	0.1	0.04	0.01	1.38	1.15	0.04	0.45	0.04	0.04	0.02	0.01	2.34	6.33	1.99
Phosphates	0.07	0.55	0.18	0.09	0.06	0.12	0.13	0.42	0.09	0.07	0.13	0.1	0.07	0.19	0.13	0.16	0.16	0.16	1.88	3.76	0.64	0.21	0.67	0.43	0.23
Oxides	0.17	0	0.46	0.32	0.43	0.21	0.34	0.28	0.37	0.31	0.11	0.31	0.09	0.42	0.11	0.17	0.5	0.29	0.54	0.43	0.61	0.58	0.4	0.68	0.85
Muscovite	0.41	0.01	0.25	0	0.19	0	1.83	0.41	0.01	0.1	0.01	0.01	0	0.57	0	0.04	10.7	0	0	0	0.41	0.23	0.2	0	0.13
Biotite	6.79	0.32	4.44	0.06	2.43	0.07	0.68	5.33	0.03	0.16	2.03	0.76	0.12	5.44	3.05	1.91	1.07	0.02	0.01	0	0.68	3.46	0.88	4.52	1.1
Pores	19.07	0.93	6.96	9.43	5.86	5.09	9.72	23.42	12.12	16.55	22.04	11.46	16.64	5.38	9.48	10.18	13.99	10.49	10.07	1.55	2.25	0.33	8.95	3.27	1.01
Normalized Total %	99.91	96.44	99.8	99.94	99.9	99.97	99.99	99.85	99.96	99.95	99.99	99.94	99.97	99.86	99.86	99.93	99.97	99.99	99.96	99.94	99.96	99.9	99.91	99.75	99.94

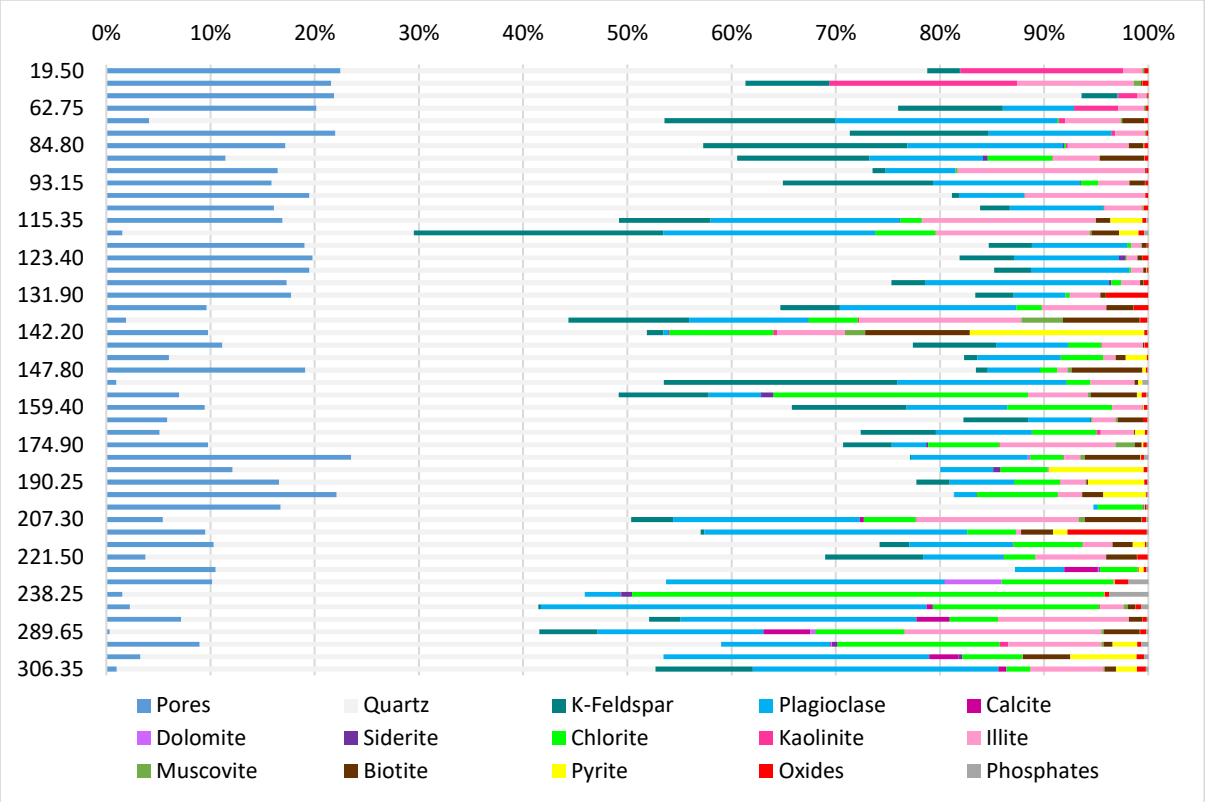

Figure 5. Bulk mineral composition of 49 thin sections composed of more than 80% of sandstone. All samples QEMScan data are presented in Appendix A.

sometimes it is difficult distinguish between *in situ* overgrowth and inherited quartz overgrowths from source rocks. Distinct euhedral to subhedral quartz crystals occur along veins and associated with carbonate-cemented sandstone intervals (Fig. 6 C-D; Fig. 8 A-E).

2.3.2.4. Chlorite

Chlorite crystals occur with radial, bladed, randomly arranged subhedral plates, lath-shaped and massive habits with crystal sizes varying from <5 µm to up to 60 µm. Chlorite comprise up to 45% of sandstone bulk mineral composition, with an average of 6% TBMC (Table 1; Fig. 5; Appendix A).

Chlorite occurs frequently in mudstone and sandstones at depths greater than 130m and erratically at intervals above 130m of depth where it mostly occurs associated with mudstone

intervals. Authigenic chlorite occur: (1) as the main pore-filling mineral phase in sandstones resulting in a greenish or greenish spotted sandstone (Fig. 4 D-E; 6 E-F; H-I; 7 A-F); (2) filling veins and in aureoles in mudstone host-rocks crosscut by veins (Fig. 7 A, B , E-H; 8 A-E; 9 A, D, E;); (3) forming rounded (nodular) agglomerates in mudstones, also resulting in a spotted texture (Fig. 9 A-G; 10 E-I); (4) filling discontinuous vertically symmetrical horizontal structures and layer transgressive structures in mudstones (Fig. 9 B,C and Fig. 10).

In the first two cases, the radial and bladed chlorite crystals usually grow from a framework grain surface or vein wall towards the pore-centre or vein space, respectively (Fig. 4 D, E; Fig. 7 C-F, Fig. 8A-C; Fig. 9A, D, E). Chlorite with acicular and massive habits occur filling intergranular spaces associated with corroded framework grains (Fig. 6 E, F, H; Fig. 8 C, D; Fig. 11 A-D).

When associated with veins, chlorite mainly occurs in two contrasting forms. Inside veins, it occurs as bladed and radial chlorite crystals in the footwall, whereas outside veins it presents microcrystalline habit of the inner aureole in mudstone-host rock (Fig. 8 A, D-E).

In mudstones, the third case, authigenic microcrystalline chlorites occur as rounded agglomerates resulting in greenish grey spotted texture in macroscopic scale (Fig. 9 D-G). Chlorite spotted mudstones generally occur close to veins, or heavily cemented sandstone layers.

In the fourth case, microcrystalline chlorite occurs intergrown and associated with acicular iron oxides filling vertically symmetrical horizontal structures (Fig. 10 E-H) and filling transgressive structures (Fig. 10 A-D). In the last example, microcrystalline authigenic chlorite can be associated with two types of structures: (1) transgressive structures that crosscut sedimentary beddings, breaches in mudstone layers and migrate continuously along siltstone layers (Fig. 10A-D); (2) veins that forms from porous sandstone bodies into low permeability mudstone levels where chlorite shows intergrowths with iron oxides (Fig. 7 E-F). More rarely occur as parallel to the vein walls elongated crystals (Fig. 7 G, H). These two forms of chlorite occurrences of the fourth case will be further detailed below in the brittle structures section.

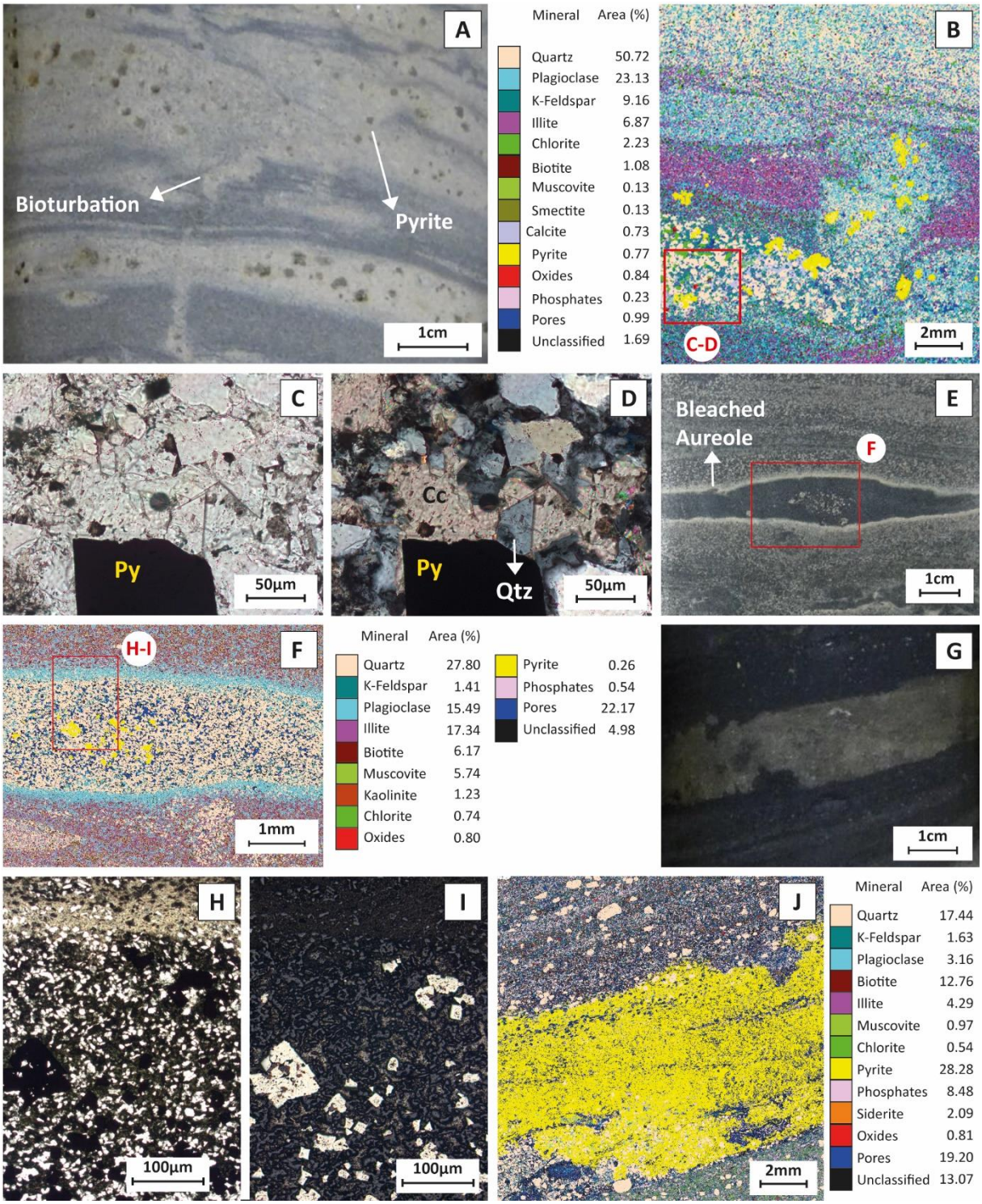

Figure 6 A) Core sample of interlaminated and weakly bioturbated siltstone and mudstone with scattered pyrite crystals (Sample 306.35) **B)** QEMScan false colour map highlighting preferential authigenic mineralization of chlorite, pyrite, quartz ± calcite along coarser grained intervals and sand-filled bioturbations (Sample 306.35). **C-D)** Photomicrographs in PPL and XPL, respectively, taken under transmitted light correspondent to the coarser grained interval on the lower portion of the Figure 8B showing the pyrite, calcite and quartz cementation (Sample 306.35). **E)** Core sample with dotted texture

and a zoned coarse siltstone layer with white coloured rims and green coloured central portion with pyrite crystals. The red rectangle corresponds to the Figure 8F location (Sample 227.85). **F)** QEMScan false colour map highlighting the composition of the zoned interval with microcrystalline albite rims (white in Fig. 7E) and chlorite and pyrite in the central portion (green zone in Fig. 7E). The red rectangle corresponds to the Figure 8H-I location (Sample 227.85). **G and J)** Core sample of sandy mudstone and QEMScan false colour map with 2cm thick sulfide massive layer (Sample 202.55). **H-I)** Photomicrographs taken under transmitted (XPL) and reflective lights (PPL), respectively, showing the microcrystalline albite rim a.long the mudstone and very fine sandstone and the sandstone interval cemented by chlorite and pyrite. Observation: comparing the figures 8F and 8H, the underestimation of the chlorite content filling the pores may have occurred due to araldite absorption by chlorite and it was identified as pores in QEMScan analysis.

2.3.2.5. Other Clay minerals

The occurrence of clay minerals is associated with mudstones; and with mudstone intraclasts, mud drapes, heterolithic bedding in sandstones. In the studied rocks, illite, chlorite, muscovite, biotite, kaolinite, smectite and glauconite are the main clay minerals phases. Illite, chlorite, biotite and muscovite are the main constituents of mudstones with total bulk mineral compositional averages (TBMA) of 13.2%, 6.1 %, 5.8%, and 4.17% respectively (Fig. 5; Table 1; Appendix A).

Other clay minerals with total bulk mineral composition lower than 5% were mainly identified by means of QEMScan analysis due to petrography scale limitation (Appendix A). For example, kaolinite, smectite and glauconite show an average composition of less than1% of total bulk mineral composition in the studied samples. However, kaolinite reaches up to 15.62% when it occurs associated with altered feldspars and as intraclasts in the Piauí formation sandstones in the shallowest levels of the studied well (<40m of depth) (Fig. 5 – Table 1).

In sandstones, illite and chlorite are the main authigenic clay mineral phases with total bulk mineral compositional averages of 4.88 and 4.54%, respectively (Table 1- Fig. 5 -

Appendix A). Muscovite and biotite occur mainly as detrital grains and composing intraclasts. Biotite also occurs as pseudomatrix, formed as a product of ductile plastic deformation of muscovites (Fig. 4 A-B).

Muscovite and biotite occur mainly as detrital grains and composing intraclasts. Biotite also occurs as pseudomatrix, formed as a product of ductile plastic deformation of muscovites (Fig. 4 A-B). Authigenic chlorite, illite ± biotite crystals occur as cement in sandstones. More analysis is required to determine textural relationship of pore-occluding clay minerals. Authigenic illite is mainly related to partial to total K-feldspar dissolution and can reach up to 10.5% of bulk mineral composition in sandstones (Fig. 4 H-J; Fig. 5; Appendix A).

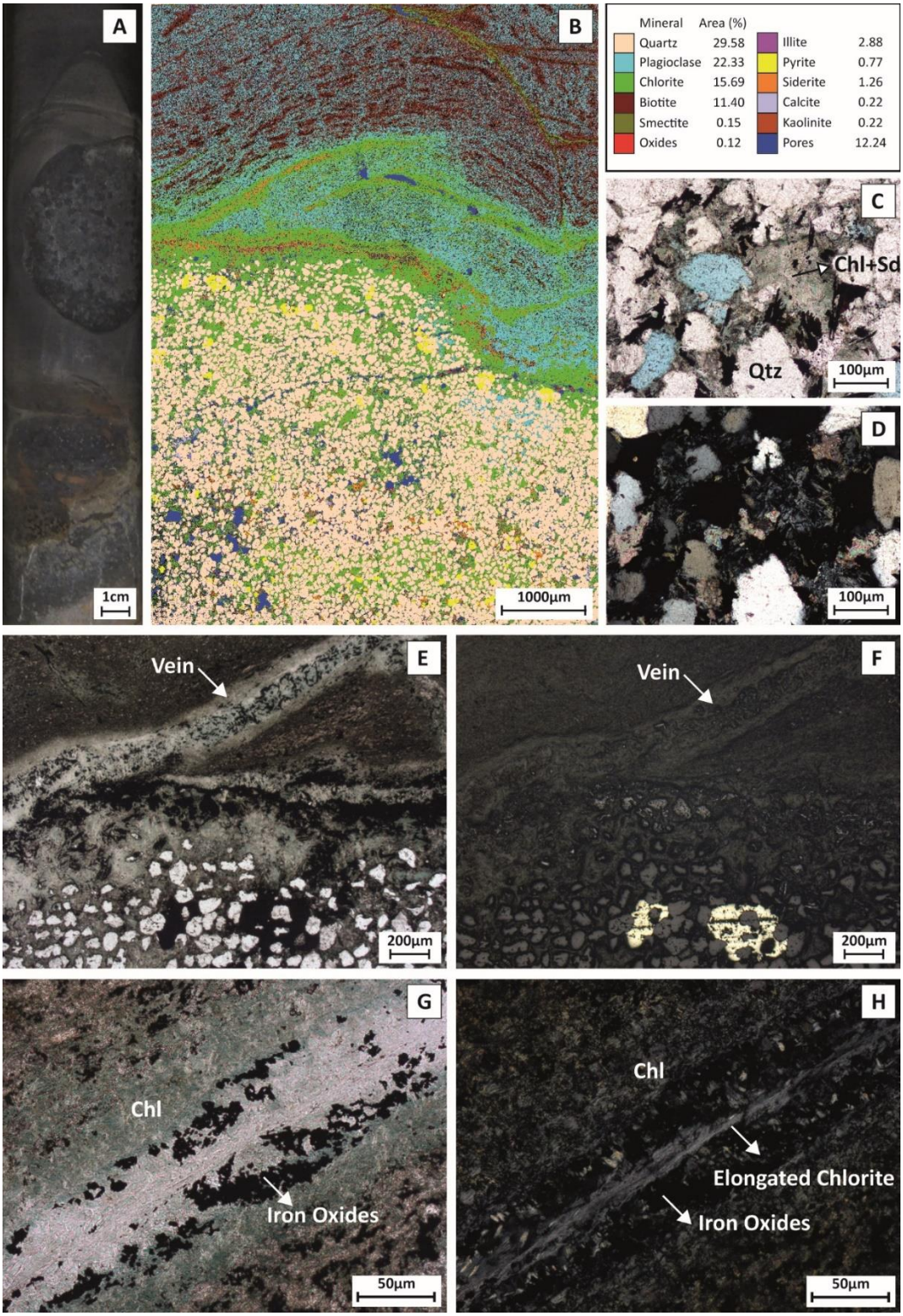

Figure 7 A) Photograph of core sample showing ductile structure with a rounded and spotted sand body on the upper part and highly mineralized nodules on the lower part with fractured mudstone surrounding them. **B)** QEMScan false colour map at the upper contact between the spotted sandstone body cemented by albite, calcite, pyrite and iron oxide and the mudstone, which is composed of a microcrystalline albite mass with orientated biotite and iron oxides clusters. **C-D)** PPL and XPL photomicrographs, respectively, taken under transmitted light in of sandstone cemented by chlorite, iron oxides and calcite. **E-F)** Photomicrographs taken under transmitted light and reflected light in PPL and XPL, respectively, of sandstone body and the mudstone contact (correspondent to the central left

portion of Figure 7B marked by a pervasive cementation of chlorite, iron oxides and pyrite with a vein filled with chlorite and iron oxide ending/starting at lithological contact surface. **G-H)** Detail PPL and XPL, respectively, photomicrographs taken under transmitted light of a vein filled with chlorite and anhedral iron oxide crystals in central portion, and by wall vein-parallel elongated chlorite crystal in the outer portion.

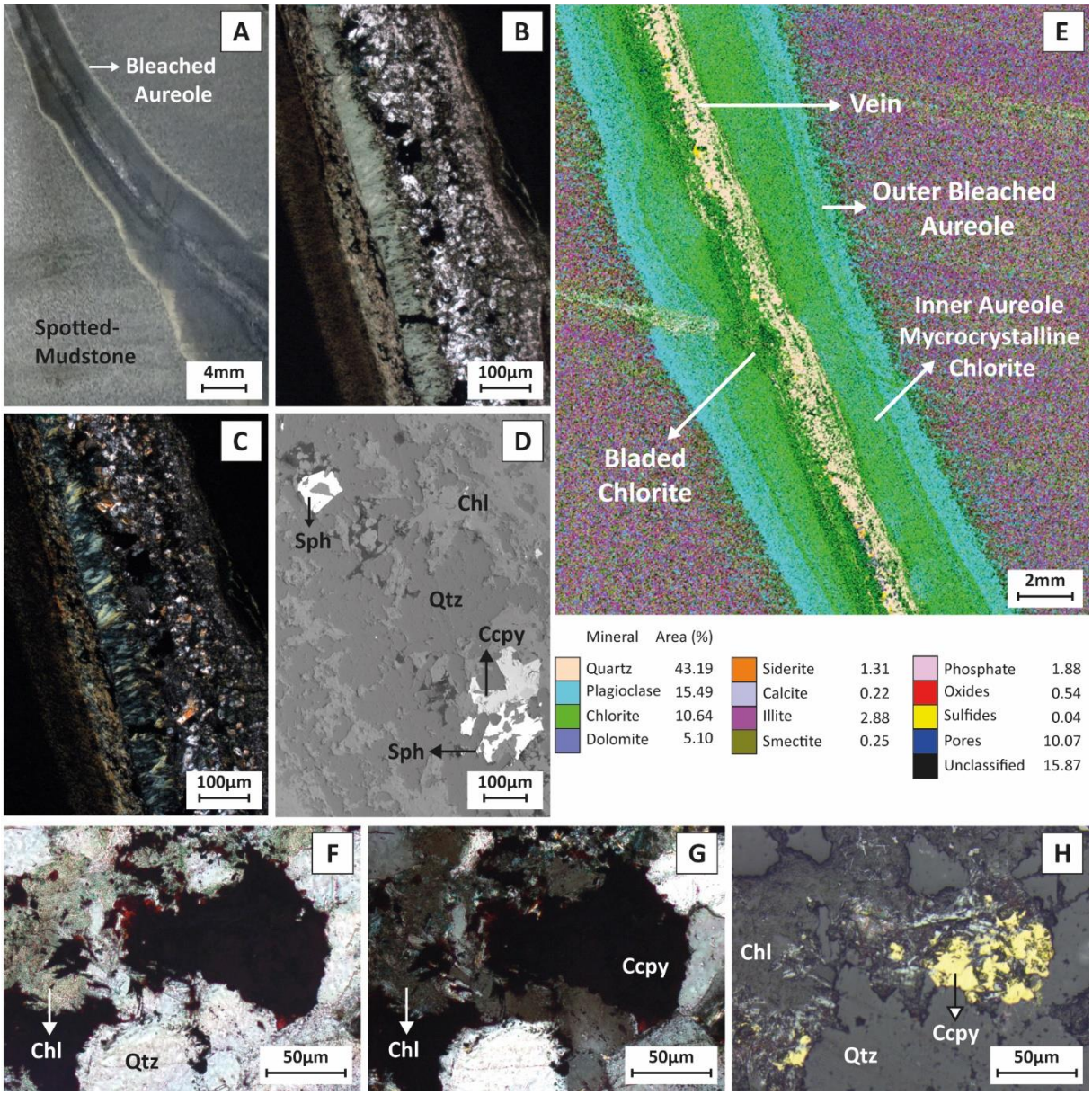

Figure 8 A) Core sample of a subvertical assymmetrical vein crosscutting a greyish-green spotted mudstone with a white bleached aureole. **B-C)** Photomicrographs taken under transmitted light with PPL and XPL, respectively, of the central portion of the vein showing an asymmetrical aspect with bladed chlorites growing from the footwall towards the hanging of the vein which is filled with quartz, chalcopyrite and sphalerite ± calcite. **D)** Back-scattered image of the upper central portion of the figures B and C with euhedral and anhedral sphalerite crystal and anhedral chalcopyrite crystal. **E)** QEMScan false colour map showing an outer aureole of microcrystalline albite, an inner aureole of microcrystalline chlorite and the vein filled with the bladed chlorite, quartz, sphalerite, chalcopyrite and minor amounts of calcite (Sample BG-251.65). **F-G-H)** Photomicrogrphs taken under transmitted light in PPL and XPL and under reflective light with parallel polarizers, respectively, of anhedral chalcopyrite altering to

hematite in sandstones cemented by chlorite. Detrital quartz and overgrowths are corroded by chlorite and chalcopyrite (Sample BG 297.50m).

2.3.2.6. Sulfides

Pyrite corresponds to most of the sulfide phases, with chalcopyrite and sphalerite occurring only in veins and disseminated in a few sandstone intervals associated with pyrite (172.30; 227.85; 266.70m; 297.50m). Galena occurs as inclusions in pyrite crystals and as trace minerals in the very same samples. Pyrite occurs discontinuously in mudstones and sandstones intervals at depths greater than 130m and becomes restrictedly associated with mudstones at depths shallower than 130m (Fig. 3). Pyrite composes up to 28.28% of bulk mineral composition with an average of 1.33% (Figure 5; Table 1; Appendix A). Pyrite occurs as hexagonal euhedral crystals and as anhedral crystals with minor occurrence of framboidal habits. In some cases, crystals with a slight anomalous birefringence and square euhedral crystals occur and indicate pyrrhotite occurrence which is a pyrite pseudomorph. Pyrite crystals occur as single crystals or agglomerated crystals disseminated in sandstones replacing and/or englobing framework grains and with a massive habit forming millimetric to up to 5cm thick layers of pyrite cementing sandy-mudstones (Fig. 6; Fig. 7A-B, E-F).

Sphalerite occurs as anhedral and euhedral crystals of up to 200µm and chalcopyrite occur as anhedral crystals of up to 150µm (Fig. 8 D-H). The suphide-rich vein is composed of an outer rim of microcrystalline albite, an inner aureole of microcrystalline chlorite and an asymmetrical central portion filled with chlorite bladed crystals on the footwall and quartz with chalcopyrite and sphalerite on the hanging wall. A minor content of calcite occurs near the limit between bladed-chlorite crystals and quartz domains (Fig. 8E).

2.3.2.7. Oxides

Iron oxides occur as nodules in sandstone layers, cement in mudstone layers, orientated clusters in a rare ductile deformed mudstone interval and intergrown with microcrystalline chlorite in beef-like and transgressive structures (Fig. 7; 10;11 D). Below 130m of depth, most of the iron oxide present weak to strong magnetism in the presence of swing pen magnet. Regarding habits, iron oxides occur as microcrystalline crystals and lath-shaped crystals. The form of occurrence, magnetism, and microcrystalline habit suggest the presence of magnetite; in other cases, the lack of magnetism and lath-shaped crystal suggest the presence of hemaetite. At lower levels, iron oxi-hydrates presents similar habits of chlorite, pyrite, and iron oxide occurrences in deeper levels, but they do not occur simultaneously. Shallower iron oxi-hydrates domain and deeper chlorite, pyrite and iron oxide domain are marked by a contrast macroscopically change of colour from the greenish-grey colour close to igneous intrusion to a brownish colour close to the surface.

2.3.2.8. Carbonates

Calcite, dolomite, and siderite are the main carbonate phases. They occur: (1) as cement in sandstones (Fig. 6 A-D; Fig. 11 A-D); (2) as carbonate cemented breccias in mudstones (Fig. 11 E-H); (3) and filling subvertical to sub horizontal veins crosscutting sedimentary (Fig. 9 A-E) and igneous rocks. All three types of carbonate occurrences occur at depths greater than 170m (Fig. 3).

Carbonates presents an average of 1% of TBMC of the studied samples but occur in greater amounts (>2%) closer to the igneous intrusion, composing up to 17.22% of TBMC (Figure 5; Table 1; Appendix A). Calcite is the main carbonate phase occurring as coarse-grained crystals filling veins and cementing carbonate breccias that will be further characterized below (Fig. 6 A-E; 11 E-H). Calcite rarely occurs as poikilotopic and fine-grained

crystals in sandstones (Fig. 6 B-D). Dolomite rarely occur as cement in amounts greater than 1% of TBMC, except for one sample in which it composes 5.40% of TBMC (232.20m-Fig. 11A-D). Siderite corresponds to 1 to 2% of TBMC in certain intervals of the Poti Formation in which sandstones are associated with iron-rich phases (i.e. chlorite and pyrite).

2.3.2.9. Brittle structures

Brittle structures occur as subvertical veins and fractures, horizontal breccias, layer parallel-transgressive structures and beef-like structures. In the studied sedimentary sequence, it occurs from the bottom (337.50m), up to 170m of depth of the studied drill core showing an increase frequency towards igneous intrusion. In igneous rocks, centimetric to metric calcite and pyrite veins crosscut main igneous sill and the 4 m thick splay above it.

In sedimentary rocks, brittle structures can be grouped based on the main mineral assemblage filling content and geometry. The first brittle structure group is composed of calcite-filled subvertical veins and layer parallel/ horizontal veins and breccias (Fig. 6 A-E; 11 E-H). Calcite subvertical veins occur in sedimentary rocks close to igneous intrusion in distances lower than 10m from igneous-sedimentary contact. Layer parallel/horizontal veins and carbonate-cemented breccias occur restrictedto the interval between 261 and 230m (Fig. 3). Calcite-cemented breccias clasts are composed of adjacent upper and lower mudstone (Fig. 11 E-H).

The second group of brittle structures comprises layer parallel-transgressive structures and beef-like structures that are discontinuous vertically symmetrical horizontal structures filled by chlorite, iron oxide and very fine non-identified minerals. Macroscopically these structures often connect with each other in more than one point. Eventually, in high-frequency siltstone-mudstone intercalations, , the layer parallel-transgressive structures present a contrasting geometry pattern depending on the host rocks. In siltstones, it presents a layer-parallel

geometry, whereas in mudstones it occurs with high- to low-angle and branching geometry (Fig. 10A-D).

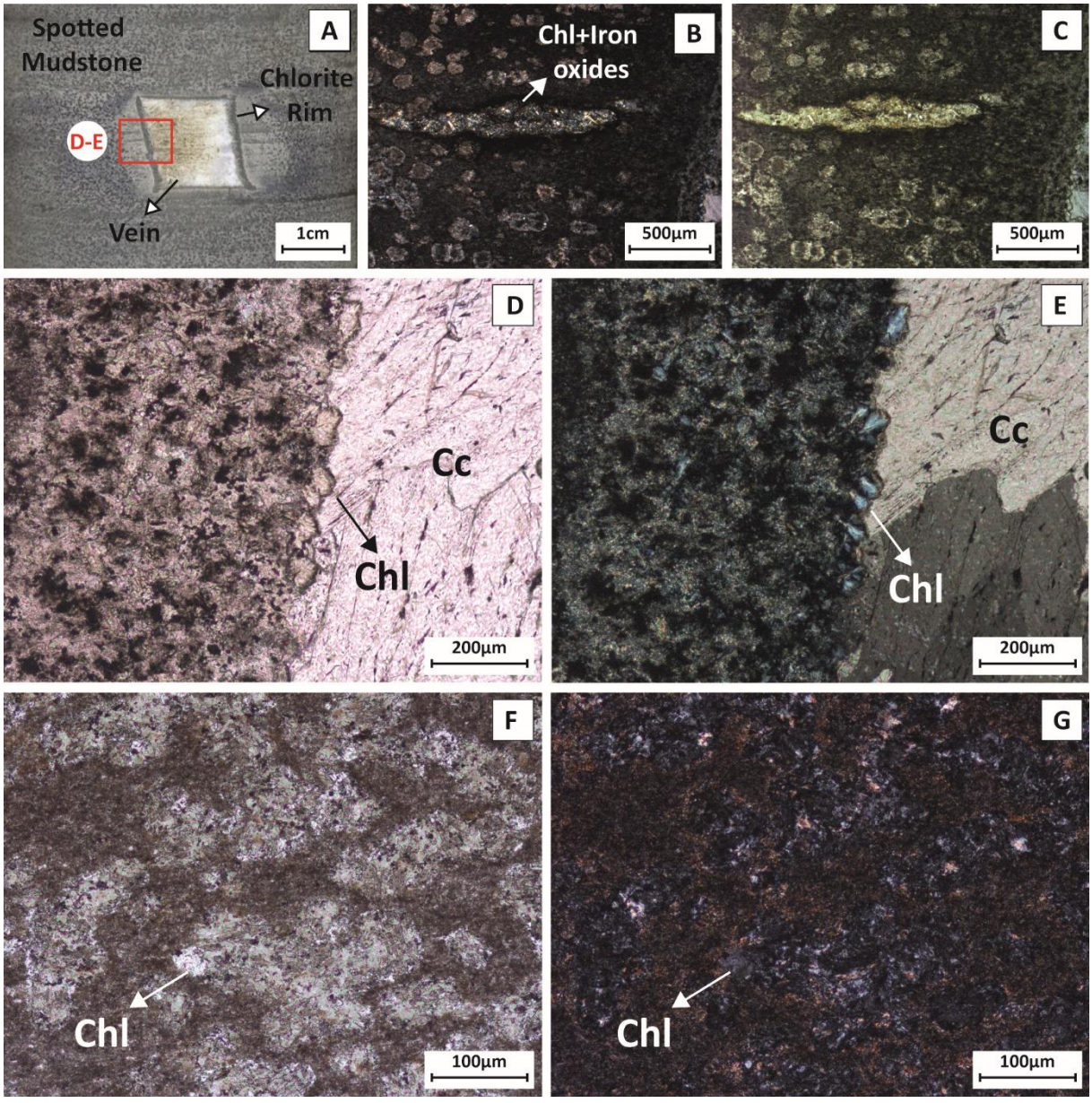

Figure 9 A) Core sample photo of horizontal square tube-shaped calcite vein with spotted texture in mudstone well core photograph (Sample 261.65m). **B-C)** Photomicrographs in PPL and XPL) of nodules that result in spotted texture and horizontal vertically symmetrical cylindrical structure, both are filled with chlorite and iron oxides. **D-E)** Photomicrographs in PPL and XPL, respectively, of calcite vein and mudstone contact with authigenic radial chlorite growing from the mudstone surface inwards the calcite vein (Sample 261.65m). **F-G)** Photomicrographs in PPL and XPL, respectively, of the spotted texture composed of chlorite and minor iron oxides crystals in mudstone (Sample 266.70m).

In all cases, vertical microfractures crosscut siltstone layers and connect transgressive-structures hosted in two different mudstone layers (Fig. 10A-D). In addition, transgressive structures do also connect siltstone and sandstone layers that were once isolated from each other by a mudstone layer (Fig. 10A-D).

Discontinuous vertically symmetric horizontal structures occur in mudstones and are often associated with a microcrystalline albite aureole, vertical microfractures, and nodular agglomerates of authigenic chlorite (Fig. 9; Fig. 10). These structures are composed of randomly arranged microcrystalline chlorite and anhedral to acicular randomly arranged iron oxide crystals that form an intersection line at the center of the structure giving a vertically symmetrical geometry (Fig. 9 B,C; Fig.10E-I). The symmetrical geometry suggests an in situ intergrow of chlorite and iron oxide that may occur from the top and bottom of the structure towards its center or from a center planar structure outward.

In addition, at a single interval around 223.95m deep, ductile structures occur associated with brittle structures. This interval is composed of a rounded sandstone body surrounded by plastically deformed mudstone (Fig. 7). This interval presents an increase in the frequency and modal percentage of diagenetic cements of chlorite, albite, pyrite, calcite (Fig.3 and 5; Appendix A). QEMScan data showed that the ductile foliation in mudstone is composed of iron oxides and microcrystalline elongated biotite clusters in a microcrystalline albite mass contouring the sandstone rounded body (Fig. 7 A-B). The mudstone present strong magnetism in the presence of swing magnetic pen. The sandstone body is heavily cemented by chlorite, calcite and siderite/iron oxides which gives its spotted texture in macroscopic core sample (Fig. 7 A-D). Chlorite and iron oxide veins occur within the mudstone interval but do not continue into the sandstone body.

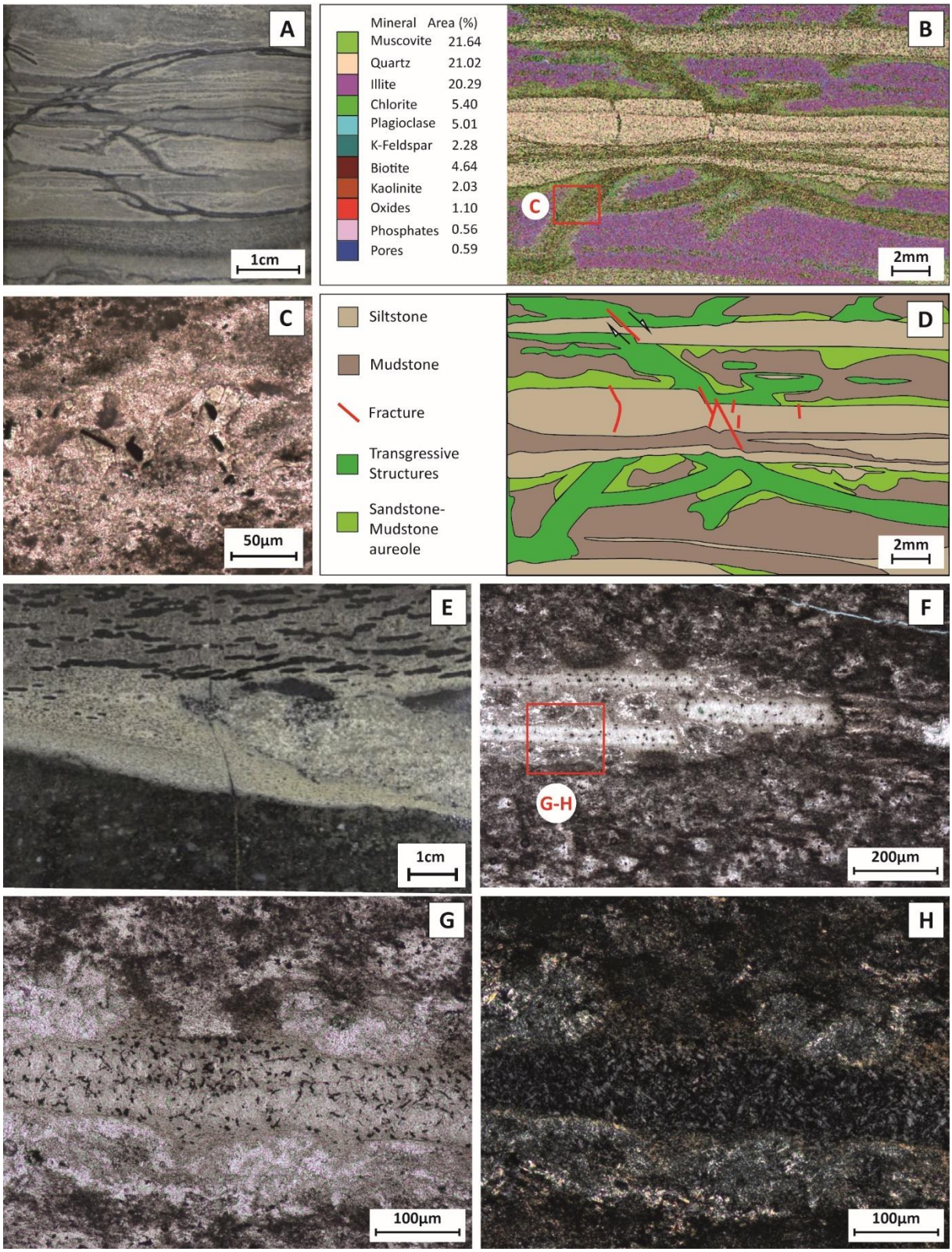

Figure 10 A) Core slab photograph of dark grey layer parallel-transgressive structures in alternating siltstone-mudstone interval (Sample 292.70). **B)** QEMScan false colour map showing that the transgressive structure shows a low- to high-angle and branching behaviour in mudstones and a layer-parallel and associated with vertical microfractures in siltstone layers. **C)** Photomicrograph in PPL taken

under transmitted light of the inner portion of a transgressive structure with lath-shaped chlorite and randomly arranged opaque crystals. **D)** Schematic figure of QEMScan false colous map presented in Fig. 10 B highlighting transgressive structures and sandstone-mudstone aureoles. **E)** Core sample photo of dark green sandstone overlain by white mudstone with discontinuous horizontal structures (Sample BG-225.00). **F)** Photomicrographs in PPL taken under transmitted light of vertically symmetrical horizontal structures that occur in a stacked geometry and are associated with nodular texture in the host mudstone (Sample BG-225.00). **G-H)** Detail photomicrographs taken under transmitted light with PPL and XPL of chlorite and iron oxide intergrown crystal in random arrangement forming an interception line at the central portion and with microcrystalline albite rim around it (Sample BG-225.00).

2.3.3 Chlorite Mineral Composition and Geothermometric Data

The studied authigenic chlorites are all tri-trioctahedral and vary in composition from chamosite to clinochlore (Wiewóra and Weiss, 1990) and Mg- to Fe- chlorite (Zane and Weiss, 1998). The Fe/Fe+Mg ratio varied from 0.26 to 0.88 with an average of 0.58, and the #Mg number varied from 11.6 to 73.8 with an average of 41.6 (Appendix B). Chlorite formation temperature varied from 70°C to 342°C based on the four different geothermometer methods used (Cathelineau, 1988; Kavalieris et al., 1990; Kranidiotis and Maclean, 1987; Zang and Fyfe, 1995).

The Kavalieris et al. (1990) method based on Si—tetrahedral occupancy presents the lowest temperature trends and the Kranidiotis and Maclean (1987) method based on Al-tetrahedral occupancy presents the highest temperature trends (Appendix B). The higher the temperatures, the higher were the values of standard deviations calculated for different methods in individual analysis. The geothermometric data can be roughly divided into two main temperature plateaus. The highest plateau with average temperatures around 250°C ±37 and the lowest around 150°C ±49 (Fig. 15). The high and low temperature authigenic chlorites show little or no relationship regarding its distance to the igneous intrusion as they occur in alternated levels and low-temperature chlorite forms close to igneous intrusions. Six out of the

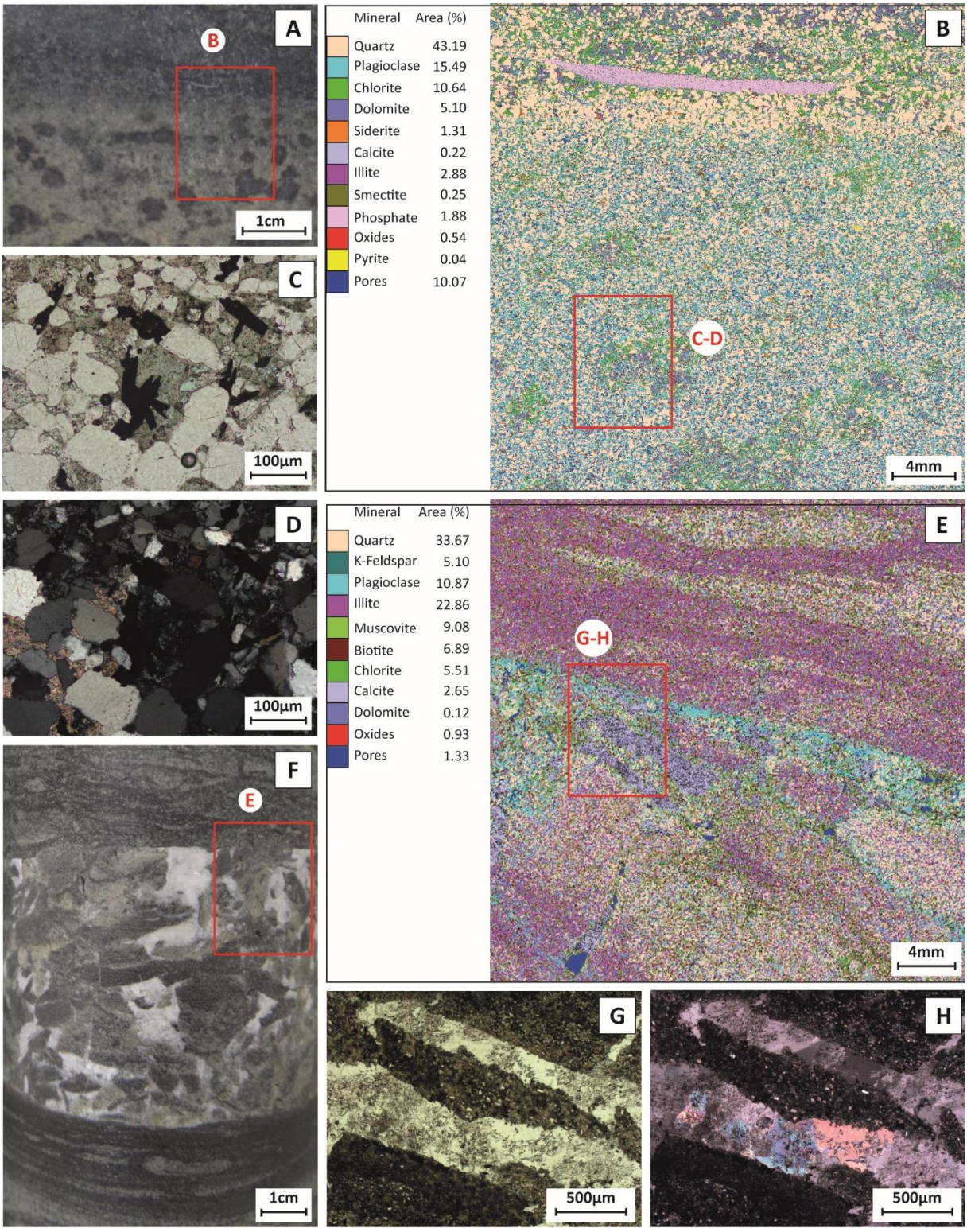

Figure 11. A) Photograph showing the contact of white coarse sandstone with greyish green spots and very fine-grained sandstone with elongated phosphate clast (Sample 232.20). **B)** QEMScan false colour map of bulk mineral composition showing chlorite, dolomite and haematite spots (Sample 232.20). **C-D)** PPL and XPL photomicrographs showing iron oxides, dolomite and chlorite as the main pore-occluding minerals. Macroscopically, they correspond to greyish green nodules of Figura 11A (Sample 232.20). **E)** QEMScan false colour map of bulk mineral composition showing the upper limit of a

carbonate cemented breccia which is marked by microcrystalline albite aureole(light blue) and a similar composition of the upper host rock and breccia intraclasts (Sample 234.85m). **F)** Well core photograph of the carbonate breccia with adjacent mudstone intraclasts (Sample 234.85) **G-H)** PPL and XPL photomicrographs of the inner portion of the carbonate cemented breccia with mudstone clasts.

eight high- temperature chlorite samples present chalcopyrite in the mineralogical composition (e.g. 251.65 and 297.50m samples; Figs. 8 and 15).

One individual analysis in each of the following samples BG139.25, 159.90 and 285.30 showed anomalous higher or lower temperature values compared to the other individual analysis of the same sample. The anomalous temperature individual analysis presents a great variation in the Fe/(Fe+Mg) ratio, Al (IV) and Si (apfu) values compared to the other individual analysis of their respective samples.

In terms of interpretation, the geothermometric chlorite formation data must be considered as the minimum value of the maximum temperature that each sediment sample have reached. Therefore, chlorite geothermometry data suggest that studied sediments have potentially reached temperatures higher than those recorded at the time of chlorite formation (i.e. higher than 150°C ±49 or 250°C ±37).

2.3.4. Stable Isotopes

2.3.4.1. Carbon and Oxygen in Calcite crystals

In order to compare igneous- and sedimentary-hosted calcite crystals isotopic signatures, calcite samples were collected from amygdules, aplites and veins in dolerite and from veins and cements in sedimentary rocks. Calcite samples collected in sedimentary and igneous rocks plot in separately clusters in a vs. $\delta^{13}C_{V\text{-}PDB}$ diagram with a few exceptions (Fig. 12). $\delta^{13}C_{V\text{-}PDB}$ values varies from -8.58 to -5.12‰ and $\delta^{18}O_{V\text{-}PDB}$ from -21.18 to -6.62‰.

Calcite from igneous rocks have $\delta^{18}O_{V\text{-}PDB}$ values varying from -21.01‰ to -6.62‰, clustering around -20.50‰. Despite of limited number of analysis, a decreasing trend of $\delta^{18}O_{V\text{-}PDB}$ values towards the contact with sedimentary rocks occur. Amygdule and vein samples present a general increase trend towards $\delta^{13}C_{V\text{-}PDB}$ values range from -6.20‰ to -5.37‰, showing more homogeneous values.

Calcite from veins crosscutting sedimentary rock have $\delta^{18}O_{V\text{-}PDB}$ values varying from -21.18‰ to -8.15‰, with an average of -11.13‰, and $\delta^{13}C_{V\text{-}PDB}$ values varying from -8.58‰ to -5.12. Up to 10m above igneous intrusion, sedimentary-hosted calcite vein samples present a decrease trend of $\delta^{13}C_{V\text{-}PDB}$ values reaching the lowest measured value of -8.58‰, showing a fractionation of the order of 3‰. Above this point, $\delta^{13}C_{V\text{-}PDB}$ values show an increase trend reaching values similar to those immediately above igneous intrusion at depths between. On the other hand, $\delta^{18}O_{V\text{-}PDB}$ values of sedimentary-hosted calcite cluster between -15 and -10‰ with a single exception of the sample 276.3m that presented the lowest value among of -21.18‰. Regardless the host rock, both igneous- and sedimentary-hosted calcites present similar range of $\delta^{18}O_{V\text{-}PDB}$ values.

2.3.4.2. Sulfur in Pyrite crystals

Pyrite occurs in igneous and sedimentary rocks. In dolerite, pyrite occurs disseminated and filling amygdules. In sedimentary rocks, it occurs as disseminated agglomerated crystals, single dispersive crystals, filling veins and as massive layers (Fig. 6, Fig. 7). Analysed samples $\delta^{34}S$ values vary from -4.7 to 11.6‰. Two igneous hosted pyrites samples present $\delta^{34}S$ values of 3.3‰ and 0.9‰ (Fig. 13). Pyrite filling veins that crosscut the sedimentary rocks near to the contact with the igneous intrusion (303 and 306m samples which are 3.6 and 0.6m from igneous intrusion), present $\delta^{34}S$ values ranging between 1.3 and 4.4‰. In contrast, most pyrite cement in sedimentary rock cluster between +5.0 and +10.0‰, although three samples (142, 148 and 302m) have $\delta^{34}S$ values ranging between -5 and 0‰ (Fig.13). While

pyrite veins in sedimentary rocks present similar $\delta^{34}S$ values to igneous-hosted pyrite veins, pyrite cement hosted in sedimentary rocks are isotopically ligher or heavier than igneous sulfur.

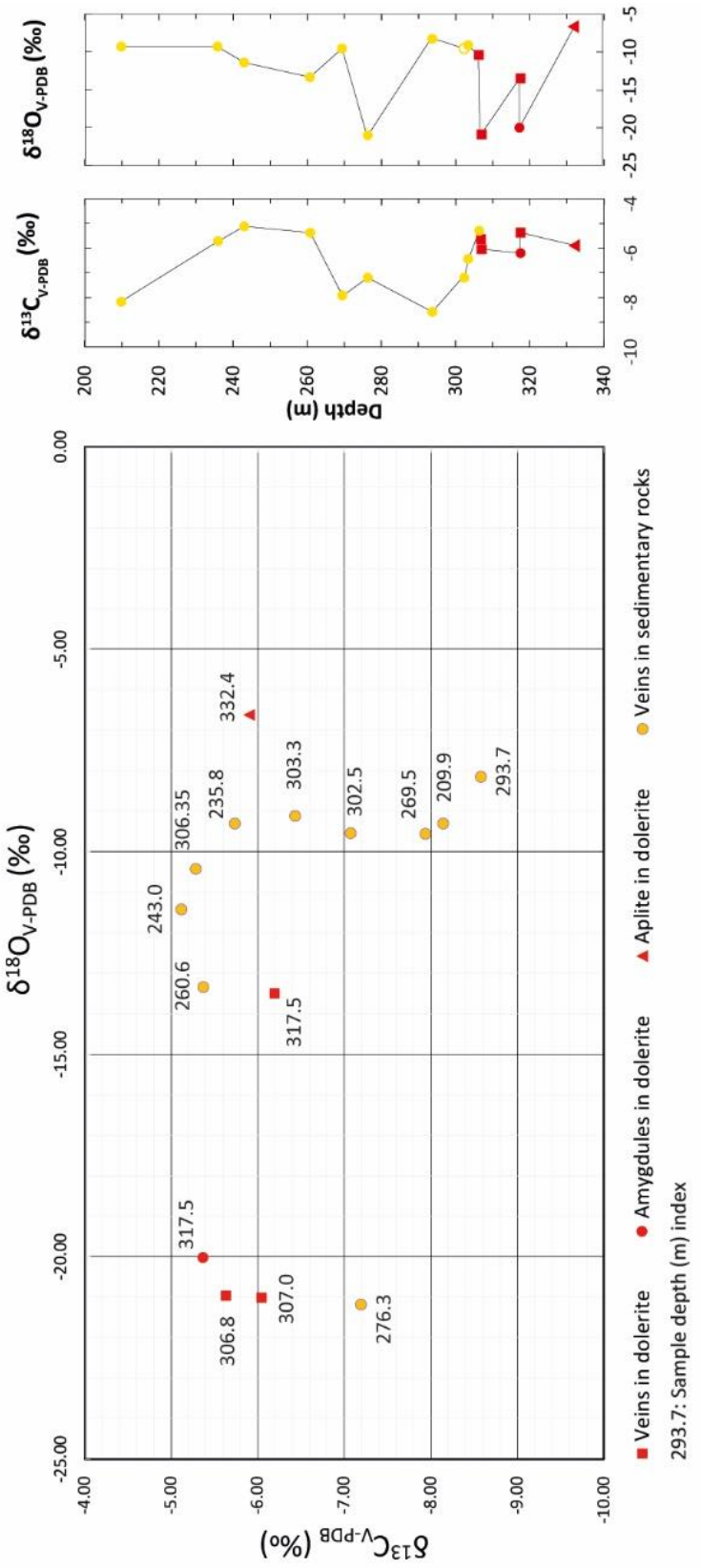

Figure 12. Plot showing sedimentary rock calcite cluster along $\delta^{18}O_{V\text{-}PDB}$ -10.00‰ axis and igneous rock calcite clustering around -20.50‰ $\delta^{18}O_{V\text{-}PDB}$ and -5.8‰ $\delta^{13}C_{V\text{-}PDB}$ in a $\delta^{18}O_{V\text{-}PDB}$ vs. $\delta^{13}C_{V\text{-}PDB}$ graph. On the righthand side, $\delta^{13}C_{V\text{-}PDB}$ and $\delta^{18}O_{V\text{-}PDB}$ values are plotted against depth to highlight vertical variations.

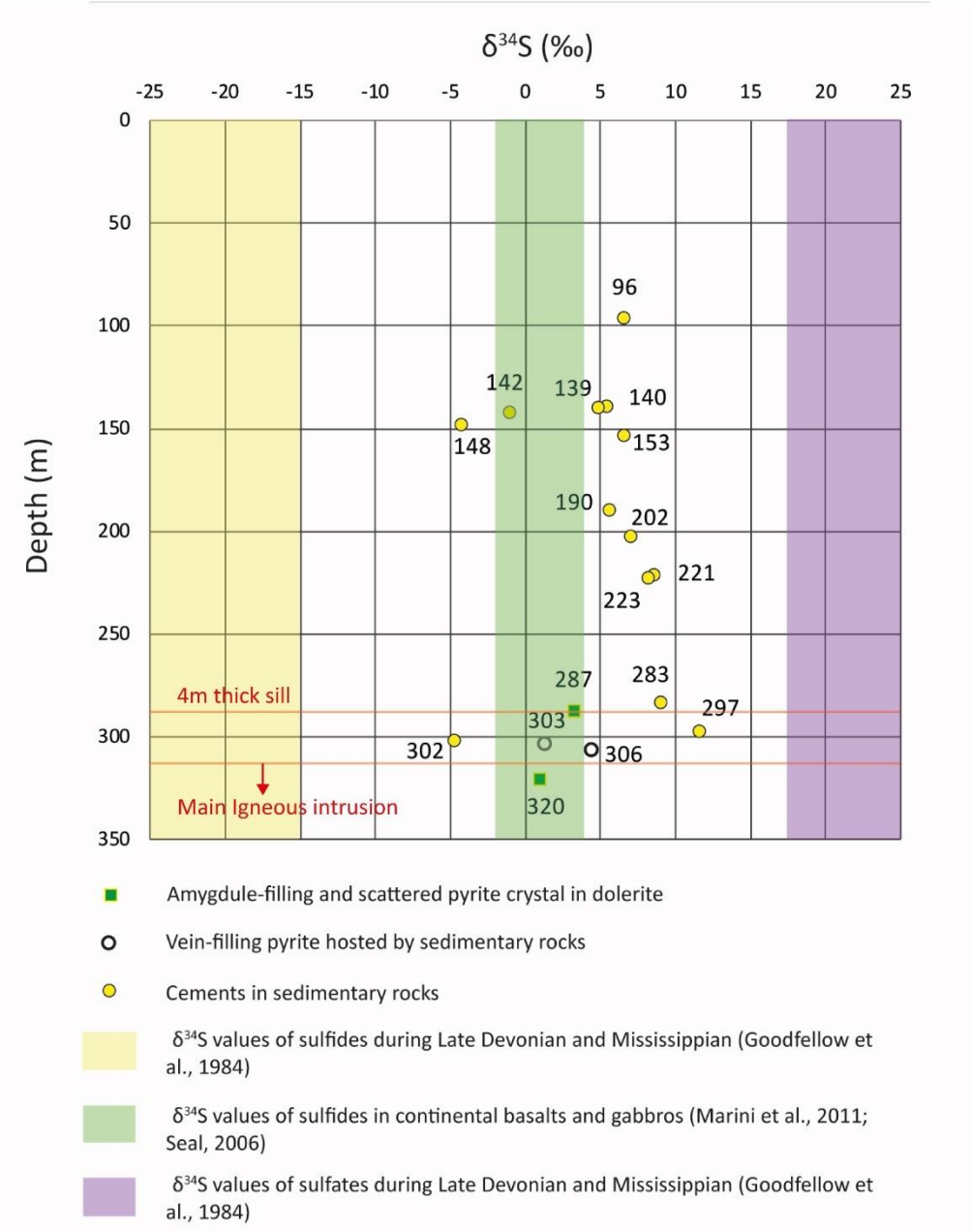

Figure 13. Pyrite $\delta^{34}S$ (‰) values plotted by depth of occurrence along the BG-1-MA well.

2.3.5 Petrophysical Data

Porosity(Φ) and permeability (k) data have a weak correlation ($R^2 = 0.288$) with values varying in a wide range from 0.19 to 34.63% and 0.28 to 830.00 mD, respectively (Fig. 14A). Reservoir Quality Index (RQI) and the Normalized Porosity Index (NPI or Φ_z) vary from 0.004

to 0.0193 and 0.002 to 0.530 with averages of 0.053 and 0.530, respectively. Flux Zone Indicator (FZI) values vary from 0.022 to 48.097 with an average of 0.722 (Fig. 14B). Gathering geological data from well core description and normalized cumulative RQI data (i.e. main slope changes in the NCRQI vs. depth plot – Fig. 15), the studied sedimentary succession was divided into four main reservoir zones. Along the studied well core, there is a general increasing trend of the RQI, NPI and FZI averages from Reservoir Zone 4 to 1, but each zone presents a wide range of values of similar magnitudes (Fig. 15).

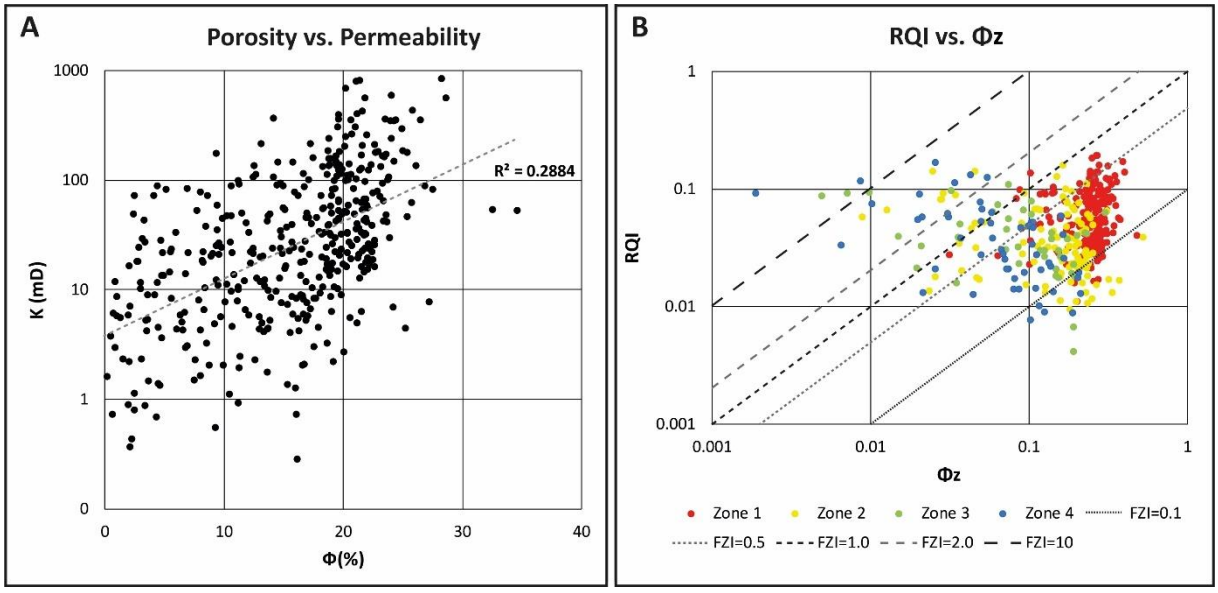

Figure 14. A) Porosity vs. Permeability graph showing a wide range of values but with some correlation between the two parameters. **B)** Normalized porosity (Φz) vs. Reservoir Quality Index (RQI) graph with sample values plotted by reservoir zones and with Flow Zone Indicators (FZI) values plotted as lines.

Zone 4 is composed of the Longá Formation heterolithic sandstones that are close to the igneous intrusion and shows an average porosity lower than 10% and permeability varying from 1 to 100mD (Fig.15). The highest porosity values intervals within this zone are immediately above the main igneous intrusion. Zone 3 is composed of the Longá-Poti and the lower part of the sedimentary succession I. It is highly heterogeneous with values of porosity varying from close to 0 up to 17% and permeability from 1 to 100mD with an average around 10mD. At the top of Zone 3, a peak of permeability (>100mD) and low porosity (<10%) is associated with a heavily cemented medium-grained sandstone layer (Fig.15). The Zone 2 is

composed of the sedimentary successions I (upper part) II, III and IV and presents similar porosity and permeability ranges and averages compared to the Zone 3, but sedimentary stratas are thicker, resulting in a lower heterogeneity frequency (Fig. 15). Zone 1 comprises the sedimentary successions IV, V, VI of the Poti Formation and the lower portion of the Piauí Formation. It shows a high increase in porosity and permeabilities averages, 20% and 100mD, respectively.

Within each of the four zones, there are smaller scale shifts in the normalized cumulative RQI (black dashed lines in Fig. 15) that present a great correlation with the stratigraphic surfaces of maximum flooding surfaces and sequence limits (blue and red lines in Fig. 15). Generally, normalized cumulative RQI present better quality (gentle slopes) above maximum flooding surfaces (light blue lines) and worse (steeper slope) below it and the opposite trend occurs for the sequence limits (red lines) (Fig.15).

2.4 Discussion

The main diagenetic processes in the studied succession of the Parnaíba basin (i.e. Longá to Lower Piauí Fm.) are related to eodiagenetic and mesodiagenetic processes caused by progressive burial of deposited sediments (De Araújo 2018, Góes 1995). The eodiagenetic processes are marked by mechanical clay infiltration via previously formed bioturbation or not; feldspar overgrowth; silicification; chemical and mechanical compaction. While mesodiagenetic processes are marked by quartz overgrowth; smectite cementation; precipitation and dissolution of calcite, siderite and dolomite (de Araújo, 2018; Góes, 1995).

Subordinately, these studies have also reported other diagenetic processes of minor occurrence (e.g barite precipitation and dissolution, replacement of mudstone fragments by illite, chlorite, pyrite and dolomite). However, the thermal history of the basin (Cardoso Jr. et al., 2020; Dias et al., 2017; Rodrigues, 1995; Zembruscki and Campos, 1988) and the occurrence of the two Mesozoic magmatic events indicates that some of the Parnaíba basin

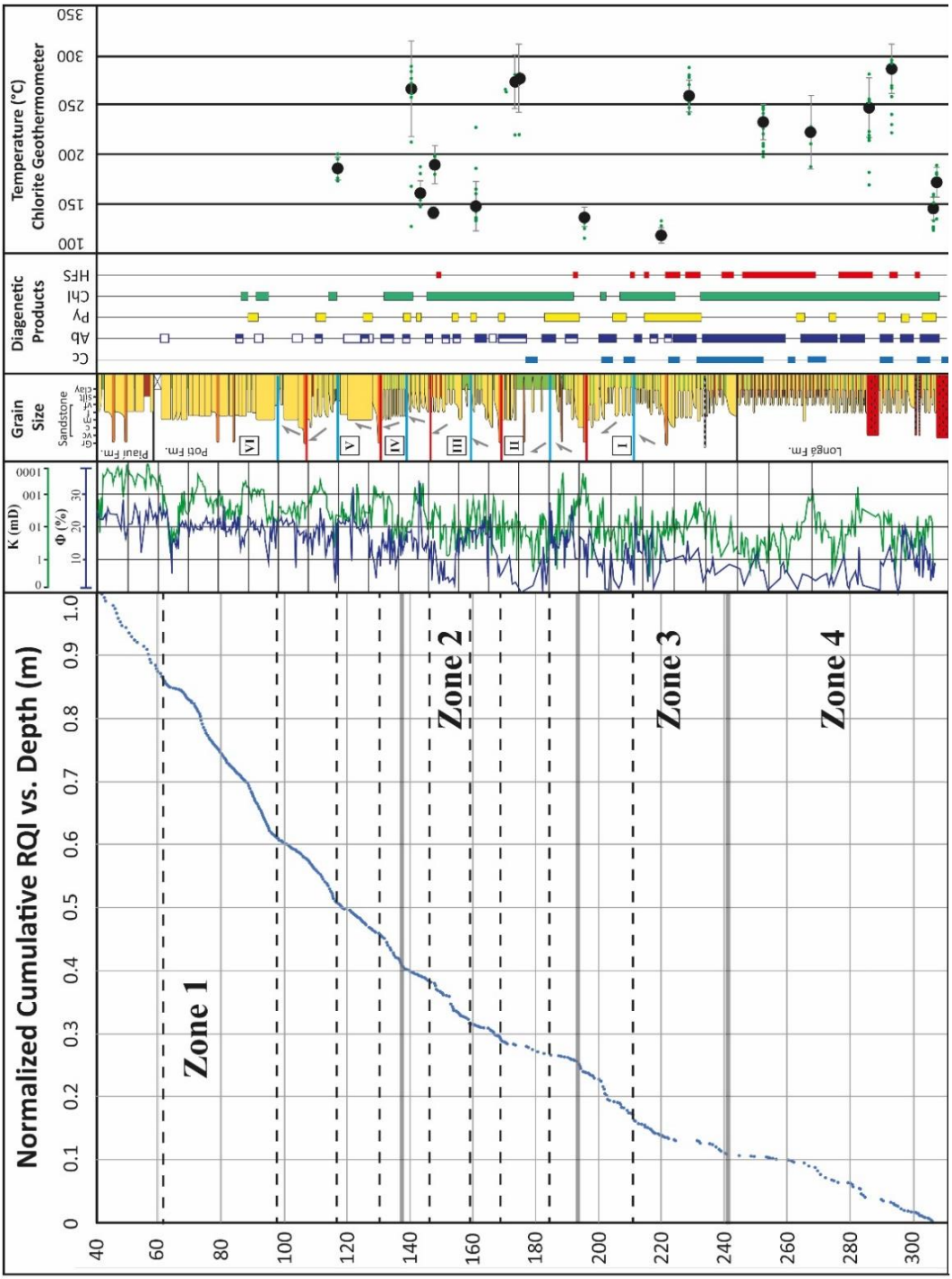

Figure 15. Normalized cumulative reservoir quality index vs. depth graph divided into reservoir zones with the stratigraphic column divided into stratigraphic sequences on its right side, followed by the main diagenetic alterations and the chlorite temperature of formation geothermometric data. The dark blue rectangles are microcrystalline albite occurrences and open rectangles are albite overgrowths.

sediments and the studied samples may have a more complex diagenetic history than only simple normal burial diagenesis.

The 1-FL-1-PI well which is a ca. 36 km to NW from the studied well reaches the basement at 2374m of depth (Zembruscki and Campos, 1988). In a progressive burial diagenesis scenario, considering that sediments in the studied area could be buried to depth

of 2374m, maximum temperature would have been no higher than 75°C assuming an average geothermal gradient of 19.4 °C/km and a surface temperature of 27.7°C proposed by (Zembruscki and Campos, 1988). Average geothermal gradient and surface temperature are reasonable for cratonic basins (Girard et al., 1989; Zembruscki and Campos, 1988).

Diagenetic signatures and geothermometry data presented in this study reveal that Longá, Poti and Piauí formations have been subjected to three different diagenetic phases: progressive burial diagenesis, heat and mass transfer induced diagenesis triggered by igneous intrusions; and telodiagenesis. Each phase will be further discussed in the following topic. In addition to the diagenetic and geothermometry fingerprints, carbon and sulfur isotopic fingerprints of igneous intrusion influence on reservoir rock, mineral changes, heat transfer mechanisms and implications to petroleum system will be discussed on this section.

2.4.1. Progressive Burial Diagenesis

Considering the progressive burial diagenesis products described by de Araújo (2018) and Góes (1995) and the above mentioned temperature (<75°C) and maximum burial depth (2374m), the normal burial diagenesis phase may have occurred under conditions of eodiagenesis to shallow mesodiagenesis described by Morad et al. (2000).

Ductile plastic deformation of soft mudstone lenses, intraclasts and grain contacts register the effects of chemical and mechanical compactions. Detrital micas may have been deformed, bent and even replaced by biotite, suggesting sequestration of Fe^{2+} and Mg^{2+} by the deformed mica and a release of K^{+} and Al^{3+} to the pore fluid. This cation exchange processes may also compose the open system mechanism previously proposed (Aagaard et al., 1990), in which mudstones are source and sink of cations. In this case, mica in sandstone may have exchanged cations with nearby mudstones. A second hypothesis is that this specific compaction reaction (i.e. biotite replacing mica grains) have occurred under the influence of Mg- and Fe-enriched hydrothermally influenced pore-water conditions.

The grain contacts vary depending on the initial composition of the rock. Sutured grain contacts are associated with clay mineral poor sandstones of the upper portion of the Poti Formation and the Piauí Formation and floating grains in muddy sandstones of the lower portion of the Poti Formation and Longá Formation. Although the studied sediments have suffered differential compaction effects, the predominance of long and tangential grain contacts suggest that limited mechanical compaction has acted on the studied sediments (Wilson and McBridge, 1988).

Petrographic observations indicate that albite overgrowth over K-Feldspar grains seems to have been formed before mechanical compaction (Fig.4 G-I) in agreement with the previous description by Araújo (2018) and Góes (1995). However, in the studied samples, mechanical compaction was not pervasive along the studied interval, so textural chronological relationship is not observed over the entire sedimentary succession. In addition, occurrence of albite overgrowths and microcrystalline albite as cement, replacing mudstone lenses and intraclasts, and as bleached rims along contact surfaces of sandstone-mudstone and veins-mudstones suggest that at least two phases of authigenic albite precipitation have occurred along the diagenetic history. The earlier one is associated with progressive burial eodiagenesis processes and the later associated with the magmatic events influence on diagenesis which will be further discussed in the following subsection.

Albite overgrowths over K-feldspar commonly occur over a wide range of temperature from 65 to 150°C, but particularly over 90°C (Aagaard et al., 1990; Saigal et al., 1988). Thermodynamic and mass constraints show that, in an open system, albitization processes are more sensitive to potassium removal than to sodium supply (Aagaard et al., 1990). The frequent intercalation of mudstone and arkoses/subarkoses may have favoured the supply and removal of Na^+ and the removal of K^+ connecting arkosic sandstones and interbedded mudstone that work as sink and source of Na^+ and K^+ as suggested by Aagaard et al. (1990). We argue that albitization process during progressive burial diagenesis depends more on the

chemistry of the pore water during early stages of eodiagenesis than on temperature as proposed by De Ros *apud* Góes (1995).

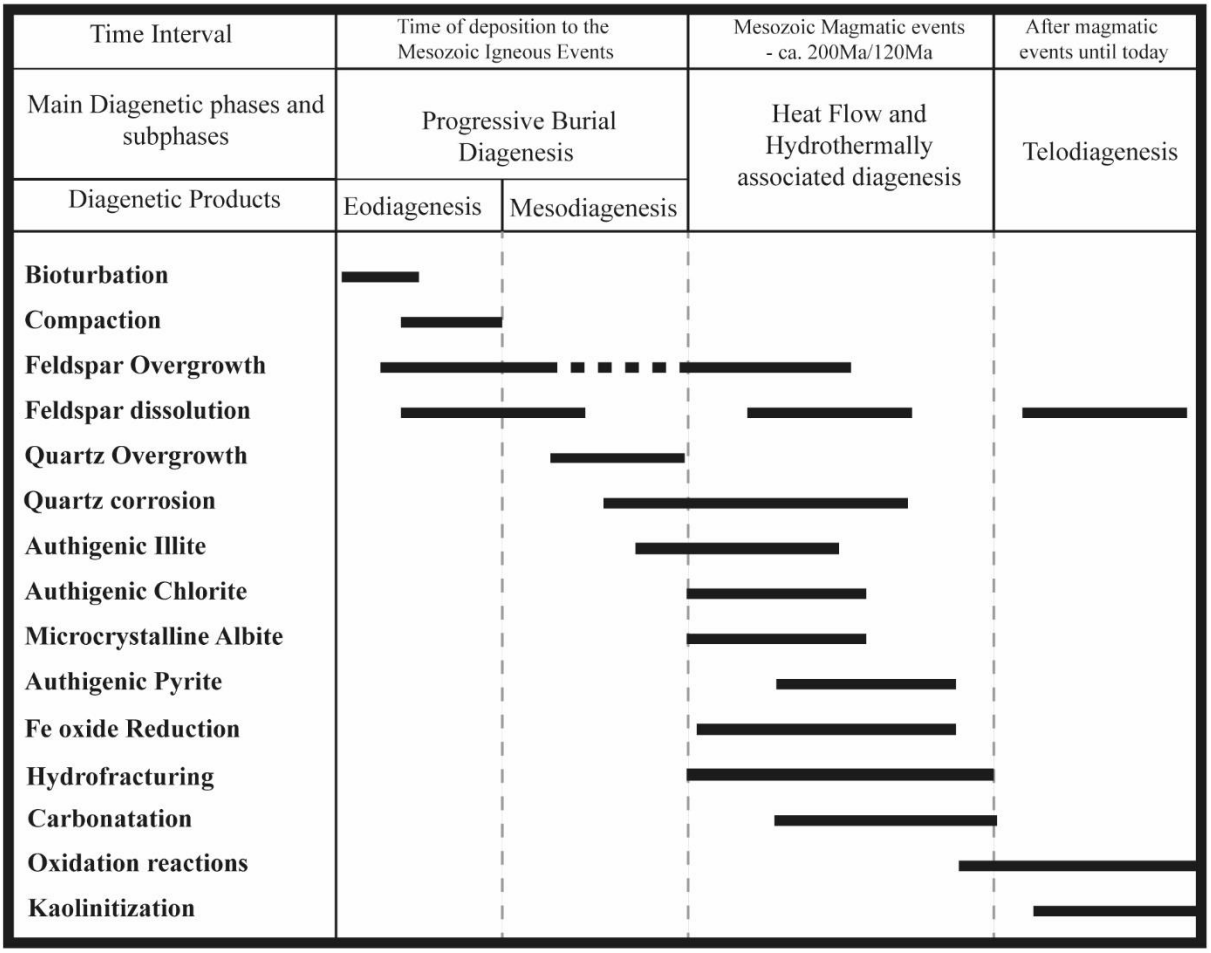

Figure 16. Main diagenetic phases of reservoir rocks with igneous intrusion influence.

Feldspar dissolution is an important parameter on the generation of secondary porosity in arkosic sandstones (Morad et al., 2010; Yuan et al., 2019). K-feldspar detrital grains with albite overgrowth tends to dissolve more than their albite overgrowth rims and dissolution tends to be more effective along the contact of the two minerals. (Fig. 4). During eodiagenetic conditions, more specifically at temperatures below 145°C and pH of 4 to 7, K-Feldspar dissolution is always faster than albite growth and they are coeval processes (Aagaard et al. 1990). In addition, the temperature increase caused by igneous intrusion favours feldspar dissolution in the later hydrothermally induced diagenetic phase (Yuan et al., 2019). Therefore,

feldspar dissolution may have occurred in more both progressive burial diagenesis and hydrothermally induce diagenesis phases (Fig. 16).

Quartz overgrowths described in this study occur as thin rounded rims, represent a low percentage of total authigenic minerals and occur corroded by later cementation processes as reported by De Araújo (2018) and Góes (1995). Pervasive quartz cementation generally occurs at depths greater than 2500m and temperature above 90°C, but it may also occur as a minor cement at lower temperatures such as those of normal burial diagenesis of the studied samples (depth <2000m of and T<80°C) (Giles et al., 2000; Haszeldine et al., 1984; Taylor et al., 2010). Under these conditions, (ie. low temperature and low silica solubility), quartz cementation may be kinetically controlled and associated with K-feldspar dissolution and illitization of smectite as these processes can be a source of silica (Haszeldine et al., 1984; Taylor et al., 2010; Worden and Morad, 2000).

Quartz overgrowths are associated with low clay content sandstones which favours the occurrence of pressure solution between framework grains (Fig. 4) (Araújo, 2018; Folk, 1980; Góes, 1995; Morad et al., 2000). Quartz grains dissolution is more pervasive and seams to represent a more important space opening process than quartz overgrowth as a pore-occluding process in the studied sediments. Although quartz corrosion is associated with late progressive burial diagenetic processes of carbonate cementation (de Araújo, 2018; Góes, 1995), in this study quartz corrosion mainly occur due to chlorite and pyrite mineralization.

In the Poti Formation, carbonate cements are one of the main pervasive and pore occluding mineral with minor occurrences of chlorite and pyrite cement (Araújo, 2018; Góes, 1995). In the present study, carbonate minerals are restricted to veins, breccias cements, and it is also commonly found in high poroperm media near carbonate veins (Fig. 6A-D, Fig. 9 A-E, Fig. 11). The limited interval of occurrence close to the igneous intrusion and $\delta^{13}C$ values within mantle carbon values suggest that these carbonates are not associated with normal

burial diagenesis process but with hydrothermal sources. If carbonate and pyrite cementation have occurred during eodiagenesis and mesodiagenesis phases as suggested in the literature, they might have been remobilized or consumed by later diagenetic phases due to the heat and mass transfer associated with the igneous intrusion, specially due to the addition of CO_2 and SO_2 by the degassing of the igneous intrusion (Giggenbach, 1988 and references therein). Another possibility is that carbonate and pyrite cementation described in the literature may present a regional hydrothermal influence as proposed for the Taoudeni basin by Girard et al. (1989). However, more isotopic studies is required to better determine the elements origin of authigenic carbonate and pyrite cements.

2.4.2. Hydrothermally Induced Diagenesis

2.4.2.1. Thermal History and Thermal Fingerprint of Igneous Events

In the Parnaíba basin, heat provided by igneous intrusions generated an anomalous geothermal gradient and increased the maximum temperatures of the sedimentary rocks and basement rocks at local and regional scales (Cardoso Jr. et al., 2020; Dias et al., 2017; Miranda, 2014; Rodrigues, 1995).

Geothermometric data indicate that both source rocks (Source Rock Analyzer data - Miranda, 2014; Rodrigues, 1995) and reservoir rocks (Apatite and Zircon Fission Track Analysis - AZFTA) (Cardoso Jr. et al., 2020) close to igneous intrusion have reached temperatures from 130°C up to 559°C, with values greater than 367°C only reported in source rock analysis. Chlorite formation empirical geothermometric data of this study have generated temperature values of similar ranges (79-340°C) with averages varying from 112-295°C. Chlorite formation temperature data is similar to the zircon fission track temperatures (123-367°C) obtained from reservoir rocks intruded by igneous intrusions(Cardoso Jr. et al., 2020).

In addition, the high- and low-temperature plateaus of the studied samples (250°C ±37 and 150°C ±49, respectively) present a similar behaviour with the high- and low-temperature groups of geothermometric data (>300°C and <150°C, respectively) presented by (Cardoso Jr. et al., 2020)(Fig. 15). This same author suggested that the highest temperature values are related to local heat flow influence and the lowest temperature values to regional influence of igneous intrusions over sedimentary rocks as temperature values higher than 80°C are not expected in the studied area. A similar origin may be applied to chlorites formed in different temperature reported in this study. Another hypothesis is that low- and high- temperatures chlorite may have formed in different moments of a hydrothermal fluid migration or may have formed by different types of heat and mass transfer mechanisms that will be further discussed in a following topic.

Regarding the recommended use of empirical chlorite geothermometers as a complementary method and not the only geothermometric method, the use of appropriate Fe/Fe+Mg ratio and geological setting proved to be in agreement with the reported apatite and zircon fission-track data used in the same geological setting (Cardoso Jr. et al., 2020). Although chlorite composition and AFTA and ZFTA were not directly calibrated, they were carried out in similar sedimentary succession interval and distance from igneous intrusion in the very same basin region only separated by 80km.

2.4.2.2. Diagenetic Signature of Hydrothermal Influence on Reservoir Rocks

Diagenetic products associated with heat and mass transfer from igneous intrusion into sedimentary rocks described in this study (Fig. 17) are similar to those described for deep mesodiagenetic products of progressive burial diagenesis at temperatures higher than 100°C and depths higher than 3km (e.g. chlorite, albitization, illitization, sulfide precipitation) (Morad

et al., 2000). However, deep mesodiagenetic and hydrothermally induced diagenesis processes differ regarding the duration, origin and source of elements.

Once the eodiagenesis high pore-water flow rates of meteoric water ends, the bulk mineral composition of the sediments should remain nearly constant during progressive burial because of limited pore water flow (Bjørlykke and Jahren, 2012) and the diagenetic reactions occur due to long term increase in temperature. Therefore, progressive burial diagenetic products strongly depend on the sediment environment of formation and on the composition of eodiagenetic products.

In contrast, sediments under the influence of high pore-water rates of hydrothermal fluids are submitted to short term and rapid increase in temperature and are affected not only by heat flow associated with igneous intrusion but also by mass transfer mechanism (Ahmed, 2002; Bjørlykke and Jahren, 2012; Duddy et al., 1994). The significant increase in chlorite, pyrite, albite, calcite and iron-oxides content in the studied samples close to the igneous intrusions may be related to an open system associated with high pore-water flow rates and mass transfer mechanism of hydrothermal origin (Fig. 5, 15; Appendix A). These hydrothermal open systems have caused bulk chemical enrichment in Fe, Mg, S and CO_3 of the sediments and caused favourable precipitation conditions for the above-mentioned minerals. An input of Fe, Mg, S and CO_3 into sedimentary rocks may be associated with igneous intrusion degassing and alteration and pore-water fluid migration (Ahmed, 2002; Giggenbach, 2003).

Considering Bjørlykke and Jahren (2012) assumption of a near closed-system during progressive burial, the chlorite replacing intraclasts and pyrite occurrences reported by De Araújo (2018) could be related to a minor influence of hydrothermal fluid migration that has opened the system and caused an input of iron. Long distances with no local evidence of igneous intrusion presence mineral alterations by hydrothermally-induced diagenetic processes are reported in the Taoudeni Basin by Girard et al., (1989). However, further analysis should be carried out in larger areas of the basin to prove the extent of regional and

local influence of these hydrothermal systems associated with igneous intrusions (e.g. stable isotopes, apatite fission track, fluid inclusion analysis, and others).

Regarding the primary composition of detrital grains, heat and mass transfer from igneous intrusion presents stronger influence over minerals that are more susceptible to react under the new physicochemical conditions (e.g. minerals that are unstable at high temperature). Among the primary minerals, clay minerals are the most unstable minerals due to temperature increase and tend to react and form authigenic minerals (Sant'Anna et al., 2006; Santos et al., 2009). Illite, chlorite and biotite are the main authigenic clay mineral phases in the studied samples. The increase in temperature (> 100°C) due to heat transfer may have caused the transformation of unstable clay minerals (e.g. smectite and kaolinite) into illite and chlorite (Morad et al., 2000; Worden and Morad, 2003). In addition, the Fe and Mg input due to mass transfer mechanism may have favoured chlorite formation over other clay mineral phases. The presence of kaolinite content higher than 1% close to the igneous intrusion (Table 1, Fig. 5, Appendix A) may be associated with dehydration and endothermic reactions (Holness and Watt, 2002; Rodrigues, 1995; Santos et al., 2009). Another hypothesis is that hydrous high-temperature mineral precipitation (e.g. illite and chlorite) may be hindered by instant pore-water expulsion by the time of igneous intrusion. Authigenic kaolinite close to igneous may have formed in a later cooler phase.

Smectite and kaolinite occur in minor contents in the studied samples (<1%), but they are the main authigenic minerals in sedimentary rocks without igneous intrusion effects (Góes, 1995). This fact supports that smectite and kaolinite may have been recrystallized into chlorite and illite due to temperature increase. In addition, the illitization of smectite and kaolinite during the hydrothermally induced diagenesis may have generated a sodium-rich alkaline pore water that favoured a second generation of K-feldspar grains albitization in the middle and upper portions of the Poti Formation (Ahmed, 2002; Brauckmann and Fuchtbauer, 1983; Morad, 1990). Rounded shape and occurrence in low porosity and permeability mudstones suggest in-situ precipitation of the microcrystalline chlorite crystals probably replacing previous stable

clay mineral, probably illite, smectite or an interstratified phase. Conductive heat transfer from hydrothermal fluid migration or from igneous intrusion may have caused temperature increase due to the low permeability of mudstones (Aarnes et al., 2011b; Santos et al., 2009). Detailed X-ray and Back-scattering electron images studies are required for further information about textural relationship and identification of mixed-layer clay mineral phases.

Closer to the igneous intrusion, the hydrothermal fluid alkalinity (Girard et al., 1989; Holness, 1999; Holness and Watt, 2002; Yuan et al., 2019) may have favoured the precipitation of microcrystalline albite in pore-spaces, replacing mudstone detrital grains, generating bleached mudstone rims around sandstone layers and veins. The elevated heat flow, high nucleation rate, elevated pore-water temperature may have favoured the precipitation of microcrystalline albite instead of albite overgrowths (Ahmed, 2002). Authigenic albite formation associated with hydrothermal fluid migration is also reported in similar geological settings in the Ulster, Hartford, Taoudeni and Paraná basins (Ahmed, 2002; Girard et al., 1989; Sant'Anna et al., 2006).

The presence of bleached rims on mudstones around high permeability medias (sandstones and veins) suggest that the adjacent mudstone and the fluid migration media have worked as an open system. Exchange of alkaline and alkaline earth cations between mudstone clay minerals and the hydrothermal fluid may have favoured the authigenic mineralization along the porous sandstones (i.e. fluid migration media) and the precipitation of microcrystalline albite aureole in the adjacent low permeability mudstone layers. The illitization of previously formed smectite in mudstones and illitization of kaolinite in sandstones may have favoured the precipitation of albite along mudstone rims due to the K^+ removal from mudstones. In addition, the occurrence of microcrystalline albite aureoles in mudstones crosscut by veins crosscut support that an open-system disequilibrium reaction of clay minerals from mudstone and hydrothermal fluids took place in the mudstone-hydrothermal fluid migration media surface.

The hydrothermal fluid rich in Fe, Mg, CO_2, H_2S, SO_2 and base metals provided by the igneous intrusion (Ahmed, 2002; Brauckmann and Fuchtbauer, 1983; Giggenbach, 1988) through mass transfer mechanism are probably associated with the precipitation of Fe- and Mg-chlorites, calcite, pyrite ± chalcopyrite. This is supported by the stable isotopic data of pyrite and calcite that suggest a magmatic origin for sulfur, and carbon isotopes. The authigenic mineralization of chlorite, iron oxides, pyrite, microcrystalline albite and carbonates in the pore space occur in circular mineral domains (nodules) (Fig. 6, 8, 10, 12) resulting in a spotted texture in sandstone and mudstones. This texture is interpreted as a response to the authigenic mineral growth under hydrothermal/contact metamorphism conditions (Aarnes et al., 2011; Grapes, 2011; Miranda, 2014). Although physicochemical conditions are similar, this study have followed the term hydrothermally induced diagenesis to refer to the heat flow and hydrothermal fluid migration triggered by igneous intrusion as suggested by Ahmed, (2002), Haile et al., (2019) and Girard et al., (1989). Illite is the main clay mineral identified in unaltered domains of mudstones and sandstones with spotted textures (Fig. 6, 7, 8). Then, microcrystalline albite may have replaced illite in a high-temperature, reductive environment in which K^+ may have been leached and hydrothermal fluids or sandstones may have been a source of Na^+.

The corroded quartz aspect may be related to quartz dissolution by the hydrothermal fluid due to the increase in temperature and perhaps an increase in pH values higher than 7 (Girard et al., 1989; Kennedy, 1950; Siever, 1962; Utami et al., 2014; Williams et al., 1985). The magnetism presented by microcrystalline iron oxides clusters scattered in mudstones may occur due to iron reduction caused by the hydrothermal fluids as proposed by Holness and Isherwood (2003) and Robinson and McClelland (1987).

2.4.2.3 Brittle and Ductile Structures Associated with Heat Flow and Hydrothermal Fluid Migration

Brittle structures in the studied well comprises a great variety of types and its frequency of occurrence increase towards igneous intrusions (Fig. 3 and 15) suggesting that igneous intrusion may have triggered pore water migration and/or were a source of local stress (Rabbel et al., 2020). Igneous intrusion may have generated natural hydraulic fractures due to the overpressure of hydrothermal fluids migration (Jamtveit et al., 2004; Philipp et al., 2013). Dehydration reactions and hydrocarbon generation may also have contributed to generate overpressure fluids in the organic- and clay-rich layers of the Longá Formation and as suggested by Holness and Watt (2002) and Aarnes (2010). Mandl and Harkness (1987) proposed that natural hydraulic fractures are extension fractures caused by fluid pressure overcoming the tensile strength. Hydraulic fracture is also defined as a fracture partly or wholly generated by internal fluid pressure and it is very well stablished for fluid-driven rock fractures (natural or man-made) (Philipp et al., 2013 and references therein).

In the present study, three types of hydrofractures related to hydrothermal fluids have been recognized: (1) horizontal veins and breccias filled with calcite (Fig. 11 F-H); (2) layer parallel to obliquus and breaching hydrofractures forming an anastomosing array (Fig. 9 A-D); (3) beef-like horizontal discontinuous structures composed of microcrystalline chlorite and lath-shaped opaque minerals (Fig. 9 E-I). These structures occur in mudstones and siltstones and mudstones laminations in distances up to 110m above the igneous intrusion.

Carbonate veins and breccias occurrence are limited to the top of the Longá Fm. and the lower portion of the Poti Formation and are controlled by previously existing structures (i.e. faults and sedimentary/stratigraphic surfaces), suggesting a stratigraphic control of these features. (Gilg et al., 2003; Hangx and Spiers, 2009; Matsui et al., 1974). The $\delta^{13}C$ composition of the carbonate vein and breccia samples (especially the horizontal breccias and veins: 235.8m and 260.6m – Fig. 11) suggest a major contribution of magmatic derived fluids as they

present mantle source $\delta^{13}C_{PDB}$ ‰ values (Fig.17). Considering the stratigraphic interval of occurrence and the stable isotopic signature, the carbonate cemented breccia and horizontal veins are interpreted to be formed by CO_2-rich fluids derived from magmatic intrusions. Vertical migration of this fluid may have occurred along vertical faults that could not be observed in well scale. Lateral horizontal migration may have been favoured by layer-parallel structures weak surfaces in a similar condition of sill propagation mechanism (Eide et al., 2017; Trosdtorf et al., 2018).

Haile et al. (2019) report carbonates remobilization in sandstones caused by igneous intrusion hydrothermal fluid migration in Svalbard, Greenland. However, there is no isotopic study from the Poti Fm. Bivalvia fossils at the Parnaíba basin reported by (Santos and Carvalho, 2009) to support this hypothesis or volumetric evidence that carbonate fossils are a representative isotopic source. Another possible source would be remobilized calcite of marine cements associated with the pervasive calcite cement described by Góes (1995). Although there is also no isotopic study for marine cements in the Parnaíba basin, $\delta^{13}C_{PDB}$ ‰ data compilation of marine cements associated with the main oceans at the time of sediment deposition shows a positive $\delta^{13}C_{PDB}$ ‰ values signature. Carbonate veins and breccias hosted in sedimentary rocks samples cluster within mantle carbon $\delta^{13}C_{PDB}$ ‰ values and their negative signature suggest a major contribution of magmatic sources and little or no contribution from other sources.

Although the source of Ca^{+2} could also be derived from mafic intrusion plagioclase alteration as proposed by Gilg et al. (2003), Hangx and Spiers (2009) and Matsui et al. (1974), this element may also have been partially derived from dissolution of bioclastic fossils and dissolution of unstable Ca- and Mg-bearing non-carbonate minerals caused by hydrothermal fluids migration through sedimentary rocks. Therefore Bivalvia fossils of the lower portions of the Poti Formation and prior carbonate cements could also be minor to major source of Ca^{+2} depending on their volumetric contribution (Góes, 1995; Santos and Carvalho, 2009).

The layer-parallel to obliquus fractures present preferential layer parallel geometry within siltstones and obliquus transgressive fractures within mudstone layers (Fig. 10). Sometimes, vertical microfractures crosscut siltstone layers connecting transgressive hydrofractures of two different mudstone layers. These preferential geometries suggest that hydrofracturing migration pattern is more dependent on the permeability than on the differential stress or anisotropy of the host rock as suggested by Hillier and Cosgrove (2010). Although igneous intrusions and related tectonic Mesozoic events may have controlled overall fracture orientation in a basin scale (Michelon et al., 2019), local stress interactions may cause significant deviations of fracture paths and control the coalescence characteristics of fractures in reservoir scales (Rabbel et al., 2020). The breaching, transgressive to layer-parallel hydrofractures path deviations may be associated to discontinuities, stiffness changes between layers and stress barriers that changes local stress field. The non-stratabound transgressive hydrofractures in mudstone and normal microfractures in interlayered siltstones may increase reservoir vertical permeability and the interconnectivity between layers that were once isolated from each other (Philipp et al., 2013). Homogenization of bioturbated layered may also contribute to the increase in vertical permeability and have controlled hydrothermal fluid migration paths in the studied samples (Needham et al., 2006) (Fig. 7A-D). Miranda et al., (2018) have pointed out the importance of fractures to increase permeability in the Poti Formation.

The beef-like vertically symmetric horizontal discontinuous structures occur mainly as isolated bodies with an external microcrystalline albite rim but may also occur connected to or at least nearby veins (Fig. 10). The vertically symmetrical geometry and horizontal orientation resemble beef structures (Cobbold et al., 2013; Cobbold and Rodrigues, 2007). However, the chlorite and opaque minerals are randomly arranged in contrast with the fibrous vertically orientated as in beef-filling crystals. In addition, there is no chlorite and iron oxide filled beefs reported (Cobbold et al., 2013; Cobbold and Rodrigues, 2007; Rodrigues et al., 2009). While beefs are generated by overpressure fluid related to organic matter maturation, the studied

structures may be related to heat flow and hydrothermal fluid-driven overpressure triggered by igneous intrusions. More studies and examples are required to better understand processes and genesis of these kind of structures.

The only ductile structure described is composed of a rounded sandstone body (10cm) surrounded by mudstone with mineral clusters orientated parallel to the rounded shape of the sandstone body (Fig. 10). Two different genesis processes are proposed to the ductile structure origin. The first hypothesis is that it is fluidization/slump structure generated during eodiagenetic phase that was later modified by hydrothermal fluid migration. And the second hypothesis is that overpressured fluid related to magmatic intrusions may have caused the fluidization of sand and the plastic deformation of mudstones. The second hypothesis is similar to the sandstone fluidization and injections into brittle mudstone layers proposed by Hillier and Cosgrove (2010). However, in the studied case, the increase in temperature may have favoured the ductile deformation showed by the biotite and iron oxide oriented clusters in mudstone and the brittle behaviour would be represented by the chlorite-filled vein that starts/ends at the mudstone-sandstone contact and develops in mudstone domain (Fig. 7)

2.4.3 Telodiagenesis

Telodiagenetic alterations correspond to downwards percolation of meteoric waters to tens to few hundred meters below the surface. This process is characterized by dissolution of unstable minerals, oxidation reactions and kaolinization resulting in an increase in permeability and porosity (Bjørlykke and Jahren, 2012; G. Shanmugam, 2002; Garcia et al., 1998; Morad et al., 2000). In the shallowest levels of the studied well (<65m), there is an increase in kaolinite content and a sharp increase in porosity and permeability (Fig.5 and 15). The presence of iron oxi-hydroxides in similar chlorites and pyrites textures reported in deeper levels, lack of magnetism in the iron oxide occurrences, the change in colour from greenish-grey in the deeper portions to brownish-pale yellow in the shallower portion of the studied core suggest that the former pore-occluding authigenic mineral were oxidized. Overall, the heat and mass

transfer induced diagenesis may have affected sedimentary rocks up to the nowadays surface but telodiagenesis phase have superimposed and altered prior diagenetic mineral phases.

2.4.4. Stable Isotope Fingerprints

2.4.4.1 Sulfur in Pyrite

Pyrite crystals occur in framboidal and cubic habits in the Poti Formation (de Araújo, 2018; Góes, 1995). Miranda (2014) have reported the occurrence of euhedral and framboidal pyrite crystals in the Pimenteiras Formation intruded by igneous rocks in the Parnaíba Basin and have suggested a different origin of these pyrites based on its habits. The framboidal pyrite was associated with eodiagenetic processes and the euhedral pyrite with hydrothermal processes. Taylor and Macquaker (2000) suggest that euhedral and framboidal pyrites can be formed associated with eodiagenetic processes and that the pyrite morphology is controlled by the amount and reactivity of organic matter within the deposited sediments. Graham and Ohmoto (1994) suggest that euhedral pyrites may develop from a framboid when individual pyrite crystal starts to grow and engulf the framboids. Therefore, there is a great divergence regarding the association of pyrite habits to its origin. In addition, the dominant crystal growth mechanism(s) can change over time and the later crystal growth can effectively erase evidence for early crystal growth mechanisms (De Yoreo *apud* Wolf and Gower, 2017). Considering this, sulfur isotopic analyses were carried out to further investigate the origin of the euhedral and anhedral pyrite crystals in the studied samples.

Regarding $\delta^{34}S$ signatures, three main sources of sulfur were considered regarding the geological setting of the studied samples. The first source would be igneous intrusions that are continental basalts and gabbros and present a narrow range of $\delta^{34}S$ values $+1.0 \pm 3.2$ (Marini et al., 2011; Seal, 2006). The second possible source would be early diagenetic sulphides precipitated by bacteria reduction of marine sulphate. The Mississippian seawater sulfates present values around +20‰ and the bacteria reduction would deplete $\delta^{34}S$ by 40‰ in open-

systems (Habicht and Canfield, 1997) producing sulphides with negative values around -20‰ (Claypool et al., 1980; Fallick et al., 2001; Goodfellow and Jonasson, 1984). The third source would be thermochemical reduction of sulfates that may occur by the reaction of upwelling hydrothermal fluids that would produce fluids with $\delta^{34}S$ values of positive values around +17.5‰ (Claypool et al., 1980; Peter and Shanks, 2003; Rodrigues, 1995; Shanks et al., 1981). These three possible sulfur sources may be isotopically distinguishable and provide information on the sources of sulfur.

The pyrite sulfur isotopic composition of igneous rock samples (BG-320 and 287m) yielded $\square^{34}S$‰ values of 0.9 and 3.3‰, respectively, and these values are within the range of whole-rock $\delta^{34}S$ values of continental basalts and gabbros, +1.0 ± 3.2 (Marini et al., 2011; Seal, 2006). $\square^{34}S$‰ values of +4.4‰ and +1.3‰ of pyrite samples of vein hosted by sedimentary rocks (BG-306m and BG-303m) also match continental basalts and gabbros (Fig. 13 and Fig. 17).

Sedimentary rock-hosted pyrite samples cluster into two different $\delta^{34}S$ values intervals groups (Fig.13). The first group is composed of pyrite cement that displays $\delta^{34}S$ values between -5 and 0‰, thus having an isotopic composition similar to pyrite-bearing igneous samples of this study with slightly lighter isotopic composition. The lighter $\delta^{34}S$ values relative to the magmatic sources may be related to partial oxidation of the fluid, forming SO_4, or disproportionation reaction that leads to the formation of HS^- and SO_4^{2-} from SO_2 magmatic fluids (Rye, 1993; Rye et al., 1992). Another possible mechanism that probably had a minor role but also contributes to explain the low $\delta^{34}S$ values is a result of a mixed analysis of $\delta^{34}S$ from igneous sources and prior formed burial diagenetic formed sulfides. No prior stable isotopic study was done by the time of this publication for this sedimentary interval at the Parnaíba basin to proper evaluate diagenetic sulfides isotopic contribution. In addition, S leaching from organic-rich intervals (e.g. Pimenteiras or Longá formations) may also result low $\delta^{34}S$ values (Miranda, 2014; Peter and Shanks, 2003; Rodrigues, 1995). The second group of pyrite have $\delta^{34}S$ values ranging between +5 and +10‰. This group of samples may have some

isotopic contribution from thermochemical reduction of sulfate source during reaction of hydrothermal fluid with aquifer sulfate (at the time of the igneous intrusion), from entrainment or leaching of isotopically heavy previously deposited sulphate or sulfides as proposed by Peter and Shanks (2003) and Shanks et al. (1981). Barite cement in the Poti Formation sandstones reported by Góes (1995) would be a possible sulfate source for this hypothesis. However the rare occurrence of barite cements in the Poti Formation may represent volumetrically limitation of this sulfur isotopic source (Góes, 1995).

Euhedral pyrite in sandstones shows a strong association with mudstone intraclasts and lenses. Taylor and Macquaker (2000) suggest that diagenetic euhedral pyrite crystals are associated with clay pellets as the reactive detrital iron of clay pellets would be the source of iron to form pyrite. Diagenetic crystals precipitate directly from saturated in FeS_2 porewater in sandstones with low reactive organic matter content. Although most of the studied cement pyrite have presented a major $\delta^{34}S$ magmatic signature for sulfur and part of the iron cation supply may also come from the igneous intrusion, at least part of the required iron cation to form pyrite crystals could also be from sedimentary detrital iron.

Although there are at least three sources of sulfur to form pyrite, the clustering of sedimentary samples around 4.6‰ suggests a major contribution of magmatic/hydrothermal sources. More isotopic studies of sulphate cements, organic matter rich intervals and sedimentary pyrites are required to better understand the importance of sulfur magmatic source in pyrite occurrence in the Parnaíba basin.

2.5.4.2 Carbon and Oxygen in Calcite

Calcite occurs mainly as carbonate cemented breccias, veins and vein-associated cement in sedimentary rocks and as amygdules and veins in igneous rocks. Veins and cement hosted in sedimentary rocks occur up to 120m above the igneous intrusions and are mostly associated with mudstones (Fig.6 A, D-E; Fig. 11 and Fig. 3).

Calcite derived from magmatic/hydrothermal sources are associated with the degassing of igneous intrusions and may mix with meteoric water and fluids derived from dissolution of previously formed calcite (Giggenbach, 2003; Haile et al., 2019; Stakes, 1991). Hydrothermal calcite may also have had a contribution of low-temperature meteoric fluids since marine cements have been described in the Poti Formation and later diagenetic dissolution of bioclasts could be possible sources of ions (Girard et al., 1989; Góes, 1995; Santos and Carvalho, 2009).

In a $\delta^{18}O_{V\text{-}PDB}$ vs. $\delta^{13}C_{V\text{-}PDB}$ graph, the calcite studied samples plot close to mafic end-member of the Mid-Ocean Ridge field, and in the interceptions of the Mississippi Valley-type (MVT) lead-zinc deposits, and Paraná geodes fields (Fig. 17). All samples $\delta^{13}C_{V\text{-}PDB}$ values are within the mantle carbon range of values suggesting a major contribution of carbon mantle source.

The calcite vein hosted in sedimentary rocks plot in concordance with the MVT field (Rollinson, 1993), except for the samples BG-260.60 and 276.30m that present lighter $\delta^{18}O_{V\text{-}PDB}$ values plotting in and close to the mafic end-member of the Mid-Ocean Ridge field, respectively (Fig. 13 and Fig. 17). The Mid-Ocean Ridge field variation from the mafic igneous rock end-member (M) to the sedimentary end-member (S) in Figure 17 depends on the influence of seawater/meteoric water, water/rock ratios and temperature variations (Rollinson, 1993; Stakes and O'Neil, 1982). The lighter $\delta^{18}O$ mantle signature of the samples BG-276.30, BG-260.60 and the other igneous calcite samples close to it suggest that calcite was formed with little influence of seawater/meteoric water in conditions of low water/rock ratios and high temperature (145-170°C) in similar conditions to those presented by Stakes and O'Neil (1982).

The MVT field presents a large variability of a $\delta^{18}O_{V\text{-}PDB}$ and $\delta^{13}C_{V\text{-}PDB}$ values. This variability also occur in hydrothermal settings due to the mixture of the following sources isotopic sources of carbon: host carbonate rock ($\delta^{13}C_{V\text{-}PDB} \sim 0‰$), the proximity of mantle-derived or magmatic sources ($\delta^{13}C_{V\text{-}PDB} \sim -6‰$), and the degradation of organic carbon ($\delta^{13}C_{V\text{-}PDB} < -30‰$)

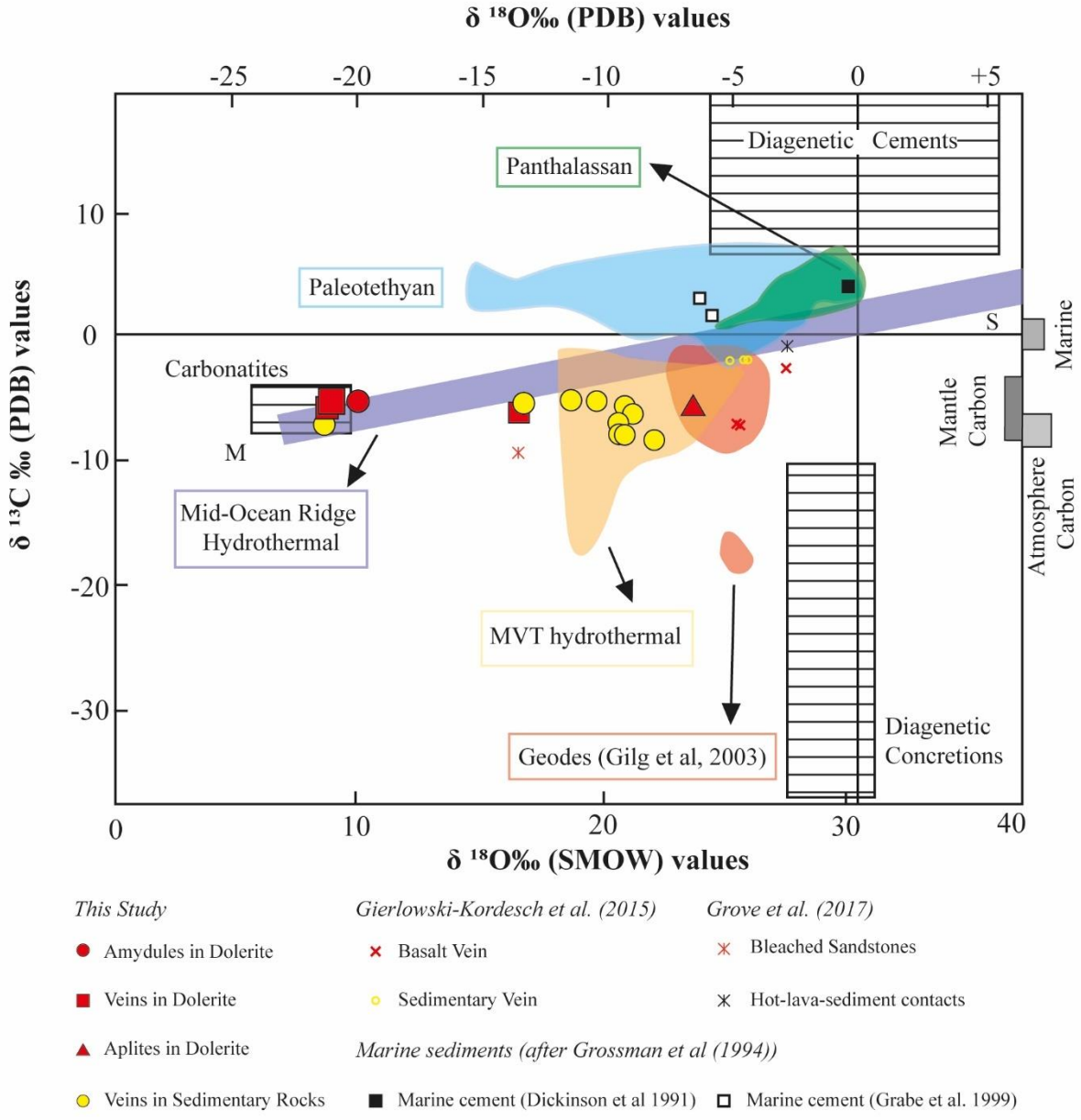

Figure 17. $\delta^{18}O_{V\text{-}PDB}$ vs. $\delta^{13}C_{V\text{-}PDB}$ graph with brachiopods shells of the Panthalassan (Grossman et al., 1993, 1991; Mii and Yancey, 1999) and Paleotethyan oceans (Bruckschen et al., 1999; Popp et al., 1986) during the Mississippian period; marine cements Dickinson *apud* (Grossman, 1994) and Grabe *apud* (Grossman, 1994); geodes of the Paraná Basin (Gilg et al., 2003); igneous and sedimentary calcite (Gierlowski-Kordesch et al., 2015) (Modified after (Rollinson, 1993).

(Peter and Shanks, 2003 and reference therein; Richardson et al., 1988; Rollinson, 1993). Although there are no carbonate rocks in the studied succession, the presence of bivalves at the lower portion of the Poti Formation reported by Santos and Carvalho (2009) and the organic matter degradation caused by the heat input of igneous intrusion (Rodrigues, 1995) may have contributed with $\delta^{13}C_{V\text{-}PDB}$ close to zero and with lighter $\delta^{13}C_{V\text{-}PDB}$ values, respectively, in a

similar way that occur in MVT systems and Mid-Ocean Ridge hydrothermal systems (Leach et al., 2010; Peter and Shanks, 2003; Richardson et al., 1988). The $\delta^{13}C_{V\text{-}PDB}$ values varying from -8.58 to -5.12 presented by the sedimentary hosted calcite samples are very similar to mantle $\delta^{13}C_{V\text{-}PDB}$ values but they may have a minor influence of dissolved bivalve and degraded organic matter $\delta^{13}C_{V\text{-}PDB}$ values.

The igneous hosted calcite samples presented a very small range of $\delta^{13}C_{V\text{-}PDB}$ values (-6.20 to -5.37‰) indicating a very strong contribution of carbon from a mantle source that present mean $\delta^{13}C_{V\text{-}PDB}$ values of -6‰ (Rollinson, 1993). Regarding the variation of $\delta^{18}O_{V\text{-}PDB}$ values, they might be related to differences in meteoric water influence, water/rock ratios, differentiation processes and temperature (Rollinson, 1993; Stakes, 1991; Stakes and O'Neil, 1982).

In igneous rocks, the heavier $\delta^{18}O_{V\text{-}PDB}$ value of the inner chilling margin vein sample (317.50m) compared to the outer chilling margin vein samples (306.8 and 307.0m) suggest that they were formed under different conditions.

The outer chilling margin of igneous intrusions usually crystallize first in relation to the inner parts of the igneous bodies and the volatiles are likely to accumulate on the top of the still liquid interior. During further cooling, if the volatile contents are high enough, it may exsolve to accumulate in vesicles (Giggenbach, 2003). Therefore, the outer chilling margin samples (306.8 and 307.0m) vein samples may have precipitated under different water/rock ratio, temperatures and under depleted in SiO_2 conditions compared to the inner vein samples of the igneous body (317.50) (Chivas et al., 1982; Javoy et al., 1986; Rollinson, 1993).

The amygdule and aplite in dolerite data are represented by only one sample each, so they are of limited statistical use, but when compared to the others they are of qualitative value. Although the amygdule sample (317.50m) is within of what was considered as an inner portion of the igneous intrusion, it presents $\delta^{18}O_{V\text{-}PDB}$ and $\delta^{13}C_{V\text{-}PDB}$ values similar to the outer margin vein samples that may have concentrated lighter $\delta^{18}O$ isotopes during the genesis of the

amygdules. The amygdule lighter $\delta^{18}O_{V\text{-}PDB}$ value may be related to a different stage of degassing of the igneous rock (Javoy et al., 1986).

The aplite sample is enriched in ^{18}O by 7 up to 15 per mil compared to the other igneous calcite samples suggesting the precipitation from a hydrous fluid with heavier $\delta^{18}O_{V\text{-}PDB}$ values. Chivas et al. (1982) suggest that the increase in $\delta^{18}O$ correlates with an increase in SiO_2 content – a measure of the degree of differentiation. This fluid can be an evolved seawater-hydrothermal fluid, perhaps derived from a late hydrous magma (i.e. associated with the aplite genesis process) or a hybrid resulting from mixing between magmatic water and seawater during the waning stages of magmatic activity (Gilg et al., 2003; Stakes, 1991). Although, the aplite sample plot within the Paraná geodes fields in Figure 17 which may indicate that they have formed from similar isotopic sources and precipitation conditions, they may result from different genetic processes. The direct comparison of calcite hosted in igneous and sedimentary rocks proved to be a very useful approach showing that all samples present a major contribution from mantle sources and that there is little or no influence from positive $\delta^{13}C_{V\text{-}PDB}$ sources as marine carbonates and diagenetic cements. However, more data is required to corroborate and better understand the isotopic sources of carbon and oxygen.

2.5.5 Heat Dissipation and Hydrothermal Fluid Migration Mechanisms

The heat of sills and dykes intruded into sedimentary rocks can be transferred by conduction and convection of fluids (Aarnes et al., 2011a; Einsele, 1982; Ferry and Dipple, 1991; Rohrman, 2007). The first generally occur in low permeability rocks where fluid migration is not a significant heat transfer mechanism (Aarnes, 2010). Overpressure structures and contact metamorphism reactions marks thermal effects on low permeability rocks (Aarnes, 2010; Aarnes et al., 2012; Holness, 2002; Holness and Watt, 2002; Iyer et al., 2017; Jamtveit, 1992; Jamtveit et al., 2004). Spotted texture of chlorite in mudstones described here may be associated with conductive heat transfer as there is no evidence of fluid migration. Similar textures are described in the Karoo basin in a very similar geological setting by Aarnes et al.,

(2011b). Overpressure structures may have been caused by hydrothermal fluid migration instead of organic matter maturation as previously discussed.

Convection of fluids implies that fluids are not only responsible for heat transfer, but they are also the mass transfer main mechanism (Bjørlykke, 1994). The hydrothermal convective fluid migration occurs through the most permeable medias and leads in many instances to hydrothermal alteration (Bjørlykke, 1994; Ferry and Dipple, 1991; Middleton et al., 2001; Wilson et al., 2007). High pore-water flow rates associated with igneous intrusions caused bulk chemical composition change of the main pore-occluding mineral assemblage associated with hydrothermally induced diagenesis phase. The fluid migration media may be shear failures, thermal shock fractures/columnar jointing, reactivated faults and permeable sedimentary stratas (Barker et al., 1998; Genthon and Rabinowicz, 1990; Schmiedel et al., 2019; Summer and Ayalon, 1995). For instance, evidence of hydrothermal fluid migration through permeable strata (Fig. 6, 7), veins (Fig. 8) and failures along sedimentary strata forming breccias (Fig. 11 E-G) limited by mudstone layer baffles support that convective fluid migration were a the major heat transfer mechanism from igneous intrusion to interlayered reservoir rocks.

However, Bjørlykke et al. (1988) suggest that the convection cells require relatively thick (100-300m), homogeneous and porous sandstones to satisfy Rayleigh number conditions in numerical models. And even when this condition is fulfilled, pore-water convective flow could be so fast that there will not enough efficient to produce a diagenetic effect. Under this scenario, the presence of shales separating sandstone bodies forming interlayered sedimentary succession would decrease even more the mass transfer and hydrothermal fluid velocities. On the other hand, Genthon and Rabinowicz (1990) advocate that thermal convection related to hydrothermal cells can take place along anisotropic porous medium composed of porous sandstone layers and semi-porous shale or limestone layers if only a slight slope of the order of a few percent of the sedimentary layers occur. This condition may be satisfied by the formation of grabens and the tilting/folding of sedimentary layers associated

with shear failures and is easily identified in seismic data (De Castro et al., 2016; Schmiedel et al., 2019, 2017).

Hydrothermally mineralized stratas occurred in alternated levels but are more frequent towards igneous intrusions. The occurrence of alternated low- and high-temperature chlorites and low to highly mineralized stratas may have been controlled by sedimentary texture, stratigraphic surfaces as maximum flooding surfaces and interconnectivity of fault-sedimentary strata that may have favoured or halted hydrothermal fluid migration. The occurrence of pervasive authigenic mineralization within specific levels, high temperature chlorite associated with chalcopyrite occurrences along sedimentary succession and mineralized veins suggest that the proposed model is in agreement with previous models proposed in the literature (Duddy et al., 1994; Genthon and Rabinowicz, 1990; Girard et al., 1989; Holford et al., 2013; Reeckmann and Mebberson, 1984). Duddy et al. (1994) suggest that heated fluid migrating through confined intervals may generate complex vertical variation in the geothermal gradient.

Chlorite temperature formation may have also formed due to local and regional thermal regimes associated with different magmatic events as it is proposed for low and high temperatures measure in apatite fission tracks (Cardoso Jr. et al., 2020). However, the lower temperatures (<150°C) of the samples immediately above the igneous intrusion may be related to the fact that the chlorite were formed during the cooling of the igneous intrusion as it may have caused pore-water boiling (T~500°C) that have halted the precipitation of hydrous minerals (Rodrigues, 1995). Considering that chlorite temperature of formation is only the minimum value of temperature, sediments near igneous intrusion may have experienced temperature much higher than average values between 121 and 181°C recorded in chlorite geothermometer from samples collected 5 cm and 30cm above igneous-sedimentary contact.

The hydrothermally induced mineralization may have implications for ore-forming processes and hydrocarbon systems. For both, the slight slope occurrence is important to increase the lateral continuity of the mineralized layers (Fig. 18A). In the case of ore deposits, Pb-Zn-Cu sulfide mineralization would be favoured by the occurrence of major faults, rapid

cooling conditions, and primary content of base metals and reactivity of the sedimentary host rock (Deloule and Turcotte, 1989; Leach et al., 2010). Implications to the petroleum system is discussed in the following section.

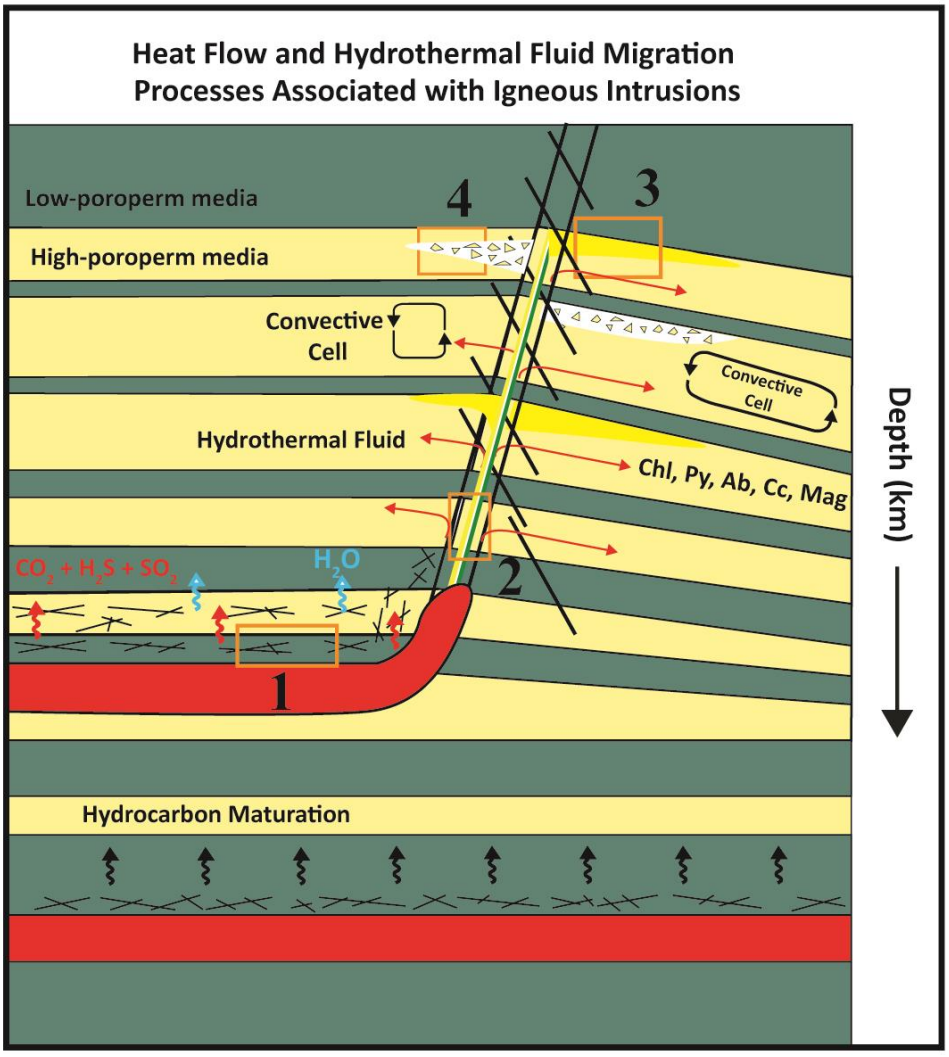

Figure 18. A) Schematic geological profile with the main heat flow and hydrothermal fluid migration processes on reservoir rocks associated with igneous intrusions highlighting the extension of convective cells, the dehydration of host rocks and the degassing of igneous intrusion. The orange rectangles correspond to hydrofracturing (1) (Fig. 9 A-I); mineralized veins with quartz, chlorite, calcite and sulphides (2) (Fig. 8 A-E); hydrothermal fluid migration associated with sulphides, chlorite, albite, calcite and magnetite mineralization along high poroperm stratas (3) (Fig. 7; Fig. 8 F-H; Fig. 10); carbonate cemented breccias horizons along sedimentary strata (4) (Fig. 11 E-H).

Thermal aureole thickness is a common measure to evaluate conduction and convective heat transfer mechanism from igneous rocks to host rocks. It is usually measured in percentage

of the associated igneous intrusion thickness (Aarnes et al., 2010; Barker et al., 1998; Raymond and Murchison, 1988). However, due to the sampling limitation of the igneous intrusion, it not possible to determine its thickness. However, the occurrence of hydrothermally induced diagenetic products up to 200m above igneous-sedimentary contact suggest a thermal aureole of at least 200m. In addition, the thermal aureole could be greater, however telodiagenesis overprinted hydrothermally induced diagenesis evidences. Duddy et al. (1994) suggest that convective heat and mass transfer generate complex vertical variation in the geothermal gradient and may cause thermal anomalies at distances of up to 10's of kilometres (Duddy et al., 1994; Genthon and Rabinowicz, 1990; Parnell, 2010). In summary, conductive heat transfer settings are harder to determine a thermal aureole based on associated igneous intrusion because it generates irregular and complex thermal anomalies regardless of the geothermometry method used.

2.4.6. Petroleum system implications

The reservoir zones division proposed (Fig. 16) shows a great correspondence with the reservoir qualities and divisions proposed by Miranda et al. (2018) for the same stratigraphic interval. The Zone 4 presents a good correlation with the Longá Formation reservoir rocks with an average porosity lower than 10% and average permeability lower than 10mD. In addition, above the two thickest intrusions there is an increase in permeability that is probably related to the presence of hydraulic fractures and contact metamorphism boiling reactions that have caused the expulsion of pore-water away. Therefore, authigenic mineralization immediately above igneous intrusions may have occured during the cooling and waning of hydrothermal activity. Natural fractures are critical for good flow rates in low-quality hornfels aureole facies (Miranda et al., 2018). Considering that the studied rocks are located in the eastern border of the basin and the wells studied by Miranda et al. (2018) are in depocenter of the basin, they are probably from different Longá facies and it is hard to say if the authigenic mineralization have decreased the reservoir quality of the Longá Formation rocks. However, the fact that

authigenic mineralization compose most of the pore-occluding mineral assemblage suggest that hydrothermal induced diagenesis have caused a decrease in reservoir quality.

Zone 3 is associated with the poorer reservoir quality, and most heterogeneous and laminated reservoir zone of the Poti Formation and present strong hydrothermally induced authigenic mineralization.

The presence of frequent hydraulic fractures may be responsible for permeability peaks and the presence of horizontal veins and breccias cemented by calcite may have increased the heterogeneity of this reservoir zone. Zone 2 presents a sharp decrease in hydraulic fractures frequency and permeabilities peaks are associated with thicker sandstone layers. Zone 2 would be equivalent to the middle reservoir zone (Miranda et al., 2018). Zone 1 comprises the upper reservoir zone of the Poti Formation and the lower part of the reservoir zone of the Piauí Formation. It is the best reservoir zone with the most homogeneous and thicker sandstone layers. The uppermost portion of the Poti and Piauí formations present an increase in porosity and permeability that is probably related to telodiagenesis processes as proposed by Bjørlykke and Jahren (2012) and G. Shanmugam (2002).

The strong relationship between stratigraphic sequences and changes in reservoir quality indexes suggest that they play an important role during the three diagenetic process (Morad et al., 2000) as they were not obliterated by authigenic mineralization associated with the igneous events and telodiagenetic processes.

Regarding the implications to the petroleum systems, the presence of overpressure structures, evidences of geochemically open systems (i.e. hydrothermal fluid migration through convective cells) and the high temperature conditions may have different consequences to the petroleum systems depending on whether secondary migration to reservoir rocks have occurred before or after the hydrothermal fluid migration triggered by igneous intrusions.

The first scenario consider that a hydrocarbon accumulation was present in reservoir rocks by the time igneous rocks have intruded, so secondary migration from source to reservoir

rock had occurred before hydrothermal fluid migration triggered by igneous intrusion events. The mass transfer of hydrothermal fluids generating overpressure structures (i.e. transgressive fractures and beef-like structures), fractures and veins; input of CO2, H2S and heat input from igneous rocks; and heated-pore water migration may cause the dismigration and/or cracking of prior accumulated hydrocarbons, reservoir compartmentalization and breaching of prior sealing layers. The reservoir rocks presented temperatures higher than 120°C at distances up to 190m above the igneous intrusion, which is close to the oil window upper limit 70-150°C (Bjørlykke, 2015; Surdam et al., 1989). The occurrence of temperatures higher than 200°C in alternated intervals along the Zones 4, 3 and 2 suggest that besides they present a good reservoir quality for gas production, they have reached temperatures that are not favourable for gas reservoir rocks.

In a second scenario where hydrocarbon migration to reservoir rocks have occurred after igneous intrusions. The hydrothermally induced diagenetic effects had occurred by the time secondary hydrocarbon migration happened. Therefore, the main pore spaces were filled by hydrothermally induced diagenetic minerals, it may cause a reservoir quality decrease, source-reservoir compartmentalization, reservoir compartmentalization and have implications to the stimulation processes chosen to improve reservoir rocks production. Healed fractures, veins, brittle structures may increase reservoir permeability if adequate reservoir chemical and physical stimulation is performed. In any case, although there was a decrease in reservoir quality, petrophysical data suggest the studied reservoir rocks present enough permeability and porosity to produce gas at commercial rates based on the associated producing fields reported by Miranda et al. (2018) and Tiab and Donaldson (2015). More complex scenarios in which hydrothermal fluid and hydrocarbon fluid migration are coeval are also possible, but it would be too speculative to discuss about it as the interaction of both fluids and chronological studies about fluid migration is scarce.

All implications to petroleum systems mentioned above depends on scale and lateral continuity of the authigenic mineralization and the range of distance that hydrothermal fluids can reach. Great convective cells occurrence is favoured by high permeability medias as deep structures, permeable layers, especially if sedimentary layers are slightly tilted. Therefore, graben and half-graben structures and regions with deep structures may favour the influence of authigenic mineralization in reservoir rocks triggered by igneous intrusions.

Generally, pyrite cementation is sparse on the Poti Formation when there is no direct evidence of thermal influence of igneous intrusion (de Araújo, 2018; Góes, 1995). However, in some of the gas fields in the Parnaíba Formation, pyrite occurs as pervasive pore-occluding mineral along millimetric intervals in reservoir rocks (Silveira et al., 2018). Resistivity and density logs are affected by its presence that consequently affect water saturation calculated by the Archie's equation. Overestimation of water saturation resulted in pessimist evaluation of gas reserves (Silveira et al., 2018). The form of occurrence of hydrothermal pyrites presented in this study and those described in gas fields are very similar. Stable isotopes show a major contribution of magmatic sulfur isotopes to form pyrite crystals as veins and cements in reservoir rocks of the Longá and Poti Formation. Therefore, petrology and stable isotopes data suggest that hydrothermal fluid migration control bulk mineral composition of the main pore-occluding minerals and have significant implications to hydrocarbons exploration and production.

2.5 Conclusions

Reservoir rocks of petroleum systems with igneous intrusions may have a complex diagenetic history with an important authigenic mineralization phase associated with heat flow and hydrothermally induced diagenesis. The presence of igneous intrusions may not be directly observed in outcrops, wells or through seismic data (Girard et al., 1989; Holford et al.,

2013) but its effects on reservoir rocks may be identifiable via isotopic geochemistry, petrology and geothermometric data as showed in this study and supported by Ahmed (2002); Cardoso Jr. et al. (2020); Girard et al. (1989); Haile et al. (2018, 2019)studies.

The mineral assemblage of pyrite, chlorite, albite, illite, ± iron oxides, chalcopyrite, biotite filling most of the pore spaces of sandstones is very different from the mineral assemblage and diagenetic products described in the literature for progressive burial diagenesis in the Parnaíba basin (de Araújo, 2018; Góes, 1995). Heat and mass transfer input of iron and magnesium from igneous intrusions were responsible for the great bulk mineral compositional change in reservoir rocks. The presence of a high-temperature and bulk chemical mineral compositional change may be used as an indicative of hydrothermal fluid migration record in other basins with similar geological settings. Detrital minerals and eo- mesodiagenetic were partially or totally corroded, dissolved, or transformed into other minerals in the hydrothermally induced diagenetic phase. Chlorite temperature of formation indicated that reservoir rocks affect by hydrothermal fluids have reached temperatures much higher than what were expected associated with progressive burial. The results of the four empirical geothermometric methods used presented a great agreement with zircon apatite fission track temperature values in a nearby study in the Parnaíba basin (Cardoso Jr. et al., 2020) and support the fact that the studied succession were thermally affected by igneous intrusions. The combination methods with similar Fe/Fe+Mg ratios and geological settings proved to be a very useful tool for minimum values of the highest temperature reached by authigenic chlorite-bearing sediments affected by hydrothermal induced diagenesis.

The highest values of chlorite formation and the occurrence of pervasive cemented sandstone layers in alternated levels with no direct relationship with the distance to igneous intrusion indicate that hydrothermal fluids may have migrated preferentially through highly porous and permeable medias. Sandstone layers and vertical faults may have worked as conduits of hydrothermal fluids that were limited by adjacent flow baffles. Petrophysical data showed that although there is a decrease in reservoir quality towards igneous intrusions,

hydrothermally induced mineralization has not overprinted stratigraphic surfaces and depositional environment control on poroperm variations along the sedimentary succession.

In addition, to the bulk change in the mineral assemblage and geothermometric data, the use of stable isotopes data has also proved to be a useful tool to identify the hydrothermal influence of igneous intrusion in sedimentary host rocks. Comparing the sulfur isotopic signature igneous intrusions hosted pyrites with sedimentary hosted pyrites, it is suggested that the igneous intrusions were the major sulfur isotopic source (i.e. igneous fingerprint) to form pyrite veins and cements in the sedimentary succession. More isotopic studies are required to better evaluate contribution of other isotopic sources. Igneous intrusions were also the main isotopic source of carbon to form calcite veins and breccias hosted in sedimentary rocks in distances of up to 100m from igneous intrusions. A minor contribution from dissolution of previously formed carbonate cement and bioclasts from the Lower Poti Formation may also occur. However, volumetric contribution and isotopic studies of these two possible isotopic sources must be further investigated.

Regarding the implications to the petroleum systems, the presence of overpressure structures, evidences of geochemically open systems (i.e. hydrothermal fluid migration through convective cells) and the high temperature conditions may have different consequences to the petroleum systems depending on whether secondary migration to reservoir rocks have occurred before or after the hydrothermal fluid migration triggered by igneous intrusions.

The first scenario consider that a hydrocarbon accumulation was present in reservoir rocks by the time igneous rocks have intruded, so secondary migration from source to reservoir rock had occurred before hydrothermal fluid migration triggered by igneous intrusion events. The mass transfer of hydrothermal fluids generating overpressure structures (i.e. transgressive fractures and beef-like structures), fractures and veins; input of CO_2, H_2S and temperature from igneous rocks; and heated-pore water migration may cause the dismigration and/or cracking of prior accumulated hydrocarbons, reservoir compartmentalization and breaching of prior sealing layers.

On the other hand, in a second scenario where hydrocarbon migration to reservoir rocks have occurred after igneous intrusions consider that the hydrothermally induced diagenetic effects had occurred by the time secondary hydrocarbon migration happened. Therefore, as the main pore spaces are filled by hydrothermally induced diagenetic minerals, it may cause a reservoir quality decrease, source-reservoir compartmentalization, reservoir compartmentalization and have implications to the stimulation processes chosen to improve reservoir rocks production. Healed fractures, veins, brittle structures may increase reservoir permeability if adequate reservoir chemical and physical stimulation is performed. More complex scenarios in which hydrothermal fluid and hydrocarbon fluid migration are coeval are also possible, but it would be too speculative to discuss about it as there the interaction of both fluids and chronological studies about fluid migration is scarce.

In any case, although there was a decrease in reservoir quality, petrophysical data suggest the studied reservoir rocks present enough permeability and porosity to produce gas at commercial rates based on the associated producing fields reported by Miranda et al. (2018).

All implications to petroleum systems mentioned above depends on scale and lateral continuity of the authigenic mineralization and the range of distance that hydrothermal fluids can reach. Great convective cells occurrence is favoured by high permeability medias as deep structures, permeable layers, especially if sedimentary layers are slightly tilted. Therefore, graben and half-graben structures and regions with deep structures may favour the influence of authigenic mineralization in reservoir rocks triggered by igneous intrusions.

2.6 Acknowledgments

This paper is part of the master's thesis of HAL. This study was financed in part by the Coordenação de Aperfeiçoamento de Pessoal de Nível Superior – Brasil (CAPES) -Finance Code 001 and by ENEVA SA.. We thank Elton L. Dantas for the acquisition of isotopic analyses, Luiz F. Tabosa and Eduardo Rolim for the acquisition of petrophysical analyses and

Paola F. Barbosa for the acquisitions of QEMScan analysis at the University of Brasília. HAL acknowledges Finatec, Eneva and ANP for scholarship.

2.7 References

Aagaard, P., Egeberg, Z.P.K., Saigal, G.C., Morad, S., Bjorlykkez, K., 1990. Diagenetic albitization of detrital K-Feldsars in Jurassic, Lower Cretaceous and Tertiary clastic reservoir rocks from offshore Norway, II. Formation water chemistry and kinetic considerations. J. Sediment. Petrol. 60, 575–581.

Aarnes, I., 2010. Sill emplacement and contact metamorphism in sedimentary basins Local processes with global implications. University of Oslo.

Aarnes, I., Fristad, K., Planke, S., Svensen, H., 2011a. The impact of host-rock composition on devolatilization of sedimentary rocks during contact metamorphism around mafic sheet intrusions. Geochemistry, Geophys. Geosystems 12. https://doi.org/10.1029/2011GC003636

Aarnes, I., Podladchikov, Y., Svensen, H., 2012. Devolatilization-induced pressure build-up: Implications for reaction front movement and breccia pipe formation. Geofluids 12, 265–279. https://doi.org/10.1111/j.1468-8123.2012.00368.x

Aarnes, I., Svensen, H., Connolly, J.A.D., Podladchikov, Y.Y., 2010. How contact metamorphism can trigger global climate changes: Modeling gas generation around igneous sills in sedimentary basins. Geochim. Cosmochim. Acta 74, 7179–7195. https://doi.org/10.1016/j.gca.2010.09.011

Aarnes, I., Svensen, H., Polteau, S., Planke, S., 2011b. Contact metamorphic devolatilization of shales in the Karoo Basin, South Africa, and the effects of multiple sill intrusions. Chem. Geol. 281, 181–194. https://doi.org/10.1016/j.chemgeo.2010.12.007

Abelha, M., Petersohn, E., Bastos, G., 2018. New insights into the Parnaíba Basin : results of investments by the Brazilian National Petroleum Agency. Geol. Soc. London 472, 361–366.

Ahmed, W., 2002. Effects of heat-flow and hydrothermal fluids from volcanic intrusions on authigenic mineralization in sandstone formations. Bull. Chem. Soc. Ethiop. 16, 37–52. https://doi.org/10.4314/bcse.v16i1.20947

Amaefule, J.O., Altunbay, M., Laboratories, C., Tiab, D., Oklahoma, U., Kersey, D.G., Keelan, D.K., Laboratories, C., 1993. Enhanced Reservoir Description: Using Core and Log Data to Identify Hydraulic (Flow) Units and Predict Permeability in Uncored Intervals/Wells, in: Society of Petroleum Engineers. 68th Annual Technical Conference and Exhibition of the Society of Petroleum Engineers, Houston, Texas, pp. 205–220.

Araújo, D.B., 2017. Bacia do Parnaíba, Sumário Geológico e Setores em Oferta. 14ª Rodada Licitações de Petróleo e Gás.

Baksi, A.K., Archibald, D.A., 1997. Mesozoic igneous activity in the Maranhão province, northern Brazil: 40Ar/39Ar evidence for separate episodes of basaltic magmatism. Earth Planet. Sci. Lett. 151, 139–153. https://doi.org/10.1016/s0012-821x(97)81844-4

Barker, C.E., Bone, Y., Lewan, M.D., 1998. Fluid inclusion and vitrinite-reflectance geothermometry compared to heat-flow models of maximum paleotemperature next to dikes, western onshore Gippsland Basin, Australia. Int. J. Coal Geol. 37, 73–111. https://doi.org/10.1016/S0166-5162(98)00018-4

Bjørlykke, K., 2015. Petroleum geoscience: From Sedimentary Environments to Rock Physics, Second. ed. Springer. https://doi.org/10.5860/choice.41-4685

Bjørlykke, K., 1994. Fluid-flow processes and diagenesis in sedimentary basins. Geofluids Orig. Migr. Evol. Fluids Sediment. Basins 78, 127–140.

Bjørlykke, K., 1993. Fluid flow in sedimentary basins. Sediment. Geol. 86, 137–158.

Bjørlykke, K., Jahren, J., 2012. Open or closed geochemical systems during diagenesis in sedimentary basins : Constraints on mass transfer during diagenesis and the prediction of porosity in sandstone and carbonate reservoirs. AA 96, 2193–2214. https://doi.org/10.1306/04301211139

Bjørlykke, K., Mo, A., Palm, E., 1988. Diagenesis I, in: Chilingarian, G.V., Wolf, K.H. (Eds.), Developments in Sedimentology. pp. 555–588.

https://doi.org/https://doi.org/10.1016/S0070-4571(08)70180-8
Bourdelle, F., Parra, T., Chopin, C., Beyssac, O., 2013. A new chlorite geothermometer for diagenetic to low-grade metamorphic conditions. Contrib. to Mineral. Petrol. 165, 723–735. https://doi.org/10.1007/s00410-012-0832-7
Bourdelle, F.R., Cathelineau, M.I., 2015. Low-temperature chlorite geothermometry : a graphical representation based on a T – R 2 þ – Si diagram 617–626. https://doi.org/10.1127/ejm/2015/0027-2467
Brauckmann, F.J., Fuchtbauer, H., 1983. Alterations of Cretaceous siltstones and sandstones near basalt contacts of basaltic intrusions (Nfigssuaq, Greenland). Sediment. Geol. 35, 193–213.
Bruckschen, P., Oesmann, S., Veizer, J., 1999. Isotope stratigraphy of the European Carboniferous: Proxy signals for ocean chemistry, climate and tectonics. Chem. Geol. 161, 127–163. https://doi.org/10.1016/S0009-2541(99)00084-4
Bufe, N.A., Holness, M.B., Humphreys, M.C.S., 2014. Contact metamorphism of Precambrian gneiss by the Skaergaard intrusion. J. Petrol. 55, 1595–1617. https://doi.org/10.1093/petrology/egu035
Cardoso, A.R., Nogueira, A.C.R., Abrantes, F.R., Rabelo, C.E.N., 2017. Mesozoic lacustrine system in the Parnaíba Basin, northeastern Brazil: Paleogeographic implications for west Gondwana. J. South Am. Earth Sci. 74, 41–53. https://doi.org/10.1016/j.jsames.2017.01.006
Cardoso Jr., M., Chemale Jr., F., de Oliveira, C.H.E., de Souza Cruz, C.E., de Abreu, C.J., Genezini, F.A., 2020. Thermal history of potential gas reservoir rocks in the eastern Parnaíba Basin, Brazil. Am. Assoc. Pet. Geol. Bull. 104, 305–328. https://doi.org/10.1306/05021918117
Cathelineau, M., 1988. Cation site occupancy in chlorites and illistes as a function of temperature. Clay Miner. 23, 471–485.
Cathelineau, M., Nieva, D., 1985. A chlorite solid solution geothermometer The Los Azufres (Mexico) geothermal system. Contrib. to Mineral. Petrol. 91, 235–244.
Chen, Z., Yan, H., Li, J., Zhang, G., Zhang, Z., Liu, B., 1999. Relationship between Tertiary volcanic rocks and hydrocarbons in the Liaohe basin, People's Republic of China. Am. Assoc. Pet. Geol. Bull. 83, 1004–1014. https://doi.org/10.1306/E4FD2E51-1732-11D7-8645000102C1865D
Chivas, A.R., Andrew, A.S., Sinha, A.K., O'Neil, J.R., 1982. Geochemistry of a Pliocene-Pleistocene oceanic-arc plutonic complex, Guadalcanal. Nature 300, 139–143. https://doi.org/10.1038/300139a0
Claypool, G.E., Holser, W.T., Kaplan, I.R., Sakai, H., Zak, I., 1980. The age curves of sulfur and oxygen isotopes in marine sulfate and their mutual interpretation. Chem. Geol. 28, 199–260. https://doi.org/10.1016/0009-2541(80)90047-9
Cobbold, P.R., Rodrigues, N., 2007. Seepage forces, important factors in the formation of horizontal hydraulic fractures and bedding-parallel fibrous veins ("beef" and 'cone-in-cone'). Geofluids 7, 313–322. https://doi.org/10.1111/j.1468-8123.2007.00183.x
Cobbold, P.R., Zanella, A., Rodrigues, N., Løseth, H., 2013. Bedding-parallel fibrous veins (beef and cone-in-cone): Worldwide occurrence and possible significance in terms of fluid overpressure, hydrocarbon generation and mineralization. Mar. Pet. Geol. 43, 1–20. https://doi.org/10.1016/j.marpetgeo.2013.01.010
CPRM, 2015. Informe de Recursos Minerais Programa Geologia do Brasil; Série Pedras Preciosas, n 08; Projeto Avaliação dos Depósitos de Opalas de Pedro II.
Craig, H., 1957. Isotopic standards for carbon and oxygen and correction factors for mass-spectrometric analysis of carbon dioxide. Geochim. Cosmochim. Acta 12, 133–149.
de Araújo, V.B.V., 2018. Sedimentação, Estratigrafia e Diagênese dos Reservatório da Formação Poti, Viseano, Bacia do Parnaíba. Universidade de Brasília.
De Castro, D.L., Bezerra, F.H., Fuck, R.A., Vidotti, R.M., 2016. Geophysical evidence of pre-sag rifting and post-rifting fault reactivation in the Parnaiba basin, Brazil. Solid Earth 7, 529–548. https://doi.org/10.5194/se-7-529-2016

Deloule, E., Turcotte, D.L., 1989. The Flow of Hot Brines in Cracks and the Formation of Ore Deposits 84, 2217–2225.

Dias, A.N.C., Moura, C.A. V, Neto, J.M.M., Chemale, F., Girelli, T.J., Masuyama, K.M., 2017. Geochronology and thermochronology of the gneisses of the Brasiliano/Pan-African Araguaia Belt: Records of exhumation of West Gondwana and Pangea break up. J. South Am. Earth Sci. https://doi.org/10.1016/j.jsames.2017.09.027

Duddy, I.R., Green, P.F., Hegarty, K.A., Bray, R.J., 1994. Recognition of the thermal effects of fluid flow in sedimentary basins. Geofluids Orig. Migr. Evol. Fluids Sediment. Basins 325–345.

Dutrow, B.L., Travis, B.J., Gable, C.W., Henry, D.J., 2001. Coupled heat and silica transport associated with dike intrusion into sedimentary rock: Effects on isotherm location andpermeability evolution. Geochim. Cosmochim. Acta 65, 3749–3767. https://doi.org/10.1016/S0016-7037(01)00704-9

Eide, C.H., Schofield, N., Jerram, D.A., Howell, J.A., 2017. Basin-scale architecture of deeply emplaced sill complexes: Jameson Land, East Greenland. J. Geol. Soc. London. 174, 23–40. https://doi.org/10.1144/jgs2016-018

Einsele, G., 1982. Mechanism of sill intrusion into soft sediment and expulsion of pore water. Initial Reports Deep Sea Drill. Proj. 64 1169–1176.

Einsele, G., Gieskes, J.M., Curray, J., Moore, D.M., Aguayo, E., Aubry, M.-P., Fornari, D., Guerrero, J., Kastner, M., Kelts, K., Lyle, M., Matoba, Y., Molina-Cruz, A., NIemitz, J., Rueda, J., Saunders, A., Schrader, H., Simoneit, B., Vacquier, V., 1980. Intrusion of Basaltic Sills into Highly Porous Sediments, and resulting hydrothermal activity. Nature 283, 441–445.

Eiras, J.F., Ribeiro, J., Filho, W., 2003. Sistemas Petrolíferos Ígneo-Sedimentares. pp. 1–6.

Fallick, A.E., Ashton, J.H., Boyce, A.J., Ellam, R.M., Russell, M.J., 2001. Bacteria were responsible for the magnitude of the world-class hydrothermal base metal sulfide orebody at Navan, Ireland. Econ. Geol. 96, 885–890. https://doi.org/10.2113/gsecongeo.96.4.885

Farooqui, M.Y., Hou, H., Li, G., Machin, N., Neville, T., Pal, A., Shricastva, C., Wang, Y., Yang, F., Yin, C., Zhao, J., Yang, X., 2009. Evaluating Volcanic Reservoirs. Oilf. Rev. Spring 21, 36–47.

Ferry, J.M., Dipple, G.M., 1991. Fluid flow , mineral reactions, and metasomatism. Geology 19, 211–214.

Fodor, R. V., Sial, A.N., Mukasa, S.B., McKee, E.H., 1990. Petrology, isotope characteristics, and K-Ar ages of the Maranh??o, northern Brazil, Mesozoic basalt province. Contrib. to Mineral. Petrol. 104, 555–567. https://doi.org/10.1007/BF00306664

Folk, R.L., 1980. Petrology of Sedimentary Rocks. Hemphill Publishing Co., Austin, Texas.

G. Shanmugam, 2002. Porosity Prediction in Sandstones Using Erosional Unconformities: ABSTRACT. Am. Assoc. Pet. Geol. Bull. 73. https://doi.org/10.1306/44b49e16-170a-11d7-8645000102c1865d

Garcia, A.J.., Morad, S., De Ros, L.F., Al-Aasm, I.S., 1998. Palaeogeographical, paleoclimatic and burial history controls on the diagenetic evolution of resevoir sandstones: evidence from the Lower Cretaceous Serraria sandstones in the Sergipe-Alagoas Basin, NE Brazil, in: Morad, Sadoon (Ed.), Carbonate Cementation in Sandstones. Special Publications International Association of Sedimentologists, Sedimentology. pp. 107–140.

Genthon, P., Rabinowicz, M., 1990. Sedimentary Basin : Application to the Okinawa Back Arc Basin KF23. J. Geophys. Res. 95, 175–184.

Gierlowski-Kordesch, E.H., Weismiller, H.C., Stigall, A.L., Hembree, D.I., 2015. Pedogenic mud aggregates and sedimentation patterns between basalt flows (Jurassic Kalkrand Formation, Namibia) 2515, 65–86. https://doi.org/10.1130/2015.2515(04)

Giggenbach, W.F., 2003. Magma Degassing and Mineral Deposition in Hydrothermal Systems along Convergen Plate Boundaries. Econ. Geol. 87, 1927–1944.

Giggenbach, W.F., 1988. Geothermal solute equilibria. Derivation of Na-K-Mg-Ca geoindicators. Geochim. Cosmochim. Acta 52, 2749–2765.

Giles, M.R., Indrelid, S.L., Beynon, G. V., Amthor, J., 2000. The origin of large-scale quartz

cementation: evidence from large data sets and coupled heat–fluid mass transport modelling, in: Worden, R.H., Morad, S. (Eds.), Quartz Cementation in Sandstones. Blackwell Publishing Ltd., pp. 21–28. https://doi.org/10.1002/9781444304237

Gilg, H.A., Morteani, G., Kostitsyn, Y., Preinfalk, C., Gatter, I., Strieder, A.J., 2003. Genesis of amethyst geodes in basaltic rocks of the Serra Geral Formation (Ametista do Sul, Rio Grande do Sul, Brazil): A fluid inclusion, REE, oxygen, carbon, and Sr isotope study on basalt, quartz, and calcite. Miner. Depos. 38, 1009–1025. https://doi.org/10.1007/s00126-002-0310-7

Girard, J.P., Deynoux, M., Nahon, D., 1989. Diagenesis of the Upper Proterozoic siliciclastic sediments of the Taoudeni basin (West Africa) and relation to diabase emplacement. J. Sediment. Petrol. 59, 233–248. https://doi.org/10.1306/212F8F58-2B24-11D7-8648000102C1865D

Góes, A.M., 1995. A Formação Poti (Carbonífero Inferior) da Bacia do Parnaíba. Universidade de São Paulo. https://doi.org/10.11606/T.44.1995.tde-11022014-105309

Goés, Á.M.O., Feijó, F.J., 1994. Feijó, 1994.pdf.

González-Acebrón, L., Goldstein, R.H., Mas, R., Arribas, J., 2011. Criteria for Recognition of Localization and Timing of Multiple Events of Hydrothermal Alteration in Sandstones Illustrated by Petrographic , Fluid inclusion , and Isotopic Analysis of the Tera Group , Northern Spain. Int. J. Earth Sci. 100, 1811–1826. https://doi.org/10.1007/s00531-010-0606-2

Goodfellow, W.D., Jonasson, I.R., 1984. Ocean stagnation and ventilation defined by δ34 S secular trends in pyrite and barite, Selwyn Basin, Yukon. Geology 12, 583–586. https://doi.org/10.1130/0091-7613(1984)12<583:OSAVDB>2.0.CO;2

Graham, U.M., Ohmoto, H., 1994. Experimental study of formation mechanisms of hydrothermal pyrite. Geochim. Cosmochim. Acta 58, 2187–2202. https://doi.org/10.1016/0016-7037(94)90004-3

Grapes, R., 2011. Pyrometamorphism, Second. ed. Springer, Seoul. https://doi.org/10.1007/978-3-642-15588-8

Grossman, E.L., 1994. Carboniferous to Triassic. Geol. Soc. Am. Bull. Special Pa.

Grossman, E.L., Chuanlun Zhang, Yancey, T.E., 1991. Stable-isotope stratigraphy of brachiopods from Pennsylvanian shales in Texas. Geol. Soc. Am. Bull. 103, 953–965. https://doi.org/10.1130/0016-7606(1991)103<0953:SISOBF>2.3.CO;2

Grossman, E.L., Horng-Sheng Mii, Yancey, T.E., 1993. Stable isotopes in late Pennsylvanian brachiopods from the United States: implications for Carboniferous paleoceanography. Geol. Soc. Am. Bull. 105, 1284–1296. https://doi.org/10.1130/0016-7606(1993)105<1284:SIILPB>2.3.CO;2

Grove, C., 2014. Direct and Indirect Effects of Flood Basalt Volcanism on Reservoir Quality Sandstone. Durham University.

Grove, C., Jerram, D.A., Gluyas, J.G., Brown, R.J., 2017. Sandstone Diagenesis in Sediment–lava Sequences: Exceptional Examples of Volcanically Driven Diagenetic Compartmentalization in Dune Valley, Huab Outliers, Nw Namibia. J. Sediment. Res. 87, 1314–1335. https://doi.org/10.2110/jsr.2017.75

Habicht, K.S., Canfield, D.E., 1997. Sulfur isotope fractionation during bacterial sulfate reduction in organic-rich sediments. Geochim. Cosmochim. Acta 61, 5351–5361. https://doi.org/10.1016/S0016-7037(97)00311-6

Haile, B.G., Czarniecka, U., Xi, K., Smyrak-sikora, A., Jahren, J., Braathen, A., Hellevang, H., 2019. Hydrothermally induced diagenesis : Evidence from shallow marine- deltaic sediments , Wilhelmøya , Svalbard. Geosci. Front. 10, 629–649. https://doi.org/10.1016/j.gsf.2018.02.015

Haile, B.G., Klausen, T.G., Jahren, J., Braathen, A., Hellevang, H., 2018. Thermal history of a Triassic sedimentary sequence verified by a multi-method approach: Edgeøya, Svalbard, Norway. Basin Res. 30, 1075–1097. https://doi.org/10.1111/bre.12292

Hangx, S.J.T., Spiers, C.J., 2009. Reaction of plagioclase feldspars with CO2 under hydrothermal conditions. Chem. Geol. 265, 88–98.

https://doi.org/10.1016/j.chemgeo.2008.12.005
Haszeldine, R.S., Samson, I.M., Cornford, C., 1984. Quartz Diagenesis and Convective Fluid Movement: Bearing Oilfield, UK North Sea. Clay Miner. 19, 391–402.
Hillier, R.D., Cosgrove, J.W., 2010. Core and seismic observations of overpressure-related deformation within Eocene sediments of the Outer Moray Firth, UKCS. Pet. Geosci. 8, 141–149. https://doi.org/10.1144/petgeo.8.2.141
Holford, S.P., Schofield, N., Jackson, C.A.L., Magee, C., Green, P.F., Duddy, I.R., 2013. Impacts of igneous intrusions on source and reservoir potential in prospective sedimentary basins along the western Australian continental margin. West Aust. Basins Symp. 2013 18–21.
Holford, S.P., Schofield, N., MacDonald, J.D., Duddy, I.R., Green, P.F., 2012. Seismic analysis of igneous systems in sedimentary basins and their impacts on hydrocarbon prospectivity: examples from the Southern Australian margin. APPEA J. 229, 229–252. https://doi.org/10.1071/AJ11017
Hollanda, M.H.B.M., Archanjo, C.J., Filho, A.A.M., Fossen, H., Ernst, R.E., Castro, D.L. De, Melo, A.C., Oliveira, A.L., 2019. The Mesozoic Equatorial Atlantic Magmatic Province (EQUAMP): A new Large Igneous Province in South America, in: Dyke Swarms of the World: A Modern Perspective, Springer Geology. Springer Singapore, pp. 87–110. https://doi.org/10.1007/978-981-13-1666-1
Holness, M.B., 2002. Spherulitic textures formed during crystallization of partially melted arkose, Rum, Scotland. Geol. Mag. 6, 651–663. https://doi.org/10.1017/S0016756802006842
Holness, M.B., 1999. Contact metamorphism and anatexis of Torridonian arkose by minor intrusions of the Rum Igneous Complex, Inner Hebrides, Scotland. Geol. Mag. 136, 527–542. https://doi.org/10.1017/s0016756899002988
Holness, M.B., Isherwood, C.E., 2003. The aureole of the Rum Tertiary Igneous Complex , Scotland. J. Geol. Soc. London 160, 15–27.
Holness, M.B., Watt, G.R., 2002. The Aureole of the Traigh Bhàn na Sgùrra Sill , Isle of Mull : Reaction-Driven Micro-cracking During Pyrometamorphism. J. Petrol. 43, 511–534.
Iyer, K., Schmid, D.W., Planke, S., Millett, J., 2017. Modelling hydrothermal venting in volcanic sedimentary basins: Impact on hydrocarbon maturation and paleoclimate. Earth Planet. Sci. Lett. 467, 30–42. https://doi.org/10.1016/j.epsl.2017.03.023
Jamtveit, B., 1992. Contact metamorphism of layered carbonate-shale sequences in the Oslo Rift . II : Migration of isotopic and reaction fronts around cooling plutons 114, 131–148.
Jamtveit, B., Svensen, H., Podladchikov, Y.Y., Planke, S., 2004. Hydrothermal Vent Complexes Associated with Sill Intrusions in Sedimentary Basins. Phys. Geol. High-Level Magmat. Syst. 234, 233–241.
Janasi, V. de A., de Freitas, V.A., Heaman, L.H., 2011. The onset of flood basalt volcanism, Northern Paraná Basin, Brazil: A precise U-Pb baddeleyite/zircon age for a Chapecó-type dacite. Earth Planet. Sci. Lett. 302, 147–153. https://doi.org/10.1016/j.epsl.2010.12.005
Javoy, M., Pineau, F., Delorme, H., 1986. Carbon and nitrogen isotopes in the mantle. Chem. Geol. 57, 41–62. https://doi.org/10.1016/0009-2541(86)90093-8
Kavalieris, I., Walshe, J.L., Halley, S., Harrold, B.P., 1990. Dome-Related Gold Mineralization in the Pani Volcanic Complex , North Sulawesi , Indonesia : A Study of Geologic Relations , Fluid Inclusions , and Chlorite Compositions 85, 1208–1225.
Kennedy, G.C., 1950. A portion of the system silica-water. Econ. Geol. 45, 629–653. https://doi.org/10.2113/gsecongeo.45.7.629
Kranidiotis, P., Maclean, W.H., 1987. Systematics of Chlorite Alteration at the Phelps Dodge Massive Sulfide Deposit , Matagami , Quebec 82, 1898–1911.
Leach, D.L., Bradley, D.C., Huston, D., Pisarevsky, S.A., Taylor, R.D., Gardoll, S.J., 2010. Sediment-Hosted Lead-Zinc Deposits in Earth History. Econ. Geol. 105, 593–625. https://doi.org/10.2113/gsecongeo.105.3.593
Liu, J., Wang, P., Zhang, Y., Bian, W., Huang, Y., 2013. Volcanic Rock-Hosted Natural Hydrocarbon Resources: A, in: Liu, Jiaqi (Ed.), Updates in Volcanology - New Advances

in Understanding Volcanic Systems. Intech Open Science Open Mind, pp. 20–23. https://doi.org/10.5772/54587

Magoon, L.B., Dow, W.G., 1994a. The petroleum system. Pet. Syst. - From Source to Trap AAPG Memoi, 3–24.

Magoon, L.B., Dow, W.G., 1994b. The petroleum system - from source to trap. Pet. Syst. - from source to trap. https://doi.org/10.1016/0920-4105(95)00059-3

Mandl, G., Harkness, R.M., 1987. Hydrocarbon migration by hydraulic fracturing. Geol. Soc. London, Spec. Publ. 29, 39–53. https://doi.org/10.1144/gsl.sp.1987.029.01.04

Marini, L., Moretti, R., Accornero, M., 2011. Sulfur Isotopes in Magmatic-Hydrothermal Systems, Melts, and Magmas. Rev. Mineral. Geochemistry 73, 423–492. https://doi.org/10.2138/rmg.2011.73.14

Matsui, E., Salati, E., Marini, O.J., 1974. D/H and 18 O/ 16 O ratios in waters contained in geodes from the basaltic province of Rio Grande do Sul, Brazil. Bull. Geol. Soc. Am. 85, 577–580. https://doi.org/10.1130/0016-7606(1974)85<577:DAORIW>2.0.CO;2

Mckinley, J.M., Worden, R.H., Ruffell, A.H., 2007. Contact Diagenesis: The Effect of an Intrusion on Reservoir Quality in the Triassic Sherwood Sandstone Group, Northern Ireland. J. Sediment. Res. 71, 484–495. https://doi.org/10.1306/2dc40957-0e47-11d7-8643000102c1865d

Michelon, D., Miranda, F.S., Pereira, E., Aragão, F., Planke, S., 2019. Distribution and volume of Mesozoic intrusive rocks in the Parnaíba Basin constrained by well data, in: LASI VI Conference -The Physical Geology of Subvolcanic Systems - Laccoliths, Sills and Dykes. Malargue, Argentina, pp. 89–90.

Middleton, D.W.J., Parnell, J., Green, P.F., Xu, G., McSherry, M., 2001. Hot Fluid Events in Atlantic Margin Basins: an Example from the Rathlin Basin. Geol. Soc. London, Spec. Publ. 188, 91–105.

Mii, H., Yancey, T.E., 1999. Carboniferous isotope stratigraphies of North America: implications for Carboniferous paleoceanography and Mississippian glaciation. Geological Society of America Bulletin 111 (7), 960–973. Geol. Soc. Am. Bull. 111, 960–973.

Miranda, F.S.. D., 2014. Caracterização geológica da Formação Pimenteiras como potencial reservatório do tipo shale-gas , Devoniano da Bacia do Parnaíba , Brasil. UFRJ.

Miranda, F.S.D.E., Vettorazzi, A.L., Cunha, R.D.A.C., Aragão, F.B., Michelon, D., Caldeira, J.L., Porsche, E., Martins, C., Ribeiro, R.B., Vilela, A.F., Corrêa, J.R., Silveira, L.S., Andreola, K., 2018. Atypical igneous-sedimentary petroleum systems of the Parnaíba Basin , Brazil : seismic , well logs and cores. Geol. Soc. London 472, 341–360. https://doi.org/10.1144/SP472.15

Mitsuhata, Y., Matsuo, K., Minegishi, M., 1999. Magnetotelluric survey for exploration of a volcanic-rock reservoir in the Yurihara oil and gas field, Japan. Geophys. Prospect. 47, 195–218. https://doi.org/10.1046/j.1365-2478.1999.00127.x

Morad, S., 1990. Albitization of Detrital Plagioclase in Triassic Reservoir Sandstones from the Snorre field, Norwegian North Sea. J. Sediment. Petrol. 60, 411–425.

Morad, S., Al-ramadan, K., Ketzer, J.M., De Ros, L.F., 2010. The impact of diagenesis on the heterogeneity of sandstone reservoirs : A review of the role of depositional facies and sequence stratigraphy. Am. Assoc. Pet. Geol. Bull. 94, 1267–1309. https://doi.org/10.1306/04211009178

Morad, S., Ketzer, J.M., De Ros, L.R., 2000. Spatial and temporal distribution of diagenetic alterations in siliciclastic rocks: Implications for mass transfer in sedimentary basins. Sedimentology 47, 95–120. https://doi.org/10.1046/j.1365-3091.2000.00007.x

Needham, S.J., Worden, R.H., McIlroy, D., 2006. Experimental Production of Clay Rims by Macrobiotic Sediment Ingestion and Excretion Processes. J. Sediment. Res. 75, 1028–1037. https://doi.org/10.2110/jsr.2005.078

Oliveira, A.L., Pimentel, M.M., Fuck, R.A., Oliveira, D.C., Geociências, I. De, Brasília, U. De, Universitário, C., Ribeiro, D., Cep, I.C., Petrobras, E., Geint, P.G., Rocha, A.E., 2018. Petrology of Jurassic and Cretaceous basaltic formations from the Parnaíba Basin , NE

Brazil : correlations and associations with large igneous provinces.
Parnell, J., 2010. Potential of palaeofluid analysis for understanding oil charge history. Geofluids 10, 73–82. https://doi.org/10.1111/j.1468-8123.2009.00268.x
Peter, J.M., Shanks, W.C., 2003. Sulfur, carbon, and oxygen isotope variations in submarine hydrothermal deposits of Guaymas Basin, Gulf of California, USA. Geochim. Cosmochim. Acta 56, 2025–2040. https://doi.org/10.1016/0016-7037(92)90404-7
Pettijohn, F.J., Potter, P.E., Siever, R., 1973. Sand and Sandstone, 1st ed. Springer-Verlag, Berlin. https://doi.org/10.1007/978-1-4615-9974-6
Philipp, S.L., Afşar, F., Gudmundsson, A., 2013. Effects of mechanical layering on hydrofracture emplacement and fluid transport in reservoirs. Front. Earth Sci. 1, 1–19. https://doi.org/10.3389/feart.2013.00004
Polyansky, O.P., Reverdatto, V. V., 2007. Contact metamorphism and metasomatism near the Talnakh intrusion: Fluid convection and heat transfer modeling on the basis of the finite-difference method. Dokl. Earth Sci. 411, 1480–1484. https://doi.org/10.1134/s1028334x06090339
Popp, B.N., Anderson, T.F., Sandberg, P.A., 1986. Geological Society of America Bulletin Brachiopods as indicators of original isotopic compositions in some Paleozoic 1262–1269. https://doi.org/10.1130/0016-7606(1986)97<1262
Rabbel, O., Mair, K., Galland, O., Grühser, C., Meier, T., 2020. Numerical Modeling of Fracture Network Evolution in Organic-Rich Shale With Rapid Internal Fluid Generation. J. Geophys. Res. Solid Earth 125. https://doi.org/10.1029/2020JB019445
Rateau, R., Schofield, N., Smith, M., 2013. The potential role of igneous intrusions on hydrocarbon migration, West of Shetland. Pet. Geosci. 19, 259–272. https://doi.org/10.1144/petgeo2012-035
Raymond, C., Murchison, G., 1988. Development of organic maturation in the thermal aureoles of sills and its relation to sediment compaction 67, 1599–1608.
Reeckmann, S.A., Mebberson, A.J., 1984. Igneous . Intrusions in North-West Canning Basin and their Impact on Oil Exploration, in: Geological Society of Australia/Petroleum Exploration Society of Australis Canning Basin Symposium. pp. 389–399.
Richardson, C.K., Rye, R.O., Wasserman, M.D., 1988. The chemical and thermal evolution of the fluids in the Cave-in-Rock fluorspar district, Illinois: stable isotope systematics at the Deardorff mine. Econ. Geol. 83, 765–783. https://doi.org/10.2113/gsecongeo.83.4.765
Robinson, M.A., McClelland, E.A., 1987. Palaeomagnetism of the Torridonian of Rhum, Scotland: evidence for limited uplift of the central intrusive complex. Earth Planet. Sci. Lett. 85, 473–487. https://doi.org/10.1016/0012-821X(87)90142-7
Rodrigues, N., Bobbold, P.R., Loseth, H., Ruffet, G., 2009. Widespread bedding-parallel veins of fibrous calcite ('beef') in a mature source rock (Vaca Muerta Fm, Neuquén Basin, Argentina): evidence for overpressure and horizontal compression. J. Geol. Soc. London. 166, 695–709. https://doi.org/10.1144/0016-76492008-111
Rodrigues, R., 1995. Geoquimica Orgânica na Bacia do Parnaíba. Universidade Federal do Rio Grande do Sul.
Rodriguez Monreal, F., Villar, H.J., Baudino, R., Delpino, D., Zencich, S., 2009. Modeling an atypical petroleum system: A case study of hydrocarbon generation, migration and accumulation related to igneous intrusions in the Neuquen Basin, Argentina. Mar. Pet. Geol. 26, 590–605. https://doi.org/10.1016/j.marpetgeo.2009.01.005
Rohrman, M., 2007. Prospectivity of volcanic basins: Trap delineation and acreage de-risking. Am. Assoc. Pet. Geol. Bull. 91, 915–939. https://doi.org/10.1306/12150606017
Rollinson, H.R., 1993. Using geochemical data: evaluation, presentation, interpretation. Pearson Education Limited.
Rye, R.O., 1993. The Evolution of Magmatic Fluids in the Epithermal Environment : The Stable Isotope Perspective. Econ. Geol. 88, 733–753.
Rye, R.O., Bethke, P.M., Wasserman, M.D., 1992. The stable isotope geochemistry of acid sulfate alteration. Econ. Geol. 87, 225–262. https://doi.org/10.2113/gsecongeo.87.2.225
Saigal, G.C., Morad, S., Bjorlykke, K., Egeberg, P.K., Aagaard, P., 1988. Diagenetic

Albitization of Detrital K-feldspar in Jurassic, Lower Cretaceous, and Tertiary Clastic Reservoir Rocks from Offshore Norway, I. Textures and Origin 58.

Sant'Anna, L.G., Clauer, N., Cordani, U.G., Riccomini, C., Velázquez, V.F., Liewig, N., 2006. Origin and migration timing of hydrothermal fluids in sedimentary rocks of the Paraná Basin, South America. Chem. Geol. 230, 1–21. https://doi.org/10.1016/j.chemgeo.2005.11.009

Santos, M.E. de C.M., Carvalho, M.S.S., 2009. Paleontologia das bacias do Parnaíba, Grajaú e São Luís. Programa Geol. do Bras. Paleontolo, 66–76.

Santos, R.V., Dantas, E.L., Oliveira, C.G. de, Alvarenga, C.J.S. de, Anjos, C.W.D. dos, Guimarães, E.M., Oliveira, F.B., 2009. Geochemical and thermal effects of a basic sill on black shales and limestones of the Permian Irati Formation. J. South Am. Earth Sci. 28, 14–24. https://doi.org/10.1016/j.jsames.2008.12.002

Schmiedel, T., Galland, O., Breitkreuz, C., 2017. Dynamics of sill and laccolith emplacement in the brittle crust: role of host rock strength and deformation mode. J. Geophys. Res. Solid Earth. https://doi.org/10.1002/2017JB014468

Schmiedel, T., Galland, O., Haug, Ø.T., Dumazer, G., Breitkreuz, C., 2019. Coulomb failure of Earth' s brittle crust controls growth , emplacement and shapes of igneous sills, saucer-shaped sills and laccoliths. Earth Planet. Sci. Lett. 510, 161–172. https://doi.org/10.1016/j.epsl.2019.01.011

Schofield, N., Holford, S., Millett, J., Brown, D., Jolley, D., Passey, S.R., Muirhead, D., Grove, C., Magee, C., Murray, J., Hole, M., Jackson, C.A.L., Stevenson, C., 2017. Regional magma plumbing and emplacement mechanisms of the Faroe-Shetland Sill Complex: implications for magma transport and petroleum systems within sedimentary basins. Basin Res. 29, 41–63. https://doi.org/10.1111/bre.12164

Schutter, S.R., 2003. Occurrences of hydrocarbons in and around igneous rocks service Permission Subscribe. Geol. Soc. London, Spec. Publ. 2003, 214, 35–68. https://doi.org/10.1144/GSL.SP.2003.214.01.03

Seal, R.R., 2006. Sulfur Isotope Geochemistry of Sulfide Minerals. Rev. Mineral. Geochemistry 61, 633–677. https://doi.org/10.2138/rmg.2006.61.12

Senger, K., Millett, J., Planke, S., Ogata, K., Eide, C.H., Festøy, M., Galland, O., Jerram, D.A., 2017. Effects of igneous intrusions on the petroleum system: a review. First Break 35, 47–56. https://doi.org/10.3997/1365-2397.2017011

Shanks, W.C., Bischoff, J.L., Rosenbauer, R.J., 1981. Seawater sulfate reduction and sulfur isotope fractionation in basaltic systems: interaction of seawater with fayalite and magnetite at 200-350oC. Geochim. Cosmochim. Acta 45, 1995–1981.

Siddiqui, S., Okasha, T.M., Funk, J.J., Al-harbi, A.M., 2003. Sca2003-40: New Representative Sample Selection Criteria for Special Core Analysis, in: Symposium A Quarterly Journal In Modern Foreign Literatures. pp. 1–11.

Siever, R., 1962. Silica Solubility, 0^0-200^0 C., and the diagenesis of siliceous sediments 70, 127–150.

Silveira, L.S., Andreola, ;, Faria, ;, Mello, A.G., Cruz, M.M., Candido, A., 2018. A influência da cimentação de Pirita em Perfis de Resistividade em Reservatórios da Formação Poti, Bacia do Parnaíba, in: IL Congresso Brasileiro de Geologia. Rio de Janeito, p. 1.

Souza, N.G.A., 2017. Influência Térmica de Intrusões Basálticas sobre as rochas siliciclásticas das formações Poti, Piauí e Pedra de Fogo, Porção Leste da Bacia do Parnaíba, Brasil. Tese Doutorado. Universidade Federal de Pernambuco.

Stagpoole, V., Funnell, R., 2001. Arc magmatism and hydrocarbon generation in the northern Taranaki Basin , New Zealand.

Stakes, D.S., 1991. Oxygen and hydrogen isotope compositions of oceanic plutonic rocks: High-temperature deformation and metamorphism of oceanic layer 3. Stable Isot. Geochemistry A Tribut. to Samuel Epstein 77–90.

Stakes, D.S., O'Neil, J.R., 1982. Mineralogy and stable isotope geochemistry of hydrothermally altered oceanic rocks. Earth Planet. Sci. Lett. 57, 285–304. https://doi.org/10.1016/0012-821X(82)90151-0

Summer, N.S., Ayalon, A., 1995. Dike intrusion into unconsolidated sandstone and the development of quartzite contact zones. J. Struct. Geol. 17, 997–1010. https://doi.org/10.1016/0191-8141(95)00009-3

Surdam, R.C., Crossey, L.J., Hagen, E.S., Heasler, H.P., 1989. Organic-inorganic and sandstone diagenesis. Am. Assoc. Pet. Geol. Bull. 73, 1–23.

Svensen, H., Planke, S., Polozov, A.G., Schmidbauer, N., Corfu, F., Podladchikov, Y.Y., Jamtveit, B., 2009. Siberian gas venting and the end-Permian environmental crisis. Earth Planet. Sci. Lett. 277, 490–500. https://doi.org/10.1016/j.epsl.2008.11.015

Sydnes, M., Fjeldskaar, W., Løtveit, I.F., Grunnaleite, I., Cardozo, N., 2017. The importance of sill thickness and timing of sill emplacement on hydrocarbon maturation. Mar. Pet. Geol. https://doi.org/10.1016/j.marpetgeo.2017.10.017

Taylor, H.P., 1977. Water / rock interactions and the origin of in granitic batholiths. Geol. Soc. Spec. Publ. London 133, 509–558.

Taylor, K.G., Macquaker, J.H.S., 2000. Early diagenetic pyrite morphology in a mudstone-dominated succession : the Lower Jurassic Cleveland Ironstone Formation , eastern England 131, 77–86.

Taylor, T.R., Giles, M.R., Hathon, L.A., Diggs, T.N., Braunsdorf, N.R., Birbiglia, G. V., Kittridge, M.G., MacAulay, C.I., Espejo, I.S., 2010. Sandstone diagenesis and reservoir quality prediction: Models, myths, and reality. Am. Assoc. Pet. Geol. Bull. 94, 1093–1132. https://doi.org/10.1306/04211009123

Tiab, D., Donaldson, E.C., 2015. Porosity and Permeability, 4th ed, Chapter 3. Porosity and Permeability in Petrophysics Theory and Practice of Measuring Reservoir Rock and Fluid Transport Properties. Elsevier Inc. https://doi.org/10.1016/b978-075067711-0/50007-4

Trosdtorf, I., Neto, J.M.M., Santos, S.F., Filho, C.V.P., Oglio, T.A.D., Galves, A.C.M., Silva, A.M., A, P.B.S., Exploração, P., República, A., Janeiro, R. De, 2018. Phanerozoic magmatism in the Parnaíba Basin : characterization of igneous bodies (well logs and 2D seismic sections), geometry , distribution and sill emplacement patterns. Geol. Soc. London 472. https://doi.org/10.1144/SP472.10 ©

Utami, W.S., Herdianita, N.R., Atmaja, R.W., 2014. The Effect of Temperature and pH on the Formation of Silica Scaling of Dieng Geothermal Field, Central Java, Indonesia., in: Thirty-Ninth Workshop on Geothermal Reservoir Engineering. Stanford, California, pp. 2–7.

Vandenbroucke, M., Behar, F., Rudkiewicz, J.L., 1999. Kinetic modelling of petroleum formation and cracking: Implications from the high pressure/high temperature Elgin Field (UK, North Sea). Org. Geochem. 30, 1105–1125. https://doi.org/10.1016/S0146-6380(99)00089-3

Vaz, P.T., Andrade, G. De, Ribeiro, J., Filho, W., Antônio, W., Travassos, S., 2007. Bacia do Parnaíba 253–263.

Wang, K., Lu, X., Chen, M., Ma, Y., Liu, K., Liu, L., Li, X., Hu, W., 2012. Numerical modelling of the hydrocarbon generation of Tertiary source rocks intruded by doleritic sills in the Zhanhua depression, Bohai Bay Basin, China. Basin Res. 24, 234–247. https://doi.org/10.1111/j.1365-2117.2011.00518.x

Wiewóra, A., Weiss, Z., 1990. CRYSTALLOCHEMICAL CLASSIFICATIONS OF PHYLLOSILICATES BASED ON THE UNIFIED SYSTEM OF PROJECTION OF CHEMICAL COMPOSITION: II. THE CHLORITE GROUP. Clay Miner. 25, 83–92. https://doi.org/doi.org/10.1180/claymin.1990.025.1.09

Williams, L.A.N.N., Parks, G.A., Crerar, D.A., 1985. Silica Diagenesis, I. Solubility Controls 55, 301–311.

Wilson, J.C., McBridge, E.F., 1988. Compaction and Porosity Evolution of Pliocene Sandstones, Ventura Basin, California. Am. Assoc. Pet. Geol. Bull. 72, 664–681.

Wilson, M.E.J., Evans, M.J., Oxtoby, N.H., Nas, D.S., Donnelly, T., Thirlwall, M., 2007. Reservoir quality , textural evolution , and origin of fault-associated dolomites 9, 1247–1272. https://doi.org/10.1306/05070706052

Wolf, S.E., Gower, L.B., 2017. Challenges and Perspectives of the Polymer-Induced Liquid-Precursor Process: The Pathway from Liquid-Condensed Mineral Precursors to

Mesocrystalline Products, New Perspectives on Mineral Nucleation and Growth. https://doi.org/10.1007/978-3-319-45669-0_3

Worden, R.H., Morad, S., 2003. Clay Mineral Cements in Sandstones. Blackwell Publishing Ltd.

Worden, R.H., Morad, S., 2000. Quartz Cementation in Sandstones, Quartz Cementation in Sandstones. Blackwell Publishing Ltd. https://doi.org/10.1002/9781444304237

Yavuz, F., Kumral, M., Karakaya, N., Karakaya, M.T., Yildirim, D.K., 2015. A Windows program for chlorite calculation and classification. Comput. Geosci. 81, 101–113. https://doi.org/10.1016/j.cageo.2015.04.011

Yuan, G., Cao, Y., Schulz, H., Hao, F., Gluyas, J., Liu, K., Yang, T., Wang, Y., Xi, K., Li, F., 2019. A review of feldspar alteration and its geological significance in sedimentary basins: From shallow aquifers to deep hydrocarbon reservoirs. Earth-Science Rev. 191, 114–140. https://doi.org/10.1016/j.earscirev.2019.02.004

Zane, A., Weiss, Z., 1998. A procedure for classifying rock-forming chlorites based on microprobe data. Rend. Fis. Acc. Lincei 9, 51–56.

Zang, W., Fyfe, W.S., 1995. Chloritization of the hydrothermally altered bedrock at the Igarap6 Bahia gold deposit , Carajas , Brazil 38, 30–38.

Zembruscki, S.G., Campos, J.N. dos P., 1988. Comportamento Geotérmico Regional e Provável Movimentação de Fluidos na Bacia do Parnaíba, Maranhão. Bol. Geociências Petrobrás 2 (2/4), 133–145.

Raw and Normalized QEMScan Data Table. Sandstones samples name are subscribed. (Continues)

QEMScan raw data (%)																				
Samples	**BG-13.8**	**BG-19.5**	**BG-38.6**	**BG-40.6**	**BG-42.7**	**BG-62.7**	**BG-64.9**	**BG-75.0**	**BG-84.8**	**BG-88.7**	**BG-88.8**	**BG-93.1**	**BG-96.3**	**BG-100.9**	**BG-106.4**	**BG-115.3**	**BG-115.6**	**BG-118.7**	**BG-121.9**	**BG-123.4**
Quartz	88.72	54.57	84.60	34.52	70.96	53.98	45.55	48.48	36.84	44.65	54.42	46.55	15.85	56.14	66.29	31.44	26.65	3.55	64.33	59.60
K-Feldspar	1.96	3.04	2.61	6.97	3.40	9.70	15.11	13.06	18.02	11.56	1.19	13.67	19.10	0.63	2.81	8.56	22.82	29.25	4.06	5.02
Plagioclase	0.01	0.01	0.01	0.04	0.03	6.62	19.63	11.57	13.70	9.91	6.36	13.38	12.40	5.70	8.73	17.67	19.42	14.74	8.97	9.65
Calcite	0.00	0.00	0.01	0.01	0.00	0.01	0.00	0.01	0.01	0.01	0.00	0.01	0.00	0.00	0.00	0.01	0.01	0.01	0.00	0.00
Dolomite	0.00	0.00	0.00	0.00	0.00	0.00	0.00	0.00	0.00	0.00	0.00	0.01	0.00	0.00	0.00	0.00	0.00	0.00	0.00	0.00
Siderite	0.02	0.00	0.49	0.00	0.07	0.00	0.01	0.00	0.09	0.42	0.03	0.05	2.59	0.02	0.07	0.04	0.00	0.00	0.01	0.63
Chlorite	0.00	0.01	0.01	0.01	0.01	0.01	0.14	0.01	0.17	5.65	0.15	1.58	0.16	0.05	0.02	2.02	5.52	0.02	0.37	0.10
Kaolinite	4.42	15.17	0.46	15.62	1.81	4.06	0.56	0.33	0.17	0.07	0.06	0.03	0.00	0.05	0.08	0.01	0.01	0.08	0.03	0.05
Smectite	0.01	0.04	0.03	1.66	0.01	0.12	0.45	0.11	0.31	0.28	1.00	0.16	0.10	0.71	0.27	0.28	0.31	0.43	0.08	0.11
Illite	0.67	1.78	0.48	9.72	0.82	2.42	4.90	2.81	5.36	4.02	17.15	2.77	7.05	10.46	3.55	16.22	14.08	25.55	0.93	0.94
Pyrite	0.00	0.00	0.01	0.01	0.01	0.01	0.01	0.01	0.06	0.02	0.00	0.03	6.36	0.00	0.03	3.01	1.80	2.69	0.02	0.01
Phosphates	0.00	0.00	0.00	0.00	0.00	0.00	0.01	0.01	0.01	0.01	0.00	0.01	0.14	0.01	0.01	0.21	0.38	0.21	0.00	0.00
Oxides	0.16	0.38	0.21	0.50	0.12	0.22	0.31	0.18	0.34	0.31	0.18	0.27	0.64	0.23	0.41	0.34	0.51	0.83	0.11	0.55
Muscovite	0.13	0.17	0.02	0.62	0.03	0.11	0.14	0.08	0.04	0.02	0.02	0.07	0.01	0.01	0.01	0.03	0.17	0.86	0.02	0.01
Biotite	0.10	0.01	0.03	0.08	0.05	0.05	1.98	0.04	1.29	3.91	0.09	1.39	9.37	0.02	0.09	1.34	2.51	16.85	0.50	0.42
Pores	2.78	21.80	7.66	18.75	21.63	19.50	3.79	21.57	15.80	10.41	15.69	15.04	19.12	17.76	15.73	16.47	1.48	2.04	18.67	18.99
Unclassified	0.98	2.98	3.34	11.45	1.02	3.12	7.30	1.68	7.65	8.08	3.61	4.81	5.88	8.17	1.82	2.30	4.26	2.73	1.81	3.76
Total	99.02	97.02	96.66	88.55	98.98	96.88	92.70	98.32	92.35	91.92	96.39	95.19	94.12	91.83	98.18	97.70	95.74	97.27	98.19	96.24
QEMScan Normalized Data (%)																				
Quartz	89.60	56.25	87.52	38.98	71.69	55.72	49.14	49.31	39.89	48.57	56.46	48.90	16.84	61.13	67.52	32.18	27.84	3.65	65.52	61.93
K-Feldspar	1.98	3.13	2.70	7.87	3.44	10.01	16.30	13.28	19.51	12.58	1.23	14.36	20.29	0.69	2.86	8.76	23.84	30.07	4.13	5.22
Plagioclase	0.01	0.01	0.01	0.05	0.03	6.83	21.18	11.77	14.83	10.78	6.60	14.06	13.17	6.21	8.89	18.09	20.28	15.15	9.14	10.03
Calcite	0.00	0.00	0.01	0.01	0.00	0.01	0.00	0.01	0.01	0.01	0.00	0.01	0.00	0.00	0.00	0.01	0.01	0.01	0.00	0.00
Dolomite	0.00	0.00	0.00	0.00	0.00	0.00	0.00	0.00	0.00	0.00	0.00	0.01	0.00	0.00	0.00	0.00	0.00	0.00	0.00	0.00
Siderite	0.02	0.00	0.51	0.00	0.07	0.00	0.01	0.00	0.10	0.46	0.03	0.05	2.75	0.02	0.07	0.04	0.00	0.00	0.01	0.65
Chlorite	0.00	0.01	0.01	0.01	0.01	0.01	0.15	0.01	0.18	6.15	0.16	1.66	0.17	0.05	0.02	2.07	5.77	0.02	0.38	0.10
Kaolinite	4.46	15.64	0.48	17.64	1.83	4.19	0.60	0.34	0.18	0.08	0.06	0.03	0.00	0.05	0.08	0.01	0.01	0.08	0.03	0.05
Smectite	0.01	0.04	0.03	1.87	0.01	0.12	0.49	0.11	0.34	0.30	1.04	0.17	0.11	0.77	0.28	0.29	0.32	0.44	0.08	0.11
Illite	0.68	1.83	0.50	10.98	0.83	2.50	5.29	2.86	5.80	4.37	17.79	2.91	7.49	11.39	3.62	16.60	14.71	26.27	0.95	0.98
Pyrite	0.00	0.00	0.01	0.01	0.01	0.01	0.01	0.01	0.06	0.02	0.00	0.03	6.76	0.00	0.03	3.08	1.88	2.77	0.02	0.01
Phosphates	0.00	0.00	0.00	0.00	0.00	0.00	0.01	0.01	0.01	0.01	0.00	0.01	0.15	0.01	0.01	0.21	0.40	0.22	0.00	0.00
Oxides	0.16	0.39	0.22	0.56	0.12	0.23	0.33	0.18	0.37	0.34	0.19	0.28	0.68	0.25	0.42	0.35	0.53	0.85	0.11	0.57
Muscovite	0.13	0.18	0.02	0.70	0.03	0.11	0.15	0.08	0.04	0.02	0.02	0.07	0.01	0.01	0.01	0.03	0.18	0.88	0.02	0.01
Biotite	0.10	0.01	0.03	0.09	0.05	0.05	2.14	0.04	1.40	4.25	0.09	1.46	9.96	0.02	0.09	1.37	2.62	17.32	0.51	0.44
Pores	2.81	22.47	7.92	21.17	21.85	20.13	4.09	21.94	17.11	11.33	16.28	15.80	20.31	19.34	16.02	16.86	1.55	2.10	19.01	19.73
Normalized Total Porcentage	99.96	99.96	99.97	99.95	99.97	99.93	99.88	99.95	99.85	99.27	99.95	99.82	98.69	99.96	99.92	99.95	99.93	99.84	99.91	99.83

QEMScan raw data (%)		
Samples	**BG-13.8**	**BG-19.5**
Quartz	88.72	54.57
K-Feldspar	1.96	3.04
Plagioclase	0.01	0.01
Calcite	0.00	0.00
Dolomite	0.00	0.00
Siderite	0.02	0.00
Chlorite	0.00	0.01
Kaolinite	4.42	15.17
Smectite	0.01	0.04
Illite	0.67	1.78
Pyrite	0.00	0.00
Phosphates	0.00	0.00
Oxides	0.16	0.38
Muscovite	0.13	0.17
Biotite	0.10	0.01
Pores	2.78	21.80
Unclassified	0.98	2.98
Total	99.02	97.02
QEMScan Normalized Data (%)		
Quartz	89.60	56.25
K-Feldspar	1.98	3.13
Plagioclase	0.01	0.01
Calcite	0.00	0.00
Dolomite	0.00	0.00
Siderite	0.02	0.00
Chlorite	0.00	0.01
Kaolinite	4.46	15.64
Smectite	0.01	0.04
Illite	0.68	1.83
Pyrite	0.00	0.00
Phosphates	0.00	0.00
Oxides	0.16	0.39
Muscovite	0.13	0.18
Biotite	0.10	0.01
Pores	2.81	22.47

Raw and Normalized QEMScan Data Table. Sandstones samples name are subscribed. (Continues)

QEMScan raw data (%)																				
Samples	**BG-127.8**	**BG-129.1**	**BG-131.9**	**BG-133.4**	**BG-138.7**	**BG-139.2**	**BG-139.9**	**BG-142.2**	**BG-145.2**	**BG-146.4**	**BG-146.8**	**BG-147.8**	**BG-149.9**	**BG-156.0**	**BG-159.4**	**BG-162.6**	**BG-166.0**	**BG-172.3**	**BG-173.5**	**BG-174.0**
Quartz	64.76	55.89	60.36	50.94	40.98	39.23	40.70	34.67	50.77	65.00	74.87	61.20	50.19	39.87	54.76	28.70	70.56	60.87	34.17	61.97
K-Feldspar	3.49	3.11	3.40	5.28	13.99	8.11	11.10	1.32	11.60	7.81	1.24	1.10	21.40	8.18	10.66	18.29	5.73	6.55	0.10	0.19
Plagioclase	9.29	17.00	4.55	15.70	21.90	20.48	10.98	0.39	9.71	6.81	7.82	4.75	15.49	4.75	9.42	11.32	5.50	8.31	12.79	3.85
Calcite	0.00	0.00	0.00	0.00	0.01	0.00	0.01	0.00	0.00	0.00	0.00	0.01	0.01	0.01	0.00	0.00	0.00	0.00	0.00	0.00
Dolomite	0.00	0.00	0.00	0.00	0.00	0.00	0.00	0.00	0.00	0.00	0.00	0.00	0.00	0.01	0.00	0.00	0.00	0.00	0.00	0.01
Siderite	0.01	0.21	0.00	0.95	0.01	0.09	0.02	0.10	0.27	0.01	0.03	0.01	0.01	1.13	0.02	0.56	0.08	0.01	0.66	2.49
Chlorite	0.14	0.93	0.39	2.23	3.06	9.27	4.50	8.19	0.31	3.11	3.99	1.57	2.21	23.10	9.78	0.47	0.11	5.62	4.95	17.71
Kaolinite	0.03	0.04	0.03	0.01	0.02	0.01	0.13	0.32	0.00	0.04	0.02	0.02	0.00	0.01	0.04	0.01	0.01	0.37	0.25	0.02
Smectite	0.06	0.19	0.23	0.22	0.68	1.12	0.18	0.02	0.03	0.10	0.18	0.04	0.03	0.36	0.16	0.17	0.02	0.25	0.25	0.30
Illite	1.15	1.69	2.66	5.74	7.12	5.85	14.90	5.35	2.47	3.86	1.15	0.90	4.03	5.41	2.82	9.53	2.05	2.90	17.46	0.69
Pyrite	0.06	0.01	0.01	0.02	2.17	1.11	0.03	13.79	0.36	0.05	1.97	0.30	0.39	0.41	0.07	0.02	0.01	0.87	0.02	0.08
Phosphates	0.00	0.00	0.01	0.00	0.15	0.14	0.11	0.06	0.01	0.01	0.01	0.07	0.54	0.17	0.09	0.13	0.06	0.11	0.23	0.11
Oxides	0.11	0.43	3.73	0.34	0.49	0.60	0.64	0.25	0.23	0.33	0.14	0.16	0.00	0.44	0.31	0.46	0.40	0.19	0.64	0.14
Muscovite	0.01	0.01	0.01	0.01	0.03	0.05	3.82	1.59	0.04	0.00	0.02	0.39	0.01	0.24	0.00	1.02	0.18	0.00	6.59	0.04
Biotite	0.30	0.32	0.48	2.39	3.48	6.88	7.08	8.26	0.30	0.12	0.94	6.47	0.32	4.22	0.06	7.85	2.25	0.06	11.22	0.66
Pores	19.23	16.68	16.32	8.90	1.85	1.65	1.80	8.02	22.86	10.93	5.88	18.16	0.92	6.62	9.19	18.58	5.42	4.62	6.36	8.34
Unclassified	1.29	3.45	7.72	6.92	3.96	5.27	3.86	17.53	0.98	1.76	1.70	4.76	0.92	4.85	2.56	2.58	7.54	9.24	4.18	3.34
Total	98.71	96.55	92.28	93.08	96.04	94.73	96.14	82.47	99.02	98.24	98.30	95.24	99.08	95.15	97.44	97.42	92.46	90.76	95.82	96.66
QEMScan Normalized Data (%)																				
Quartz	65.61	57.89	65.41	54.73	42.67	41.41	42.33	42.04	51.27	66.16	76.16	64.26	50.66	41.90	56.20	29.46	76.31	67.07	35.66	64.11
K-Feldspar	3.54	3.22	3.68	5.67	14.57	8.56	11.55	1.60	11.71	7.95	1.26	1.15	21.60	8.60	10.94	18.77	6.20	7.22	0.10	0.20
Plagioclase	9.41	17.61	4.93	16.87	22.80	21.62	11.42	0.47	9.81	6.93	7.96	4.99	15.63	4.99	9.67	11.62	5.95	9.16	13.35	3.98
Calcite	0.00	0.00	0.00	0.00	0.01	0.00	0.01	0.00	0.00	0.00	0.00	0.01	0.01	0.01	0.00	0.00	0.00	0.00	0.00	0.00
Dolomite	0.00	0.00	0.00	0.00	0.00	0.00	0.00	0.00	0.00	0.00	0.00	0.00	0.00	0.01	0.00	0.00	0.00	0.00	0.00	0.01
Siderite	0.01	0.22	0.00	1.02	0.01	0.10	0.02	0.12	0.27	0.01	0.03	0.01	0.01	1.19	0.02	0.57	0.09	0.01	0.69	2.58
Chlorite	0.14	0.96	0.42	2.40	3.19	9.79	4.68	9.93	0.31	3.17	4.06	1.65	2.23	24.28	10.04	0.48	0.12	6.19	5.17	18.32
Kaolinite	0.03	0.04	0.03	0.01	0.02	0.01	0.14	0.39	0.00	0.04	0.02	0.02	0.00	0.01	0.04	0.01	0.01	0.41	0.26	0.02
Smectite	0.06	0.20	0.25	0.24	0.71	1.18	0.19	0.02	0.03	0.10	0.18	0.04	0.03	0.38	0.16	0.17	0.02	0.28	0.26	0.31
Illite	1.17	1.75	2.88	6.17	7.41	6.18	15.50	6.49	2.49	3.93	1.17	0.94	4.07	5.69	2.89	9.78	2.22	3.20	18.22	0.71
Pyrite	0.06	0.01	0.01	0.02	2.26	1.17	0.03	16.72	0.36	0.05	2.00	0.31	0.39	0.43	0.07	0.02	0.01	0.96	0.02	0.08
Phosphates	0.00	0.00	0.01	0.00	0.16	0.15	0.11	0.07	0.01	0.01	0.01	0.07	0.55	0.18	0.09	0.13	0.06	0.12	0.24	0.11
Oxides	0.11	0.45	4.04	0.37	0.51	0.63	0.67	0.30	0.23	0.34	0.14	0.17	0.00	0.46	0.32	0.47	0.43	0.21	0.67	0.14
Muscovite	19.48	17.28	17.69	9.56	1.93	1.74	1.87	9.72	23.09	11.13	5.98	19.07	0.93	6.96	9.43	19.07	5.86	5.09	6.64	8.63
Biotite	0.01	0.01	0.01	0.01	0.03	0.05	3.97	1.93	0.04	0.00	0.02	0.41	0.01	0.25	0.00	1.05	0.19	0.00	6.88	0.04
Pores	0.30	0.33	0.52	2.57	3.62	7.26	7.36	10.02	0.30	0.12	0.96	6.79	0.32	4.44	0.06	8.06	2.43	0.07	11.71	0.68
Normalized Total Porcentage	99.93	99.96	99.89	99.62	99.90	99.85	99.85	99.83	99.94	99.94	99.96	99.91	96.44	99.77	99.94	99.68	99.91	99.97	99.86	99.94

Raw and Normalized QEMScan Data Table. Sandstones samples name are subscribed. (Continues)

QEMScan raw data (%)																				
Samples	**BG-183.2**	**BG-189.2**	**BG-190.2**	**BG-192.2**	**BG-194.1**	**BG-194.6**	**BG-202.2B**	**BG-202.5**	**BG-207.3**	**BG-215.8**	**BG-218.8**	**BG-221.1**	**BG-221.5**	**BG-223.9A**	**BG-223.9B**	**BG-223.9C**	**BG-223.9R**	**BG-225.0**	**BG-227.8**	**BG-232.2**
Quartz	51.82	66.30	58.50	55.81	80.59	75.97	34.88	15.16	42.55	45.05	60.49	19.80	64.11	3.47	26.34	74.40	5.84	23.70	26.42	41.48
K-Feldspar	0.09	0.01	3.07	0.03	0.15	0.00	12.98	1.42	3.80	0.34	2.71	0.59	9.22	0.00	0.00	0.00	0.00	0.31	1.34	0.00
Plagioclase	10.84	4.94	5.91	2.01	1.89	0.42	6.03	2.75	16.98	23.92	9.40	4.23	7.63	44.49	19.88	4.59	41.73	13.64	14.72	25.48
Calcite	0.00	0.00	0.00	0.00	0.00	0.00	0.01	0.00	0.36	0.00	0.02	0.00	0.01	0.86	0.20	3.12	1.81	0.00	0.01	0.01
Dolomite	0.19	0.00	0.00	0.00	0.00	0.00	0.01	0.00	0.01	0.00	0.01	0.00	0.01	0.07	0.01	0.11	0.12	0.01	0.00	5.19
Siderite	0.04	0.70	0.01	0.04	0.01	0.00	1.41	1.82	0.00	7.14	0.01	0.00	0.72	8.09	3.16	0.08	6.19	0.33	0.03	1.26
Chlorite	3.07	4.41	4.22	7.34	0.20	4.21	12.97	0.47	4.71	4.41	6.30	0.27	2.96	21.23	13.97	3.49	24.17	3.54	0.70	10.22
Kaolinite	0.08	0.04	0.02	0.02	0.23	0.10	0.02	0.12	0.09	0.02	0.04	9.09	0.01	0.01	0.20	0.09	0.00	1.13	1.17	0.01
Smectite	0.11	0.07	0.03	0.26	0.13	0.49	0.65	0.07	0.58	0.22	1.01	0.18	0.04	0.48	0.13	0.09	0.59	0.07	0.18	0.24
Illite	1.49	0.07	2.27	2.15	1.17	0.07	10.75	3.73	14.72	0.46	2.65	33.79	6.64	0.07	2.56	0.02	0.05	22.98	16.48	0.06
Pyrite	0.06	8.83	5.17	3.85	0.10	0.04	0.06	24.58	0.01	1.31	1.10	0.04	0.01	0.12	0.69	0.44	0.11	0.03	0.25	0.04
Phosphates	0.41	0.09	0.07	0.12	0.10	0.07	0.15	7.37	0.18	0.12	0.15	0.15	0.04	2.39	0.25	0.16	1.93	4.09	0.51	1.81
Oxides	0.27	0.36	0.30	0.10	0.30	0.09	0.41	0.70	0.40	0.10	0.16	0.46	0.29	0.37	0.11	0.28	0.37	0.44	0.76	0.52
Muscovite	0.40	0.01	0.10	0.01	0.01	0.00	0.35	0.84	0.54	0.00	0.04	9.89	0.04	0.00	0.49	0.00	0.00	4.14	5.45	0.00
Biotite	5.16	0.03	0.15	1.92	0.74	0.12	2.47	11.09	5.19	2.90	1.83	0.99	2.90	0.42	10.15	0.02	0.19	4.66	5.86	0.01
Pores	22.68	11.85	15.84	20.83	11.09	16.29	9.00	16.69	5.13	9.02	9.75	12.93	3.70	8.41	10.90	10.18	4.44	16.03	21.07	9.67
Unclassified	3.14	2.25	4.29	5.50	3.23	2.10	7.73	13.07	4.62	4.86	4.26	7.56	1.56	9.51	10.96	2.92	12.45	4.88	4.98	3.96
Total	96.86	97.75	95.71	94.50	96.77	97.90	92.27	86.93	95.38	95.14	95.74	92.44	98.44	90.49	89.04	97.08	87.55	95.12	95.02	96.04
QEMScan Normalized Data (%)																				
Quartz	53.50	67.83	61.12	59.06	83.28	77.60	37.80	17.44	44.61	47.35	63.18	21.42	65.13	3.83	29.58	76.64	6.67	24.92	27.80	43.19
K-Feldspar	0.09	0.01	3.21	0.03	0.16	0.00	14.07	1.63	3.98	0.36	2.83	0.64	9.37	0.00	0.00	0.00	0.00	0.33	1.41	0.00
Plagioclase	11.19	5.05	6.17	2.13	1.95	0.43	6.54	3.16	17.80	25.14	9.82	4.58	7.75	49.17	22.33	4.73	47.66	14.34	15.49	26.53
Calcite	0.00	0.00	0.00	0.00	0.00	0.00	0.01	0.00	0.38	0.00	0.02	0.00	0.01	0.95	0.22	3.21	2.07	0.00	0.01	0.01
Dolomite	0.20	0.00	0.00	0.00	0.00	0.00	0.01	0.00	0.01	0.00	0.01	0.00	0.01	0.08	0.01	0.11	0.14	0.01	0.00	5.40
Siderite	0.04	0.72	0.01	0.04	0.01	0.00	1.53	2.09	0.00	7.50	0.01	0.00	0.73	8.94	3.55	0.08	7.07	0.35	0.03	1.31
Chlorite	3.17	4.51	4.41	7.77	0.21	4.30	14.06	0.54	4.94	4.64	6.58	0.29	3.01	23.46	15.69	3.59	27.61	3.72	0.74	10.64
Kaolinite	0.08	0.04	0.02	0.02	0.24	0.10	0.02	0.14	0.09	0.02	0.04	9.83	0.01	0.01	0.22	0.09	0.00	1.19	1.23	0.01
Smectite	0.11	0.07	0.03	0.28	0.13	0.50	0.70	0.08	0.61	0.23	1.05	0.19	0.04	0.53	0.15	0.09	0.67	0.07	0.19	0.25
Illite	1.54	0.07	2.37	2.28	1.21	0.07	11.65	4.29	15.43	0.48	2.77	36.55	6.75	0.08	2.88	0.02	0.06	24.16	17.34	0.06
Pyrite	0.06	9.03	5.40	4.07	0.10	0.04	0.07	28.28	0.01	1.38	1.15	0.04	0.01	0.13	0.77	0.45	0.13	0.03	0.26	0.04
Phosphates	0.42	0.09	0.07	0.13	0.10	0.07	0.16	8.48	0.19	0.13	0.16	0.16	0.04	2.64	0.28	0.16	2.20	4.30	0.54	1.88
Oxides	0.28	0.37	0.31	0.11	0.31	0.09	0.44	0.81	0.42	0.11	0.17	0.50	0.29	0.41	0.12	0.29	0.42	0.46	0.80	0.54
Muscovite	0.41	0.01	0.10	0.01	0.01	0.00	0.38	0.97	0.57	0.00	0.04	10.70	0.04	0.00	0.55	0.00	0.00	4.35	5.74	0.00
Biotite	5.33	0.03	0.16	2.03	0.76	0.12	2.68	12.76	5.44	3.05	1.91	1.07	2.95	0.46	11.40	0.02	0.22	4.90	6.17	0.01
Pores	23.42	12.12	16.55	22.04	11.46	16.64	9.75	19.20	5.38	9.48	10.18	13.99	3.76	9.29	12.24	10.49	5.07	16.85	22.17	10.07
Normalized Total Porcentage	99.85	99.96	99.95	99.99	99.94	99.97	99.87	99.86	99.86	99.86	99.93	99.97	99.89	99.99	100.00	99.99	99.99	99.98	99.93	99.96

Raw and Normalized QEMScan Data Table. Sandstones samples name are subscribed.

QEMScan raw data (%)																	
Samples	**BG-234.8**	**BG-238.2**	**BG-249.9**	**BG-251.4**	**BG-259.7**	**BG-261.4**	**BG-266.7**	**BG-269.8**	**BG-278.3**	**BG-285.3**	**BG-289.6**	**BG-292.7**	**BG-297.5**	**BG-299.9**	**BG-302.4**	**BG-306.3**	**BG-306.6**
Quartz	30.87	31.79	20.21	13.19	33.22	15.95	24.67	9.26	43.34	42.33	37.47	21.02	42.46	24.86	47.55	50.72	21.45
K-Feldspar	4.68	0.00	0.17	0.56	0.21	0.56	0.00	0.65	0.73	2.80	5.08	2.28	0.04	2.30	0.00	9.16	6.50
Plagioclase	9.97	2.48	3.94	19.57	31.40	7.50	26.75	10.71	3.15	21.38	14.45	5.01	8.84	19.21	24.16	23.13	32.60
Calcite	2.43	0.03	0.11	0.04	0.48	12.55	7.79	0.57	0.01	2.94	4.08	0.00	0.07	1.09	2.65	0.73	0.21
Dolomite	0.11	0.00	0.00	0.00	0.00	0.00	0.05	0.00	0.00	0.01	0.46	0.00	0.05	0.02	0.01	0.01	0.01
Siderite	0.02	0.75	0.00	0.04	0.02	0.00	0.05	0.00	0.01	0.06	0.02	0.00	0.48	0.12	0.34	0.03	0.45
Chlorite	5.05	32.46	3.06	18.46	13.52	8.67	14.08	9.76	7.13	4.39	7.75	5.40	13.19	13.76	5.48	2.23	5.77
Kaolinite	0.58	0.00	1.77	0.95	0.10	1.39	0.03	1.67	3.13	0.01	0.03	2.03	0.71	0.51	0.01	0.01	0.05
Smectite	0.05	0.07	0.12	0.26	0.52	0.17	0.04	0.28	0.25	0.15	0.11	0.04	0.12	0.33	0.28	0.13	0.50
Illite	20.96	0.01	42.83	14.10	1.89	13.26	0.23	15.60	10.60	11.79	17.14	20.29	7.58	16.26	0.02	6.87	12.88
Pyrite	0.02	0.03	0.00	0.13	0.02	0.00	1.27	0.00	0.01	0.01	0.01	0.01	1.99	0.05	6.03	1.96	0.08
Phosphates	0.13	2.70	0.29	0.62	0.55	0.73	0.36	0.62	0.19	0.14	0.19	0.56	0.57	0.47	0.41	0.23	0.38
Oxides	0.85	0.31	0.26	0.66	0.52	0.87	0.19	0.54	0.90	0.40	0.53	1.10	0.34	0.88	0.65	0.84	1.02
Muscovite	8.33	0.00	4.83	9.49	0.35	14.33	0.00	6.13	11.18	0.01	0.21	21.64	0.17	0.00	0.00	0.13	0.32
Biotite	6.32	0.00	10.32	5.59	0.58	5.98	0.50	8.56	3.76	1.20	3.15	5.35	0.75	1.84	4.31	1.08	5.21
Pores	1.22	1.11	0.46	0.39	1.92	2.13	9.16	21.76	1.42	6.75	0.30	0.59	7.61	2.35	3.11	0.99	0.39
Unclassified	8.31	28.22	11.58	15.87	14.67	15.80	14.75	13.82	14.15	5.59	8.93	14.64	14.95	15.76	4.75	1.69	11.91
Total	91.69	71.78	88.42	84.13	85.33	84.20	85.25	86.18	85.85	94.41	91.07	85.36	85.05	84.24	95.25	98.31	88.09
QEMScan Normalized Data (%)																	
Quartz	33.67	44.29	22.86	15.68	38.93	18.94	28.94	10.74	50.48	44.84	41.14	24.63	49.92	29.51	49.92	51.59	24.35
K-Feldspar	5.10	0.00	0.19	0.67	0.25	0.67	0.00	0.75	0.85	2.97	5.58	2.67	0.05	2.73	0.00	9.32	7.38
Plagioclase	10.87	3.46	4.46	23.26	36.80	8.91	31.38	12.43	3.67	22.65	15.87	5.87	10.39	22.80	25.36	23.53	37.01
Calcite	2.65	0.04	0.12	0.05	0.56	14.90	9.14	0.66	0.01	3.11	4.48	0.00	0.08	1.29	2.78	0.74	0.24
Dolomite	0.12	0.00	0.00	0.00	0.00	0.00	0.06	0.00	0.00	0.01	0.51	0.00	0.06	0.02	0.01	0.01	0.01
Siderite	0.02	1.04	0.00	0.05	0.02	0.00	0.06	0.00	0.01	0.06	0.02	0.00	0.56	0.14	0.36	0.03	0.51
Chlorite	5.51	45.22	3.46	21.94	15.84	10.30	16.52	11.33	8.31	4.65	8.51	6.33	15.51	16.33	5.75	2.27	6.55
Kaolinite	0.63	0.00	2.00	1.13	0.12	1.65	0.04	1.94	3.65	0.01	0.03	2.38	0.83	0.61	0.01	0.01	0.06
Smectite	0.05	0.10	0.14	0.31	0.61	0.20	0.05	0.32	0.29	0.16	0.12	0.05	0.14	0.39	0.29	0.13	0.57
Illite	22.86	0.01	48.44	16.76	2.21	15.75	0.27	18.10	12.35	12.49	18.82	23.77	8.91	19.30	0.02	6.99	14.62
Pyrite	0.02	0.04	0.00	0.15	0.02	0.00	1.49	0.00	0.01	0.01	0.01	0.01	2.34	0.06	6.33	1.99	0.09
Phosphates	0.14	3.76	0.33	0.74	0.64	0.87	0.42	0.72	0.22	0.15	0.21	0.66	0.67	0.56	0.43	0.23	0.43
Oxides	0.93	0.43	0.29	0.78	0.61	1.03	0.22	0.63	1.05	0.42	0.58	1.29	0.40	1.04	0.68	0.85	1.16
Muscovite	9.08	0.00	5.46	11.28	0.41	17.02	0.00	7.11	13.02	0.01	0.23	25.35	0.20	0.00	0.00	0.13	0.36
Biotite	6.89	0.00	11.67	6.64	0.68	7.10	0.59	9.93	4.38	1.27	3.46	6.27	0.88	2.18	4.52	1.10	5.91
Pores	1.33	1.55	0.52	0.46	2.25	2.53	10.74	25.25	1.65	7.15	0.33	0.69	8.95	2.79	3.27	1.01	0.44
Normalized Total Porcentage	99.89	99.94	99.94	99.90	99.96	99.87	99.91	99.92	99.95	99.96	99.90	99.95	99.91	99.77	99.75	99.94	99.69

Appendix B. Chlorite Mineral Composition and temperature of formation plots and tables.

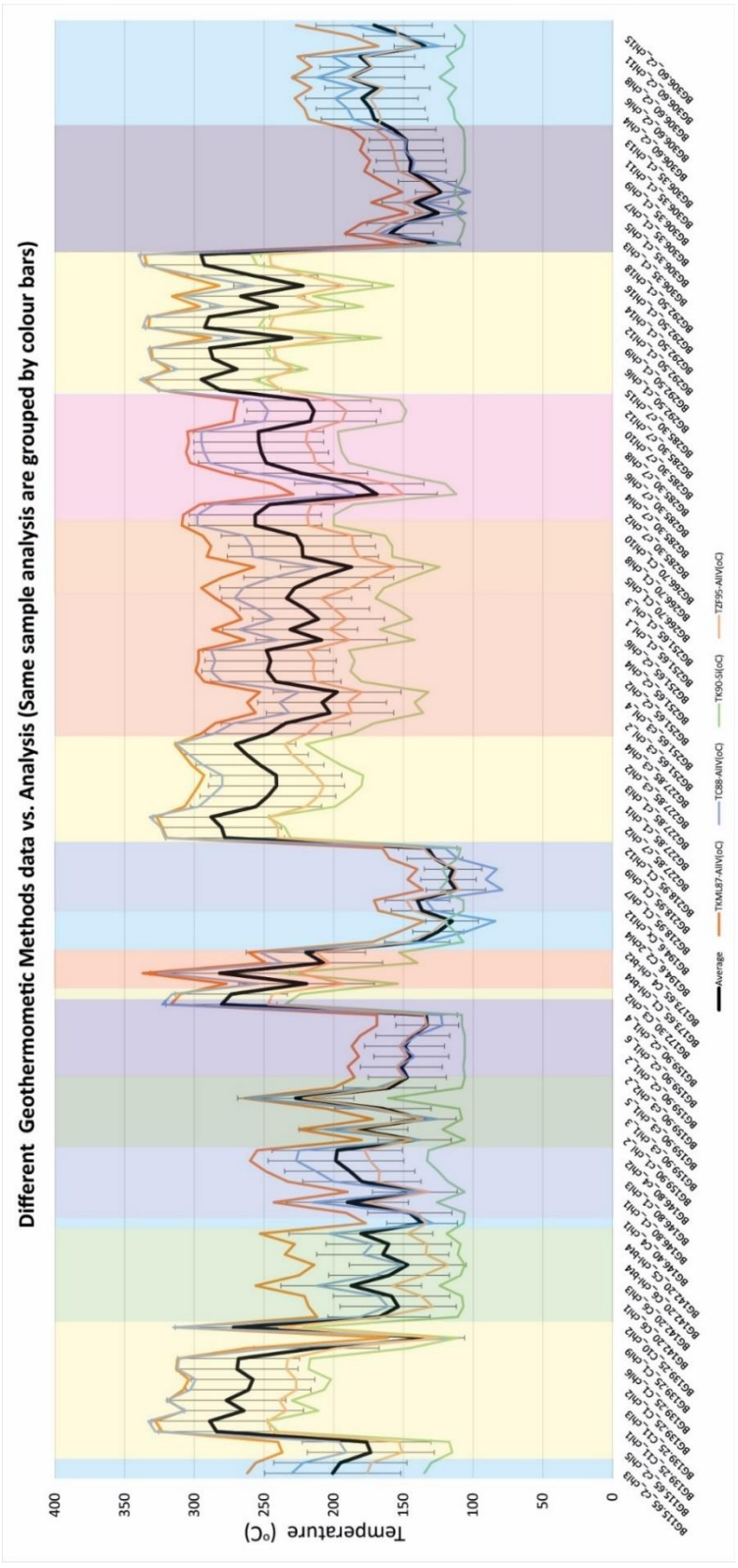

Sample Analysis vs. Temperature graph with the four selected empirical geothermometric averages and the respective chl deviation (bars). TKM87: Kranidiotis (1987); TC88: Cathelineau (1988); TK90: Kavalieris et al (1990); TZ95:Zang et al (1995).

Chlorite mineral composition in oxides, chlorite temperature of formation in four different methods and average temperature of individual analysis. TKM87: Kranidiotis (1987); TC88: Cathelineau (1988); TK90: Kavalieris et al (1990); TZ95:Zang et al (1995

Depths(m)	115.65				139.25												142.20							146.40		146.80			
Major Elements	BG115.65_c2_chl3	BG115.65_c2_chl4	BG115.65_c2_chl5	BG115.65_c2_chl6	BG139.25_C11_chl1	BG139.25_C11_chl2	BG139.25_C11_chl3	BG139.25_C1_chl1	BG139.25_C1_chl2	BG139.25_C1_chl3	BG139.25_C1_chl6	BG139.25_C1_chl7	BG139.25_C1_chl9	BG139.25_C10_chl1	BG139.25_C10_chl2	BG139.25_C10_chl3	BG142.20_C6_chl1	BG142.20_C6_chl2	BG142.20_C6_chl3	BG142.20_chl-bt2	BG142.20_C6_chl-bt4	BG142.20_C5_chl-bt4	BG142.20_C5_chl-bt5	BG146.4_C4_chl1	BG142.2_C4_chl2	BG146.80_c1_chl1	BG146.80_c1_chl2	BG146.80_c1_chl3	BG146.80_c4_chl1
SiO_2	27.599	26.178	27.147	27.745	25.262	24.907	26.029	25.048	25.187	25.57	25.819	25.962	28.656	32.63	24.799	31.21	28.279	30.016	26.754	27.51	27.747	28.695	28.68	32.027	30.818	27.415	31.822	28.557	28.201
TiO_2	0.649	0.317	0.786	0.541	0.07	0	0.093	0.102	0	0	0.084	0.027	0.117	0.1	0	0.195	0.278	0.075	0.105	0.159	0.155	0.19	0.643	0.055	0.176	0.071	0	0.036	0
Al_2O_3	15.717	14.939	13.578	15.038	18.709	18.02	17.813	18.225	17.041	17.201	18.205	18.551	16.998	13.181	17.061	15.809	13.81	14.746	13.964	13.444	14.206	14.544	15.206	16.706	15.587	13.661	14.412	13.872	14.293
B_2O_3	0	0	0	0	0	0	0	0	0	0	0	0	0	0	0	0	0	0	0	0	0	0	0	0	0	0	0	0	0
V_2O_3	0.197	0.2	0.155	0.187	0.029	0	0.056	0.004	0	0.011	0.009	0.019	0.022	0.008	0	0.004	0.088	0.061	0.05	0.039	0.043	0.12	0.105	0	0.072	0.078	0.099	0.056	0.087
Cr_2O_3	0	0.029	0	0.021	0.001	0.042	0.052	0.051	0	0.02	0.01	0	0.052	0	0	0	0.061	0.146	0	0.061	0.02	0.017	0.048	0.064	0.085	0.05	0.095	0.032	0.043
Mn_2O_3	0	0	0	0	0	0	0	0	0	0	0	0	0	0	0	0	0	0	0	0	0	0	0	0	0	0	0	0	0
Fe_2O_3	0	0	0	0	0	0	0	0	0	0	0	0	0	0	0	0	0	0	0	0	0	0	0	0	0	0	0	0	0
FeO	33.666	30.459	31.755	31.872	33.459	34.551	32.268	33.376	33.922	32.667	33.803	33.522	29.387	20.09	31.696	24.067	32.425	33.637	37.001	32.51	31.816	34.707	39.836	20.35	22.498	29.478	27.035	29.449	34.993
MnO	0.08	0.168	0.084	0.036	0.424	0.464	0.441	0.229	0.292	0.389	0.452	0.317	0.333	0.234	0.403	0.234	0.04	0.143	0.164	0.055	0.075	0.082	0.034	0.066	0.111	0.273	0.025	0.193	0.284
NiO	0	0.087	0	0.004	0	0	0	0	0	0.082	0.026	0.046	0	0.032	0.02	0	0.009	0	0	0	0.03	0.013	0.054	0.062	0.019	0.004	0	0.024	0
CoO	0	0	0	0	0	0	0	0	0	0	0	0	0	0	0	0	0	0	0	0	0	0	0	0	0	0	0	0	0
ZnO	0	0	0	0	0	0	0	0	0	0	0	0	0	0	0	0	0	0	0	0	0	0	0	0	0	0	0	0	0
CuO	0	0	0	0	0	0	0	0	0	0	0	0	0	0	0	0	0	0	0	0	0	0	0	0	0	0	0	0	0
MgO	8.012	7.896	7.738	7.375	9.785	9.61	10.821	9.378	9.252	9.916	9.778	9.745	12.544	16.992	10.627	15.502	7.099	8.507	6.141	7.293	5.464	6.273	4.914	13.63	13.08	11.881	13.12	12.351	9.232
CaO	0.085	0.109	0.116	0.065	0.046	0.028	0.07	0	0.031	0.046	0.028	0.071	0.063	0.334	0.07	0.113	0.102	0.154	0.068	0.091	0.085	0.12	0.055	0.091	0.081	0.194	0.236	0.252	0.156
BaO	0	0	0.059	0.052	0	0	0.122	0	0.009	0	0.073	0.076	0	0	0.005	0.05	0.009	0	0	0	0	0.068	0	0	0	0.129	0	0	0.033
Na_2O	0.123	0.123	0.062	0.113	0.032	0.065	0.08	0.006	0.077	0.105	0.018	0.077	0.062	0.121	0.08	0.177	0.121	0.176	0.073	0.134	0.208	0.141	0.065	0.189	0.208	0.066	0.124	0.103	0.117
K_2O	0.519	0.48	0.396	0.632	0.012	0.03	0.06	0.032	0.005	0.237	0.009	0.035	0.418	0.306	0.036	0.333	0.228	0.307	0.242	0.184	0.338	0.634	0.182	0.199	0.219	0.084	0.118	0.05	0.157
Rb2O	0	0	0	0	0	0	0	0	0	0	0	0	0	0	0	0	0	0	0	0	0	0	0	0	0	0	0	0	0
Cs_2O	0	0	0	0	0	0	0	0	0	0	0	0	0	0	0	0	0	0	0	0	0	0	0	0	0	0	0	0	0
Li_2O	0	0	0	0	0	0	0	0	0	0	0	0	0	0	0	0	0	0	0	0	0	0	0	0	0	0	0	0	0
F	0.165	0.054	0	0.055	0	0.051	0.084	0	0.071	0.032	0.107	0.082	0.05	0.155	0.061	0.175	0.084	0	0.027	0	0.05	0.051	0.097	0.028	0.119	0.024	0	0.101	0.031
Cl	0.143	0.275	0.105	0.225	0.018	0.008	0.014	0	0.007	0.03	0.012	0.033	0.05	0.091	0.027	0.087	0.033	0.038	0.008	0.015	0.074	0.046	0.016	0.028	0.032	0.017	0.051	0.015	0
H_2O	0	0	0	0	0	0	0	0	0	0	0	0	0	0	0	0	0	0	0	0	0	0	0	0	0	0	0	0	0
O=F	0.0695	0.0227	0	0.0232	0	0.0215	0.0354	0	0.0299	0.0135	0.0451	0.0345	0.0211	0.0653	0.0257	0.0737	0.0354	0	0.0114	0	0.0211	0.0215	0.0408	0.0118	0.0501	0.0101	0	0.0425	0.0131
O=Cl	0.0323	0.0621	0.0237	0.0508	0.0041	0.0018	0.0032	0	0.0016	0.0068	0.0027	0.0074	0.0113	0.0205	0.0061	0.0196	0.0074	0.0086	0.0018	0.0034	0.0167	0.0104	0.0036	0.0063	0.0072	0.0038	0.0115	0.0034	0
Total(%)	86.8533	81.2292	81.9573	83.8871	87.8429	87.7527	87.9645	86.451	85.8625	86.2858	88.3852	88.521	88.7197	84.1882	84.8532	87.8627	82.6232	87.9974	84.5838	81.4916	80.2732	85.6691	89.8905	83.4769	83.0477	83.4111	87.1255	85.0451	87.6139
H_2O	10.5839	9.9702	10.1063	10.3169	10.8542	10.7429	10.8831	10.6781	10.5035	10.6329	10.8517	10.9053	11.2352	11.1872	10.4721	11.4258	10.2035	10.949	10.1749	10.0702	9.9162	10.4751	10.7722	11.2522	10.9409	10.454	11.294	10.6923	10.7352
Tetrahedral Site																													
Al(IV)	0.9065	0.8813	0.7871	0.801	1.2098	1.2261	1.143	1.1867	1.1337	1.122	1.1606	1.1571	0.951	0.5326	1.1699	0.7544	0.6921	0.7151	0.8511	0.7249	0.6589	0.726	0.822	0.5928	0.6423	0.8595	0.6247	0.8124	0.8537
Si (apfu)	3.0935	3.1187	3.2129	3.199	2.7902	2.7739	2.857	2.8133	2.8663	2.878	2.8394	2.8429	3.049	3.4674	2.8301	3.2456	3.3079	3.2849	3.1489	3.2751	3.3411	3.274	3.178	3.4072	3.3577	3.1405	3.3753	3.1876	3.1463
Total]Tetrahedral	4.000	4.000	4.000	4.000	4.000	4.000	4.000	4.000	4.000	4.000	4.000	4.000	4.000	4.000	4.000	4.000	4.000	4.000	4.000	4.000	4.000	4.000	4.000	4.000	4.000	4.000	4.000	4.000	4.000
Octahedral Site																													
[Al(VI)	1.1697	1.2162	1.1069	1.2425	1.2255	1.1391	1.1614	1.2259	1.1518	1.1598	1.199	1.237	1.1806	1.1181	1.1249	1.1832	1.2118	1.1869	1.086	1.1614	1.3572	1.2297	1.1639	1.5018	1.3593	0.9848	1.1769	1.0126	1.0256
Total Octahedral	5.7442	5.7287	5.7083	5.6533	5.9753	6	5.9522	5.9664	5.9779	5.9457	5.964	5.9348	5.8308	5.6277	5.9987	5.7156	5.6648	5.6908	5.8358	5.7217	5.5726	5.6462	5.7423	5.495	5.5736	5.8823	5.6682	5.8481	5.8644
Octahedral vacant	0.2558	0.2713	0.2917	0.3467	0.0247	0	0.0478	0.0336	0.0221	0.0543	0.036	0.0652	0.1692	0.3723	0.0013	0.2844	0.3352	0.3092	0.1642	0.2783	0.4274	0.3538	0.2577	0.505	0.4264	0.1177	0.3318	0.1519	0.1356
Fe/(Fe+Mg)	0.7021	0.6839	0.6972	0.708	0.6573	0.6685	0.6259	0.6663	0.6729	0.6489	0.6598	0.6587	0.5679	0.3988	0.6259	0.4655	0.7193	0.6893	0.7717	0.7143	0.7656	0.7563	0.8197	0.4558	0.4911	0.5819	0.5362	0.5722	0.6801
Al/(Al+Mg+Fe2+)	0.316	0.321	0.2958	0.3201	0.3412	0.3322	0.3275	0.3389	0.3227	0.325	0.3337	0.3394	0.3164	0.2694	0.3223	0.3012	0.3015	0.2987	0.291	0.2939	0.3251	0.3088	0.306	0.3453	0.3241	0.2754	0.2871	0.2753	0.2814
#Mg	31.6	32.1	29.58	32.01	34.12	33.22	32.75	33.89	32.27	32.5	33.37	33.94	31.64	26.94	32.23	30.12	30.15	29.87	29.1	29.39	32.51	30.88	30.6	34.53	32.41	27.54	28.71	27.53	28.14
Types and Classification																													
Subgroup	tri-tri	tri-tri	tri-tri	tri-tri	tri-tri	tri-tri	tri-tri	tri-tri	tri-tri	tri-tri	tri-tri	tri-tri	tri-tri	tri-tri	tri-tri	tri-tri	tri-tri	tri-tri	tri-tri	tri-tri	tri-tri	tri-tri	tri-tri	tri-tri	tri-tri	tri-tri	tri-tri	tri-tri	tri-tri
(Zane & Weiss, 1998)	Fe chlorite	Fe chlorite	Fe chlorite	Fe chlorite	Fe chlorite	Fe chlorite	Fe chlorite	Fe chlorite	Fe chlorite	Fe chlorite	Fe chlorite	Fe chlorite	Fe chlorite	Mg chlorite	Fe chlorite	Mg chlorite	Fe chlorite	Fe chlorite	Fe chlorite	Fe chlorite	Fe chlorite	Fe chlorite	Fe chlorite	Mg chlorite	Mg chlorite	Fe chlorite	Fe chlorite	Fe chlorite	Fe chlorite
(Wiewiora & Weiss, 1990)	Chamosite	Chamosite	Chamosite	Chamosite	Chamosite	Chamosite	Chamosite	Chamosite	Chamosite	Chamosite	Chamosite	Chamosite	Chamosite	Clinochlore	Chamosite	Clinochlore	Chamosite	Chamosite	Chamosite	Chamosite	Chamosite	Chamosite	Chamosite	Clinochlore	Clinochlore	Chamosite	Chamosite	Chamosite	Chamosite
Geothermometer Methods																													
TKML87-AlIV(°C)	262	256	237	240	323	328	307	319	308	304	313	312	262	161	312	212	218	221	256	225	214	228	253	177	191	243	190	233	249
TC88-AlIV(°C)	230	222	191	196	328	333	306	320	303	299	312	311	244	110	315	181	161	168	212	171	150	172	203	129	145	215	139	200	213
TK90-Si(°C)	135	130	115	117	240	248	211	230	207	202	218	217	146	111	222	111	107	108	124	109	106	109	119	107	106	126	106	118	125
TZF95-AlIV(°C)	176	173	151	153	245	247	234	239	227	227	234	233	198	125	239	166	129	137	158	136	118	133	147	133	140	177	132	168	167
Average	201	195	174	177	284	289	265	277	261	258	269	268	213	127	272	168	154	159	188	160	147	161	181	137	146	190	142	180	189
Standard Deviation	49	48	45	46	42	42	43	43	45	44	44	44	45	21	42	37	42	42	50	43	42	45	52	25	30	44	30	42	47

Chlorite mineral composition in oxides, chlorite temperature of formation in four different methods and average temperature of individual analysis. TKM87: Kranidiotis (1987); TC88: Cathelineau (1988); TK90: Kavalieris et al (1990); TZ95:Zang et al (1995

Depths(m)	146.80		159.90														172.30			173.65	194.60					218.95					227.85
Major Elements	BG146.80_c4_chl_2	BG146.80_c4_chl_3	BG159.90_c1_chl_2	BG159.90_c1_chl_3	BG159.90_c3_chl_1_3	BG159.90_c3_chl_1_4	BG159.90_c3_chl_1_5	BG159.90_c3_chl_1_8	BG159.90_c3_chl_2_2	BG159.90_c2_chl_1_1	BG159.90_c2_chl_1_2	BG159.90_c2_chl_1_5	BG159.90_c2_chl_1_6	BG159.90_c2_chl_1_2	BG159.90_c2_chl_1_4	BG172.30_C3_chl_1	BG172.30_C3_chl_2	BG172.30_C4_chl_1	BG173.65_C4_chl_bt2	BG194.60_C2_1chl_3	BG194.60_C2_2chl_4	BG194.60_Cx_chl1_0	BG194.60_Cx_chl1_2	BG194.60_Cx_chl1_3	BG218.95_C1_chl_7	BG218.95_C1_chl_8	BG218.95_C1_chl_9	BG218.95_C1_chl_11	BG218.95_C1_chl_12	BG227.85_c7_chl_1
SiO_2	27.321	28.734	32.291	29.662	30.615	29.497	27.288	31.623	30.288	30.165	31.604	31.7	31.664	32.091	31.893	24.641	25.81	25.558	28.019	32.436	32.948	33.249	33.817	33.069	34.811	33.728	32.682	31.966	33.04	24.629
TiO_2	0.05	0.097	0.082	0	0	0	0.005	0	0	0.06	0	0.124	0.095	0.018	0.013	0	0.272	0.176	0	0.127	0	0	0.126	0.339	0.165	0.066	0.018	0	0.285	0
Al_2O_3	14.424	15.346	14.006	14.777	12.593	12.856	14.971	14.902	13.407	12.973	13.408	13.853	14.149	13.753	13.392	18.03	18.38	13.433	15.862	14.808	13.244	11.994	14.713	14.148	13.21	14.007	12.495	13.273	13.721	18.063
B_2O_3	0	0	0	0	0	0	0	0	0	0	0	0	0	0	0	0	0	0	0	0	0	0	0	0	0	0	0	0	0	0
V_2O_3	0.128	0.081	0.014	0.02	0.062	0.03	0.016	0.019	0.039	0.044	0.028	0.023	0.071	0.073	0.043	0.056	0.041	0.065	0	0.035	0.032	0.039	0.068	0.07	0.029	0.014	0	0.028	0.018	0.039
Cr_2O_3	0	0.007	0	0	0	0	0.073	0	0.001	0.055	0.032	0	0	0	0.035	0	0	0	0.022	0.047	0.012	0	0	0	0	0.033	0.022	0	0	0.002
Mn_2O_3	0	0	0.364	0.533	0.337	0.428	0.701	0.517	0.44	0.276	0.381	0.56	0.307	0.377	0.476	0	0	0	0	0.172	0.116	0	0.106	0.148	0	0	0	0	0	0
Fe_2O_3	0	0	0	0	0	0	0	0	0	0	0	0	0	0	0	0	0	0	0	0	0	0	0	0	0	0	0	0	0	0
FeO	35.531	34.384	20.421	21.241	19.41	21.105	23.48	21.337	19.202	19.792	20.498	19.896	20.235	19.499	19.246	30.327	30.126	35.502	25.83	16.989	16.701	14.2	17.8	17.207	17.678	18.317	17.333	18.527	18.706	32.555
MnO	0.196	0.164	0.364	0.533	0.337	0.428	0.701	0.517	0.44	0.276	0.381	0.56	0.307	0.377	0.476	0.129	0.082	0.04	0.379	0.172	0.116	0	0.106	0.148	0.116	0.047	0.133	0.203	0.053	0.483
NiO	0.028	0.037	0.075	0.062	0.043	0	0.028	0.032	0	0	0.049	0	0.032	0	0	0.052	0	0	0	0.01	0.031	0	0.013	0	0.029	0.015	0	0.06	0	0.082
CoO	0	0	0	0	0	0	0	0	0	0	0	0	0	0	0	0	0	0	0	0	0	0	0	0	0	0	0	0	0	0
ZnO	0	0	0	0	0	0	0	0	0	0	0	0	0	0	0	0	0	0	0	0	0	0	0	0	0	0	0	0	0	0
CuO	0	0	0	0	0	0	0	0	0	0	0	0	0	0	0	0	0	0	0	0	0	0	0	0	0	0	0	0	0	0
MgO	8.55	10.332	17.255	17.714	16.259	17.425	16.937	17.249	16.401	17.038	17.24	17.552	16.554	16.449	16.661	10.888	12.056	8.921	15.84	18.685	19.113	20.928	19.661	19.904	18.933	17.085	17.456	16.999	18.712	9.105
CaO	0.122	0.083	0.401	0.192	0.508	0.274	0.06	0.309	0.544	0.735	0.64	0.7	0.497	0.619	0.523	0	0.039	0.186	0.088	0.104	0.261	0.327	0.139	0.255	0.326	0.657	0.663	0.608	0.252	0.09
BaO	0.005	0.048	0	0	0	0	0	0.131	0.036	0.005	0	0.008	0.085	0	0.149	0	0	0	0.08	0.022	0.021	0	0	0.002	0.023	0.011	0.061	0.019	0	0.038
Na_2O	0.017	0.111	0.184	0.14	0.137	0.055	0.053	0.149	0.251	0.069	0.131	0.137	0.113	0.134	0.201	0.068	0.031	0.105	0.03	0.027	0.074	0.061	0.046	0.028	0.021	0.028	0.042	0.025	0	0.045
K_2O	0.117	0.048	0.26	0.185	0.125	0.074	0.025	0.116	0.098	0.052	0.053	0.028	0.023	0.088	0.133	0.067	0.016	0.054	0.086	0.052	0.137	0.09	0.546	0.15	0.05	0.035	0.036	0.021	0.062	0.035
Rb2O	0	0	0	0	0	0	0	0	0	0	0	0	0	0	0	0	0	0	0	0	0	0	0	0	0	0	0	0	0	0
Cs_2O	0	0	0	0	0	0	0	0	0	0	0	0	0	0	0	0	0	0	0	0	0	0	0	0	0	0	0	0	0	0
Li_2O	0	0	0	0	0	0	0	0	0	0	0	0	0	0	0	0	0	0	0	0	0	0	0	0	0	0	0	0	0	0
F	0.068	0.118	0	0	0	0	0	0	0	0	0	0	0	0	0	0	0	0	0	0.538	0.796	0.87	0.73	0.881	0.393	0.41	0.473	0.463	0.328	0
Cl	0.012	0.007	0	0.005	0.034	0.03	0.018	0.023	0.015	0	0.01	0	0.014	0.028	0.02	0.009	0.015	0.025	0.034	0	0.01	0.007	0.067	0.022	0.023	0.02	0.014	0.011	0.004	0
H_2O	0	0	0	0	0	0	0	0	0	0	0	0	0	0	0	0	0	0	0	0	0	0	0	0	0	0	0	0	0	0
O=F	0.0286	0.0497	0	0	0	0	0	0	0	0	0	0	0	0	0	0	0	0	0	0.2265	0.3352	0.3663	0.3074	0.371	0.1655	0.1726	0.1992	0.195	0.1381	0
O=Cl	0.0027	0.0016	0	0.0011	0.0077	0.0068	0.0041	0.0052	0.0034	0	0.0023	0	0.0032	0.0063	0.0045	0.002	0.0034	0.0056	0.0077	0	0.0023	0.0016	0.0151	0.005	0.0052	0.0045	0.0032	0.0025	0.0009	0
Total (%)	86.5377	89.5457	85.717	85.0629	80.4523	82.1952	84.3519	86.9188	81.1586	81.54	84.4527	85.141	84.1428	83.4997	83.2565	84.265	86.8646	84.0594	86.2623	83.9975	83.2746	81.3971	87.6155	85.9951	85.6363	84.2958	81.2257	82.0056	85.042	85.166
H_2O	10.5223	11.0289	11.4658	11.2392	10.7423	10.8402	10.9256	11.5442	10.8425	10.8679	11.26	11.3874	11.2612	11.2182	11.1616	10.5413	10.9521	10.1507	11.1153	11.21	10.9615	10.8206	11.5241	11.2583	11.5196	11.2693	10.8095	10.8372	11.3764	10.5106
Tetrahedral Site																														
Al(IV)	0.8964	0.8917	0.6223	0.8351	0.5848	0.7388	1.0058	0.7164	0.6509	0.6711	0.6345	0.6613	0.6288	0.5714	0.5746	1.1971	1.1746	0.9821	0.9791	0.6094	0.5193	0.4545	0.5909	0.6082	0.4374	0.4754	0.4513	0.5357	0.5655	1.1896
Si (apfu)	3.1036	3.1083	3.3777	3.1649	3.4152	3.2612	2.9942	3.2836	3.3491	3.3289	3.3655	3.3387	3.3712	3.4286	3.4254	2.8029	2.8254	3.0179	3.0209	3.3906	3.4807	3.5455	3.4091	3.3918	3.5626	3.5246	3.5487	3.4643	3.4345	2.8104
Total Tetrahedral	4.000	4.000	4.000	4.000	4.000	4.000	4.000	4.000	4.000	4.000	4.000	4.000	4.000	4.000	4.000	4.000	4.000	4.000	4.000	4.000	4.000	4.000	4.000	4.000	4.000	4.000	4.000	4.000	4.000	4.000
Octahedral Site																														
[Al(VI)	1.0347	1.0647	1.1043	1.0231	1.0709	0.9363	0.9303	1.1073	1.0963	1.0162	1.0482	1.0582	1.1466	1.1603	1.1205	1.2201	1.1967	0.8873	1.0364	1.2149	1.1296	1.0529	1.1572	1.102	1.1559	1.2497	1.1477	1.1596	1.1155	1.2395
Total Octahedral	5.8954	5.8752	5.6565	5.8345	5.6554	5.8384	5.9897	5.7209	5.6572	5.7084	5.685	5.6731	5.6446	5.5949	5.6067	5.9736	5.9558	5.9891	5.9478	5.6583	5.6411	5.6494	5.6459	5.6776	5.5849	5.5265	5.5628	5.6114	5.6698	5.9529
Octahedral vacant	0.1046	0.1248	0.3435	0.1655	0.3446	0.1616	0.0103	0.2791	0.3428	0.2916	0.315	0.3269	0.3554	0.4051	0.3933	0.0264	0.0442	0.0109	0.0522	0.3417	0.3589	0.3506	0.3541	0.3224	0.4151	0.4735	0.4372	0.3886	0.3302	0.0471
Fe/(Fe+Mg)	0.6998	0.6512	0.399	0.4022	0.4011	0.4046	0.4375	0.4097	0.3964	0.3945	0.4001	0.3887	0.4068	0.3994	0.3932	0.6098	0.5836	0.6906	0.4777	0.3378	0.3289	0.2757	0.3368	0.3266	0.3437	0.3756	0.3578	0.3794	0.3593	0.6673
Al/(Al+Mg+Fe2+)	0.2859	0.2906	0.2783	0.2828	0.2683	0.2578	0.2822	0.2873	0.2806	0.2671	0.2695	0.2761	0.2861	0.2842	0.2783	0.3381	0.3341	0.2692	0.2925	0.2932	0.2688	0.2471	0.2818	0.2745	0.2658	0.2881	0.2666	0.277	0.2708	0.3429
#Mg	28.59	29.06	27.83	28.28	26.83	25.78	28.22	28.73	28.06	26.71	26.95	27.61	28.61	28.42	27.83	33.81	33.41	26.92	29.25	29.32	26.88	24.71	28.18	27.45	26.58	28.81	26.66	27.7	27.08	34.29
Types and Classification																														
Subgroup	tri-tri	tri-tri	tri-tri	tri-tri	tri-tri	tri-tri	tri-tri	tri-tri	tri-tri	tri-tri	tri-tri	tri-tri	tri-tri	tri-tri	tri-tri	tri-tri	tri-tri	tri-tri	tri-tri	tri-tri	tri-tri	tri-tri	tri-tri	tri-tri	tri-tri	tri-tri	tri-tri	tri-tri	tri-tri	tri-tri
(Zane & Weiss, 1998)	Fe chlorite	Fe chlorite	Mg chlorite	Mg chlorite	Mg chlorite	Mg chlorite	Mg chlorite	Mg chlorite	Mg chlorite	Mg chlorite	Mg chlorite	Mg chlorite	Mg chlorite	Mg chlorite	Mg chlorite	Fe chlorite	Fe chlorite	Fe chlorite	Mg chlorite	Mg chlorite	Mg chlorite	Mg chlorite	Mg chlorite	Mg chlorite	Mg chlorite	Mg chlorite	Mg chlorite	Mg chlorite	Mg chlorite	Mg chlorite	Fe chlorite
(Wiewiora & Weiss, 1990)	Chamosite	Chamosite	Clinochlore	Clinochlore	Clinochlore	Clinochlore	Clinochlore	Clinochlore	Clinochlore	Clinochlore	Clinochlore	Clinochlore	Clinochlore	Clinochlore	Clinochlore	Chamosite	Chamosite	Chamosite	Clinochlore	Clinochlore	Clinochlore	Clinochlore	Clinochlore	Clinochlore	Clinochlore	Clinochlore	Clinochlore	Clinochlore	Clinochlore	Clinochlore	Chamosite
Geothermometer Methods																														
TKML87-AlIV(°C)	260	255	180	225	172	205	264	200	185	190	182	187	181	169	169	317	310	277	261	172	153	135	168	171	136	147	140	160	165	320
TC88-AlIV(°C)	227	225	138	207	126	176	262	169	148	154	142	151	141	122	123	323	316	254	253	134	105	84	128	134	79	91	83	111	120	321
TK90-Si(°C)	133	132	106	122	108	110	161	108	106	107	106	106	106	108	108	235	224	154	153	107	113	121	107	107	124	118	122	111	109	231
TZF95-AlIV(°C)	174	178	144	189	136	168	222	163	150	155	147	153	145	133	135	247	244	193	213	147	129	120	143	148	110	115	112	128	136	240
Average	199	198	142	186	136	165	227	160	147	152	144	149	143	133	134	281	274	220	220	140	125	115	137	140	112	118	114	128	133	278
Standard Deviation	49	47	26	39	23	34	42	33	28	30	27	29	27	23	22	40	40	49	43	23	18	19	22	23	21	20	21	20	21	43

Chlorite mineral composition in oxides, chlorite temperature of formation in four different methods and average temperature of individual analysis. TKM87: Kranidiotis (1987); TC88: Cathelineau (1988); TK90: Kavalieris et al (1990); TZ95:Zang et al (1995

Depths(m)	227.85									251.65														266.70						285.30
Major Elements	BG227.85 _c7_chl2	BG227.85 _c7_chl3	BG227.85 _c1_chl1	BG227.85 _c1_chl2	BG227.85 _c1_chl3	BG227.85 _c3_chl1	BG227.85 _c3_chl2	BG227.85 _c3_chl3	BG227.85 _c3_chl4	BG251.65 _c3_chl_1	BG251.65 _c3_chl_2	BG251.65 _c3_chl_3	BG251.65 _c3_chl_4	BG251.65 _c2_chl1	BG251.65 _c2_chl2	BG251.65 _c2_chl3	BG251.65 _c2_chl4	BG251.65 _c2_chl5	BG251.65 _c2_chl6	BG251.65 _c2_chl7	BG251.65 _c1_chl_1	BG251.65 _c1_chl_2	BG251.65 _c1_chl_3	BG266.70 _C1_chl1	BG266.70 _C1_chl5	BG266.70 _C1_chl7	BG266.70 _C1_chl8	BG266.70 _C1_chl9	BG266.70 _C1_chl10	BG285.30 _c7_chl1
SiO_2	24.736	24.576	25.157	24.394	25.787	25.838	25.666	25.549	25.181	26.047	27.255	28.153	27.52	28.447	26.344	26.178	26.266	25.368	28.137	26.652	28.045	27.481	26.872	23.795	24.993	25.773	24.564	24.743	24.912	24.941
TiO_2	0.058	0.174	0	0	0	0.034	0	0.097	0.058	0.031	0.049	0.044	0	0.142	0.005	0.087	0	0.226	0.208	0	0	0.03	0	0.08	0.03	0.018	0	0.171	0	0.091
Al_2O_3	18.239	18.793	15.999	13.058	15.769	15.298	16.486	16.762	16.674	16.603	17.328	13.927	14.557	13.855	17.071	17.505	17.673	16.513	15.578	17.224	15.661	15.595	16.774	13.761	13.795	12.936	14.073	13.926	14.345	16.069
B_2O_3	0	0	0	0	0	0	0	0	0	0	0	0	0	0	0	0	0	0	0	0	0	0	0	0	0	0	0	0	0	0
V_2O_3	0.055	0.024	0.064	0.009	0.014	0.031	0.036	0.077	0.1	0.108	0.015	0.027	0	0.028	0.061	0.093	0.104	0	0.052	0.036	0	0.056	0.078	0.017	0.019	0.015	0.036	0.094	0.038	0
Cr_2O_3	0	0.062	0.049	0	0.01	0	0	0	0.113	0	0.091	0.06	0	0.028	0	0	0	0.031	0.018	0.03	0	0	0	0.021	0	0.133	0.069	0.018	0	0.074
Mn_2O_3	0	0	0	0	0	0	0	0	0	0	0	0	0	0	0	0	0	0	0	0	0	0	0	0	0	0	0	0	0	0
Fe_2O_3	0	0	0	0	0	0	0	0	0	0	0	0	0	0	0	0	0	0	0	0	0	0	0	0	0	0	0	0	0	0
FeO	33.688	32.778	35.962	37.82	37.034	34.541	34.719	34.002	34.209	32.974	32.551	33.017	32.771	34.493	33.537	34.566	34.109	32.336	33.38	33.894	33.826	33.341	32.88	37.97	38.727	36.652	38.976	38.028	40.02	36.851
MnO	0.469	0.357	0.518	0.706	0.816	0.6	0.534	0.502	0.496	0.289	0.118	0.285	0.224	0.205	0.185	0.178	0.213	0.296	0.187	0.131	0.081	0.298	0.284	1.016	0.483	0.376	0.873	0.735	0.844	0.259
NiO	0.058	0	0.048	0.046	0.044	0.084	0	0	0	0.093	0.08	0.056	0	0	0.026	0.015	0	0	0	0.019	0.022	0.032	0	0	0	0.093	0.023	0	0.019	0.084
CoO	0	0	0	0	0	0	0	0	0	0	0	0	0	0	0	0	0	0	0	0	0	0	0	0	0	0	0	0	0	0
ZnO	0	0	0	0	0	0	0	0	0	0	0	0	0	0	0	0	0	0	0	0	0	0	0	0	0	0	0	0	0	0
CuO	0	0	0	0	0	0	0	0	0	0	0	0	0	0	0	0	0	0	0	0	0	0	0	0	0	0	0	0	0	0
MgO	8.662	8.813	8.405	7.79	7.788	9.737	9.368	10.006	9.876	10.23	10.592	12.373	11.538	11.593	9.603	8.681	8.722	9.46	10.771	8.608	10.897	11.128	10.294	4.414	4.707	5.617	4.268	5.403	4.628	7.569
CaO	0.101	0.162	0.04	0.109	0.053	0.01	0.038	0.087	0.093	0.071	0.066	0.096	0.021	0.026	0.076	0.104	0.084	0.087	0.072	0.096	0.05	0.082	0.056	0.191	0.164	0.29	0.402	0.206	0.17	0.118
BaO	0	0	0.042	0.028	0.021	0.006	0	0.057	0	0	0	0	0.067	0.012	0	0	0.112	0	0.126	0.089	0.009	0.02	0	0.043	0.018	0	0	0	0.155	0.063
Na_2O	0.049	0.097	0.05	0.013	0.014	0.052	0.043	0.04	0.015	0.095	0.109	0.053	0.058	0.069	0.013	0.074	0.027	0.113	0.09	0.126	0.068	0.038	0.153	0.119	0.181	0.127	0.099	0.088	0.127	0.053
K_2O	0.062	0.066	0.042	0.096	0.068	0.011	0.064	0.076	0.09	0.06	0.049	0.031	0	0.019	0.014	0.013	0	0.043	0.055	0.089	0.057	0.054	0.071	0.07	0.097	0.126	0.078	0.066	0.06	0.033
Rb2O	0	0	0	0	0	0	0	0	0	0	0	0	0	0	0	0	0	0	0	0	0	0	0	0	0	0	0	0	0	0
Cs_2O	0	0	0	0	0	0	0	0	0	0	0	0	0	0	0	0	0	0	0	0	0	0	0	0	0	0	0	0	0	0
Li_2O	0	0	0	0	0	0	0	0	0	0	0	0	0	0	0	0	0	0	0	0	0	0	0	0	0	0	0	0	0	0
F	0	0	0	0	0	0	0	0	0	0	0	0	0	0	0	0	0	0	0	0	0	0	0	0.123	0.077	0	0.074	0.06	0.073	0.005
Cl	0.015	0.016	0.031	0.051	0.033	0.017	0.037	0.008	0.031	0.008	0.013	0.028	0.013	0.004	0.025	0.027	0.009	0.012	0.019	0.017	0.03	0	0.014	0.032	0.034	0.028	0.013	0.049	0.085	0.02
H_2O	0	0	0	0	0	0	0	0	0	0	0	0	0	0	0	0	0	0	0	0	0	0	0	0	0	0	0	0	0	0
O=F	0	0	0	0	0	0	0	0	0	0	0	0	0	0	0	0	0	0	0	0	0	0	0	0.0518	0.0324	0	0.0312	0.0253	0.0307	0.0021
O=Cl	0.0034	0.0036	0.007	0.0115	0.0074	0.0038	0.0083	0.0018	0.007	0.0018	0.0029	0.0063	0.0029	0.0009	0.0056	0.0061	0.002	0.0027	0.0043	0.0038	0.0068	0	0.0032	0.0072	0.0077	0.0063	0.0029	0.0111	0.0192	0.0045
Total(%)	86.1886	85.9144	86.4	84.1085	87.4436	86.2552	86.9827	87.2612	86.929	86.6072	88.3131	88.1437	86.7661	88.9201	86.9544	87.5149	87.317	84.4823	88.6887	87.0072	88.7392	88.155	87.4728	81.593	83.2849	82.1777	83.5139	83.5507	85.4261	86.2234
H_2O	10.5841	10.6102	10.4485	10.0216	10.5209	10.5373	10.6215	10.702	10.6419	10.7041	11.0243	10.9252	10.7629	10.9713	10.7526	10.7655	10.7719	10.4424	11.011	10.7428	11.0053	10.9278	10.8615	9.4991	9.7786	9.806	9.7639	9.8385	9.9439	10.3691
Tetrahedral Site																														
Al(IV)	1.1981	1.2231	1.1154	1.0853	1.0627	1.062	1.1045	1.1374	1.1642	1.0821	1.0358	0.9115	0.9343	0.8906	1.0634	1.0855	1.0762	1.0873	0.9366	1.0258	0.9458	0.9839	1.0337	1.0165	0.9487	0.8501	0.9946	0.9963	1.0122	1.1173
Si (apfu)	2.8019	2.7769	2.8846	2.9147	2.9373	2.938	2.8955	2.8626	2.8358	2.9179	2.9642	3.0885	3.0657	3.1094	2.9366	2.9145	2.9238	2.9127	3.0634	2.9742	3.0542	3.0161	2.9663	2.9835	3.0513	3.1499	3.0054	3.0037	2.9878	2.8827
Total]Tetrahedral	4.000	4.000	4.000	4.000	4.000	4.000	4.000	4.000	4.000	4.000	4.000	4.000	4.000	4.000	4.000	4.000	4.000	4.000	4.000	4.000	4.000	4.000	4.000	4.000	4.000	4.000	4.000	4.000	4.000	4.000
Octahedral Site																														
[Al(VI)	1.2369	1.2796	1.0466	0.7535	1.0542	0.9881	1.0875	1.0761	1.0489	1.1099	1.1852	0.8893	0.9769	0.8943	1.1794	1.2114	1.2424	1.1473	1.0623	1.2396	1.0643	1.0333	1.1485	1.0169	1.0362	1.0132	1.0348	0.9962	1.0154	1.0717
Total Octahedral	5.951	5.9181	5.9968	5.9968	5.9893	5.9945	5.9929	5.9963	6	5.9555	5.8941	5.9846	5.967	5.9719	5.9273	5.9043	5.8944	5.9226	5.89	5.8548	5.9234	5.9521	5.9112	5.9425	5.9013	5.8468	5.9043	5.9367	5.9481	5.9857
Octahedral vacant	0.049	0.0819	0.0032	0.0032	0.0107	0.0055	0.0071	0.0037	0	0.0445	0.1059	0.0154	0.033	0.0281	0.0727	0.0957	0.1056	0.0774	0.11	0.1452	0.0766	0.0479	0.0888	0.0575	0.0987	0.1532	0.0957	0.0633	0.0519	0.0143
Fe/(Fe+Mg)	0.6857	0.676	0.7059	0.7314	0.7273	0.6656	0.6752	0.6559	0.6602	0.6439	0.6329	0.5995	0.6144	0.6253	0.6621	0.6908	0.6869	0.6572	0.6348	0.6884	0.6352	0.627	0.6418	0.8283	0.8219	0.7854	0.8367	0.7979	0.8291	0.732
Al/(Al+Mg+Fe2+)	0.3435	0.3533	0.3083	0.2738	0.3038	0.296	0.3112	0.313	0.3141	0.3136	0.3219	0.2627	0.2778	0.2614	0.322	0.3302	0.334	0.3211	0.2945	0.3302	0.293	0.2924	0.3157	0.2973	0.2921	0.2809	0.2986	0.2917	0.2952	0.3103
#Mg	34.35	35.33	30.83	27.38	30.38	29.6	31.12	31.3	31.41	31.36	32.19	26.27	27.78	26.14	32.2	33.02	33.4	32.11	29.45	33.02	29.3	29.24	31.57	29.73	29.21	28.09	29.86	29.17	29.52	31.03
Types and Classification																														
Subgroup	tri-tri	tri-tri	tri-tri	tri-tri	tri-tri	tri-tri	tri-tri	tri-tri	tri-tri	tri-tri	tri-tri	tri-tri	tri-tri	tri-tri	tri-tri	tri-tri	tri-tri	tri-tri	tri-tri	tri-tri	tri-tri	tri-tri	tri-tri	tri-tri	tri-tri	tri-tri	tri-tri	tri-tri	tri-tri	tri-tri
(Zane & Weiss, 1998)	Fe chlorite	Fe chlorite	Fe chlorite	Fe chlorite	Fe chlorite	Fe chlorite	Fe chlorite	Fe chlorite	Fe chlorite	Fe chlorite	Fe chlorite	Fe chlorite	Fe chlorite	Fe chlorite	Fe chlorite	Fe chlorite	Fe chlorite	Fe chlorite	Fe chlorite	Fe chlorite	Fe chlorite	Fe chlorite	Fe chlorite	Fe chlorite	Fe chlorite	Fe chlorite	Fe chlorite	Fe chlorite	Fe chlorite	Fe chlorite
(Wiewiora & Weiss, 1990)	Chamosite	Chamosite	Chamosite	Chamosite	Chamosite	Chamosite	Chamosite	Chamosite	Chamosite	Chamosite	Chamosite	Chamosite	Chamosite	Chamosite	Chamosite	Chamosite	Chamosite	Chamosite	Chamosite	Chamosite	Chamosite	Chamosite	Chamosite	Chamosite	Chamosite	Chamosite	Chamosite	Chamosite	Chamosite	Chamosite
Geothermometer Methods																														
TKM1.87-AlIV(°C)	323	327	307	302	297	293	302	308	314	295	285	256	262	253	293	299	297	297	264	287	266	273	285	295	280	257	291	288	294	309
TC88-AlIV(°C)	324	332	297	288	280	280	294	304	313	286	272	232	239	225	280	288	285	288	240	268	243	255	271	265	244	212	258	259	264	298
TK90-Si (°C)	235	247	199	188	180	179	195	208	220	187	171	136	142	132	180	188	185	189	142	167	144	155	170	164	145	124	158	158	163	200
TZF95-AlIV(°C)	240	246	220	211	207	213	221	230	235	219	210	187	190	180	213	215	214	219	189	203	191	200	209	188	174	156	182	186	187	218
Average	281	288	256	247	241	241	253	263	271	247	235	203	208	198	242	248	245	248	209	231	211	221	234	228	211	187	222	223	227	256
Standard Deviation	43	42	47	49	49	47	46	44	43	45	46	46	46	46	47	47	47	46	47	48	47	47	47	54	54	51	54	53	54	48

Chlorite mineral composition in oxides, chlorite temperature of formation in four different methods and average temperature of individual analysis. TKM87: Kranidiotis (1987); TC88: Cathelineau (1988); TK90: Kavalieris et al (1990); TZ95:Zang et al (1995

Depths(m)	285.30													292.50												306.35			
Major Elements	BG285.30_c7_chl2	BG285.30_c7_chl3	BG285.30_c7_chl4	BG285.30_c7_chl5	BG285.30_c7_chl6	BG285.30_c7_chl7	BG285.30_c7_chl8	BG285.30_c7_chl9	BG285.30_c7_chl10	BG285.30_c7_chl11	BG285.30_c7_chl12	BG285.30_c7_chl14	BG285.30_c7_chl15	BG292.50_c1_chl5	BG292.50_c1_chl6	BG292.50_c1_chl8	BG292.50_c1_chl9	BG292.50_c1_chl11	BG292.50_c1_chl12	BG292.50_c1_chl13	BG292.50_c1_chl14	BG292.50_c1_chl15	BG292.50_c1_chl16	BG292.50_c1_chl17	BG292.50_c1_chl18	BG292.50_c1_chl19	BG306.35_c1_chl3	BG306.35_c1_chl4	BG306.35_c1_chl5	BG306.35_c1_chl6
SiO_2	24.931	25.169	28.792	26.965	26.869	24.482	24.698	25.832	25.804	26.509	26.484	26.925	24.28	24.133	25.143	24.907	24.784	28.025	24.758	24.991	26.29	25.139	27.924	26.957	24.215	23.993	35.074	31.471	32.352	34.332
TiO_2	0.056	0.118	0.309	0.344	0.255	0.123	0	0.005	0	0.136	0.067	0.069	0	0.096	0.077	0.027	0.087	0.242	0.327	0.205	0	0.036	0.023	0	0.077	0.176	0.075	0.09	0.188	0.047
Al_2O_3	15.601	15.158	12.293	11.057	15.065	16.306	16.303	17.415	16.847	13.965	14.332	13.889	18.155	19.562	20.281	20.074	20.61	21.345	20.36	20.544	20.368	20.418	20.217	21.61	19.802	19.679	14.506	13.038	13.578	13.26
B_2O_3	0	0	0	0	0	0	0	0	0	0	0	0	0	0	0	0	0	0	0	0	0	0	0	0	0	0	0	0	0	0
V_2O_3	0.098	0.091	0.004	0.052	0.028	0.035	0.071	0	0.026	0.084	0	0.062	0.05	0.03	0.006	0.001	0.019	0.081	0.043	0	0	0.002	0.029	0.032	0.047	0	0	0.045	0	0.075
Cr_2O_3	0.039	0.022	0.053	0	0	0.095	0	0.116	0.075	0.074	0.097	0	0	0.001	0.01	0	0.076	0.02	0	0.043	0	0	0.043	0.087	0.041	0.051	0.012	0.023	0	0
Mn_2O_3	0	0	0	0	0	0	0	0	0	0	0	0	0	0	0	0	0	0	0	0	0	0	0	0	0	0	0	0	0	0
Fe_2O_3	0	0	0	0	0	0	0	0	0	0	0	0	0	0	0	0	0	0	0	0	0	0	0	0	0	0	0	0	0	0
FeO	36.7	34.152	34.678	36.082	34.841	34.053	35.192	34.686	36.037	34.194	33.946	32.349	34.189	33.313	32.058	34.489	32.913	31.538	33.258	33.981	30.502	31.691	32.794	32.98	33.339	33.492	15.931	17.292	16.867	14.101
MnO	0.434	0.274	0.265	0.328	0.35	0.229	0.343	0.378	0.219	0.38	0.349	0.29	0.257	0.124	0.078	0.032	0.302	0.233	0.146	0.131	0.167	0.188	0.293	0.23	0.253	0.132	0.102	0.072	0.067	0.021
NiO	0.006	0	0	0.021	0	0	0	0	0.038	0	0	0	0	0.01	0.008	0.075	0	0	0	0.021	0.044	0	0.038	0.013	0	0.008	0	0	0	0
CoO	0	0	0	0	0	0	0	0	0	0	0	0	0	0	0	0	0	0	0	0	0	0	0	0	0	0	0	0	0	0
ZnO	0	0	0	0	0	0	0	0	0	0	0	0	0	0	0	0	0	0	0	0	0	0	0	0	0	0	0	0	0	0
CuO	0	0	0	0	0	0	0	0	0	0	0	0	0	0	0	0	0	0	0	0	0	0	0	0	0	0	0	0	0	0
MgO	8.001	9.511	10.076	9.343	9.89	7.231	7.4	8.624	8.634	10.166	9.773	12.328	7.793	7.755	7.128	7.314	7.236	6.976	7.609	7.355	6.942	6.818	6.908	7.284	7.255	7.17	21.3	22.017	21.382	22.329
CaO	0.063	0.046	0.179	0.13	0.129	0.052	0.153	0.115	0.107	0.168	0.09	0.144	0.219	0.036	0.033	0.082	0.115	0.064	0.055	0.02	0.04	0.048	0.048	0.074	0.127	0.046	0.341	0.321	0.364	0.476
BaO	0	0	0.046	0	0	0	0.057	0	0.017	0	0	0	0	0.011	0.025	0.164	0	0.006	0.05	0	0.033	0	0.009	0.003	0.008	0	0	0	0.034	0.044
Na_2O	0.097	0.096	0.085	0.09	0.045	0.083	0.055	0.068	0.057	0.102	0.048	0.074	0.102	0.054	0.017	0	0.07	0.122	0.052	0.012	0.07	0.014	0.039	0.154	0.124	0.008	0.025	0.075	0.032	0.072
K_2O	0.063	0.035	0.372	0.306	0.05	0.065	0.019	0.065	0.026	0.067	0.062	0.01	0.021	0.018	0.323	0.143	0.161	0.558	0.029	0.04	0.698	0.453	0.256	0.235	0.025	0.048	0.078	0.079	0.084	0.093
Rb2O	0	0	0	0	0	0	0	0	0	0	0	0	0	0	0	0	0	0	0	0	0	0	0	0	0	0	0	0	0	0
Cs_2O	0	0	0	0	0	0	0	0	0	0	0	0	0	0	0	0	0	0	0	0	0	0	0	0	0	0	0	0	0	0
Li_2O	0	0	0	0	0	0	0	0	0	0	0	0	0	0	0	0	0	0	0	0	0	0	0	0	0	0	0	0	0	0
F	0	0	0.241	0.143	0.111	0	0.006	0.03	0.107	0.001	0.067	0.096	0.016	0.049	0.081	0	0.013	0	0.005	0.01	0	0	0	0.011	0	0.013	0.169	0.021	0.112	0.143
Cl	0	0.02	0	0.008	0	0	0.018	0	0.01	0	0.001	0.01	0.017	0.01	0.026	0.013	0.036	0.016	0.02	0.024	0.029	0.005	0.006	0.011	0.02	0.033	0.029	0.044	0.054	0.027
H_2O	0	0	0	0	0	0	0	0	0	0	0	0	0	0	0	0	0	0	0	0	0	0	0	0	0	0	0	0	0	0
O=F	0	0	0.1015	0.0602	0.0467	0	0.0025	0.0126	0.0451	0.0004	0.0282	0.0404	0.0067	0.0206	0.0341	0	0.0055	0	0.0021	0.0042	0	0	0	0.0046	0	0.0055	0.0712	0.0088	0.0472	0.0602
O=Cl	0	0.0045	0	0.0018	0	0	0.0041	0	0.0023	0	0.0002	0.0023	0.0038	0.0023	0.0059	0.0029	0.0081	0.0036	0.0045	0.0054	0.0065	0.0011	0.0014	0.0025	0.0045	0.0074	0.0065	0.0099	0.0122	0.0061
Total(%)	86.089	84.6875	87.2915	84.807	87.5863	82.754	84.3084	87.3214	87.9567	85.8456	85.2876	86.2033	85.0884	85.1791	85.254	87.3181	86.4084	89.2224	86.7054	87.3674	85.1765	84.8109	88.6256	89.6739	85.3285	84.8361	87.5643	84.5692	85.0547	84.9537
H_2O	10.3696	10.3313	10.5614	10.1143	10.671	10.0881	10.2132	10.695	10.649	10.4932	10.4156	10.6349	10.3957	10.4828	10.5813	10.7411	10.7022	11.2856	10.742	10.8027	10.7172	10.588	11.1323	11.2385	10.5185	10.437	12.0334	11.4597	11.5413	11.7471
Tetrahedral Site																														
Al(IV)	1.1166	1.0796	0.7656	0.8244	0.995	1.0894	1.1018	1.1071	1.1083	0.9703	0.9598	0.9772	1.2021	1.2458	1.1624	1.2198	1.2266	1.0228	1.2377	1.2283	1.06	1.1528	0.992	1.1253	1.2403	1.2468	0.5303	0.7125	0.6578	0.5176
Si (apfu)	2.8834	2.9204	3.2344	3.1756	3.005	2.9106	2.8982	2.8929	2.8917	3.0297	3.0402	3.0228	2.7979	2.7542	2.8376	2.7802	2.7734	2.9772	2.7623	2.7717	2.94	2.8472	3.008	2.8747	2.7597	2.7532	3.4697	3.2875	3.3422	3.4824
Total]Tetrahedral	4.000	4.000	4.000	4.000	4.000	4.000	4.000	4.000	4.000	4.000	4.000	4.000	4.000	4.000	4.000	4.000	4.000	4.000	4.000	4.000	4.000	4.000	4.000	4.000	4.000	4.000	4.000	4.000	4.000	4.000
Octahedral Site																														
[Al (VI)	1.0099	0.9932	0.862	0.7103	0.9908	1.1953	1.1528	1.1915	1.1168	0.9108	0.9793	0.8605	1.2636	1.3854	1.5351	1.4211	1.4915	1.6496	1.4395	1.4571	1.6245	1.5727	1.5746	1.5907	1.4194	1.4146	1.1609	0.8927	0.9954	1.0676
Total Octahedral	5.9996	6	5.8637	5.9744	5.9555	5.9088	5.9416	5.9264	5.9696	5.9741	5.9591	6	5.9269	5.9083	5.7762	5.8699	5.8231	5.6051	5.8533	5.8601	5.6542	5.7468	5.6762	5.7218	5.8685	5.8885	5.6352	5.8512	5.7662	5.6518
Octahedral vacant	0.0004	0	0.1363	0.0256	0.0445	0.0912	0.0584	0.0736	0.0304	0.0259	0.0409	0	0.0731	0.0917	0.2238	0.1301	0.1769	0.3949	0.1467	0.1399	0.3458	0.2532	0.3238	0.2782	0.1315	0.1115	0.3648	0.1488	0.2338	0.3482
Fe/(Fe+Mg)	0.7201	0.6683	0.6588	0.6842	0.664	0.7254	0.7274	0.6929	0.7007	0.6536	0.6608	0.5955	0.7111	0.7067	0.7162	0.7257	0.7184	0.7172	0.7103	0.7216	0.7114	0.7228	0.727	0.7175	0.7205	0.7238	0.2956	0.3058	0.3068	0.2616
Al/(Al+Mg+Fe2+)	0.303	0.2955	0.2476	0.2281	0.2881	0.3286	0.322	0.329	0.3158	0.2734	0.2822	0.2667	0.3473	0.369	0.3897	0.3731	0.388	0.4062	0.38	0.3807	0.401	0.3962	0.3871	0.3985	0.3762	0.3747	0.275	0.2453	0.2582	0.2574
#Mg	30.3	29.55	24.76	22.81	28.81	32.86	32.2	32.9	31.58	27.34	28.22	26.67	34.73	36.9	38.97	37.31	38.8	40.62	38	38.07	40.1	39.62	38.71	39.85	37.62	37.47	27.5	24.53	25.82	25.74
Types and Classification																														
Subgroup	tri-tri	tri-tri	tri-tri	tri-tri	tri-tri	tri-tri	tri-tri	tri-tri	tri-tri	tri-tri	tri-tri	tri-tri	tri-tri	tri-tri	tri-tri	tri-tri	tri-tri	tri-tri	tri-tri	tri-tri	tri-tri	tri-tri	tri-tri	tri-tri	tri-tri	tri-tri	tri-tri	tri-tri	tri-tri	tri-tri
(Zane & Weiss, 1998)	Fe chlorite	Fe chlorite	Fe chlorite	Fe chlorite	Fe chlorite	Fe chlorite	Fe chlorite	Fe chlorite	Fe chlorite	Fe chlorite	Fe chlorite	Fe chlorite	Fe chlorite	Fe chlorite	Fe chlorite	Fe chlorite	Fe chlorite	Fe chlorite	Fe chlorite	Fe chlorite	Fe chlorite	Fe chlorite	Fe chlorite	Fe chlorite	Fe chlorite	Fe chlorite	Fe chlorite	Mg chlorite	Mg chlorite	Mg chlorite	Mg chlorite
(Wiewiora & Weiss, 1990)	Chamosite	Chamosite	Chamosite	Chamosite	Chamosite	Chamosite	Chamosite	Chamosite	Chamosite	Chamosite	Chamosite	Chamosite	Chamosite	Chamosite	Chamosite	Chamosite	Chamosite	Chamosite	Chamosite	Chamosite	Chamosite	Chamosite	Chamosite	Chamosite	Chamosite	Chamosite	Chamosite	Clinochlore	Clinochlore	Clinochlore	Clinochlore
Geothermometer Methods																														
TKML87-AlIV(°C)	308	296	229	244	278	303	306	304	305	272	271	269	326	335	318	330	331	288	333	332	296	316	282	310	334	336	152	192	180	147
TC88-AlIV(°C)	298	286	185	203	258	289	293	295	295	250	247	253	325	339	312	331	333	267	337	334	279	309	257	300	337	340	109	167	150	105
TK90-Si(°C)	200	186	112	120	158	189	194	196	197	151	148	153	237	258	219	245	249	166	254	249	179	215	157	203	255	259	112	108	106	113
TZF95-AlIV(°C)	219	216	150	160	199	213	215	220	219	194	191	201	238	248	229	241	243	200	246	243	208	227	192	221	245	246	134	172	160	135
Average	256	246	169	182	223	249	252	254	254	217	214	219	282	295	270	287	289	230	293	290	241	267	222	259	293	295	127	160	149	125
Standard Deviation	47	46	43	46	48	49	48	47	47	47	48	46	44	42	46	44	43	49	43	44	48	46	50	47	43	43	17	31	27	17

Chlorite mineral composition in oxides, chlorite temperature of formation in four different methods and average temperature of individual analysis. TKM87: Kranidiotis (1987); TC88: Cathelineau (1988); TK90: Kavalieris et al (1990); TZ95:Zang et al (1995

Depths(m)	306.35								306.60									
Major Elements	BG306.35_c1_chl 7	BG306.35_c1_chl 8	BG306.35_c1_chl 9	BG306.35_c1_chl 10	BG306.35_c1_chl 11	BG306.35_c1_chl 12	BG306.35_c1_chl 13	BG306.35_c1_chl 14	BG306.60_c2_chl 4	BG306.60_c2_chl 5	BG306.60_c2_chl 6	BG306.60_c2_chl 7	BG306.60_c2_chl 8	BG306.60_c2_chl 9	BG306.60_c2_chl 11	BG306.60_c2_chl 13	BG306.60_c2_chl 15	BG306.60_c2_chl 16
SiO_2	32.281	32.853	30.499	32.427	32.469	32.679	31.674	32.049	30.155	30.524	30.398	30.374	29.49	30.504	28.878	31.901	32.284	29.222
TiO_2	0	0	0.104	0.099	0.062	0	0.075	0.1	0	0.364	0.023	0.005	0.129	0.06	0.222	0	0	0.25
Al_2O_3	12.981	12.865	12.191	13.555	13.076	13.494	12.954	13.838	13.133	13.254	13.847	13.944	13.197	13.487	12.858	12.047	13.301	13.183
B_2O_3	0	0	0	0	0	0	0	0	0	0	0	0	0	0	0	0	0	0
V_2O_3	0.049	0.053	0.042	0.001	0.004	0	0.092	0.03	0.068	0.089	0.013	0.02	0.023	0.039	0.004	0.046	0.052	0
Cr_2O_3	0	0.023	0	0.056	0	0	0.034	0	0	0.074	0.064	0.053	0	0.033	0.03	0	0	0
Mn_2O_3	0	0	0	0	0	0	0	0	0	0	0	0	0	0	0	0	0	0
Fe_2O_3	0	0	0	0	0	0	0	0	0	0	0	0	0	0	0	0	0	0
FeO	17.608	17.185	17.594	18.322	16.667	18.724	16.048	16.275	27.347	28.146	28.767	27.274	24.779	25.66	25.538	19.55	22.424	32.198
MnO	0.117	0.122	0.15	0.151	0.033	0.12	0.113	0.133	0.215	0.049	0.182	0.111	0.113	0.023	0.062	0.035	0.02	0.214
NiO	0	0	0	0	0	0	0	0	0	0	0	0	0	0	0	0	0	0
CoO	0	0	0	0	0	0	0	0	0	0	0	0	0	0	0	0	0	0
ZnO	0	0	0	0	0	0	0	0	0	0	0	0	0	0	0	0	0	0
CuO	0	0	0	0	0	0	0	0	0	0	0	0	0	0	0	0	0	0
MgO	20.589	18.842	17.51	20.272	21.717	21.011	21.543	22.178	15.783	15.817	15.748	15.152	18.396	17.294	16.377	18.901	18.857	11.609
CaO	0.34	0.483	0.442	0.242	0.34	0.304	0.253	0.223	0.218	0.19	0.18	0.167	0.193	0.139	0.202	0.633	0.32	0.152
BaO	0	0.005	0.104	0.01	0.031	0	0.003	0.09	0.036	0	0.082	0	0	0.01	0	0	0.041	0.126
Na_2O	0.014	0.053	0.095	0.071	0.061	0.072	0.031	0.043	0.042	0.075	0.117	0.063	0.1	0.028	0.052	0.107	0.043	0.083
K_2O	0.133	0.138	0.096	0.032	0.109	0.081	0.079	0.071	0.267	0.27	0.058	0.037	0.024	0.023	0.058	0.056	0.031	0
Rb2O	0	0	0	0	0	0	0	0	0	0	0	0	0	0	0	0	0	0
Cs_2O	0	0	0	0	0	0	0	0	0	0	0	0	0	0	0	0	0	0
Li_2O	0	0	0	0	0	0	0	0	0	0	0	0	0	0	0	0	0	0
F	0.084	0.007	0	0.096	0.206	0.048	0.084	0.239	0.244	0.321	0.109	0.054	0.244	0.134	0.351	0.178	0.113	0.207
Cl	0.007	0.027	0.038	0.031	0.019	0.047	0.049	0.079	0.018	0.013	0.027	0	0.022	0.01	0.013	0.031	0.047	0.034
H_2O	0	0	0	0	0	0	0	0	0	0	0	0	0	0	0	0	0	0
O=F	0.0354	0.0029	0	0.0404	0.0867	0.0202	0.0354	0.1006	0.1027	0.1352	0.0459	0.0227	0.1027	0.0564	0.1478	0.075	0.0476	0.0872
O=Cl	0.0016	0.0061	0.0086	0.007	0.0043	0.0106	0.0111	0.0178	0.0041	0.0029	0.0061	0	0.005	0.0023	0.0029	0.007	0.0106	0.0077
Total(%)	84.1661	82.647	78.8564	85.3176	84.703	86.5492	82.9856	85.2295	87.4192	89.0479	89.563	87.2313	86.6023	87.3853	84.4943	83.4031	87.4748	87.1832
H_2O	11.3984	11.2773	10.6444	11.5155	11.4608	11.6791	11.2975	11.5063	11.0715	11.2227	11.3748	11.2177	11.1093	11.2828	10.7085	11.0881	11.5368	10.7575
Tetrahedral Site																		
Al(IV)	0.616	0.5093	0.5668	0.6386	0.6328	0.6543	0.6532	0.6983	0.7687	0.7828	0.8114	0.7601	0.8506	0.7765	0.8163	0.5784	0.6631	0.7744
Si (apfu)	3.384	3.4907	3.4332	3.3614	3.3672	3.3457	3.3468	3.3017	3.2313	3.2172	3.1886	3.2399	3.1494	3.2235	3.1837	3.4216	3.3369	3.2256
Total]Tetrahedral	4.000	4.000	4.000	4.000	4.000	4.000	4.000	4.000	4.000	4.000	4.000	4.000	4.000	4.000	4.000	4.000	4.000	4.000
Octahedral Site																		
[Al(VI)	0.9878	1.1017	1.0506	1.0174	0.9654	0.974	0.9599	0.9819	0.8899	0.8636	0.9005	0.9929	0.8104	0.9032	0.8543	0.9444	0.9573	0.9406
Total Octahedral	5.7635	5.6306	5.6722	5.764	5.7763	5.7944	5.7981	5.812	5.8873	5.8766	5.911	5.852	5.9747	5.9083	5.9276	5.7273	5.8073	5.8639
Octahedral vacant	0.2365	0.3694	0.3278	0.236	0.2237	0.2056	0.2019	0.188	0.1127	0.1234	0.089	0.148	0.0253	0.0917	0.0724	0.2727	0.1927	0.1361
Fe/(Fe+Mg)	0.3242	0.3385	0.3605	0.3364	0.301	0.3333	0.2947	0.2916	0.4929	0.4996	0.5061	0.5024	0.4304	0.4543	0.4666	0.3672	0.4002	0.6087
Al/(Al+Mg+Fe2+)	0.252	0.2631	0.2604	0.2597	0.2497	0.2529	0.2511	0.2589	0.2501	0.249	0.2556	0.2658	0.2442	0.2518	0.2487	0.2418	0.2507	0.2599
#Mg	25.2	26.31	26.04	25.97	24.97	25.29	25.11	25.89	25.01	24.9	25.56	26.58	24.42	25.18	24.87	24.18	25.07	25.99
Types and Classification																		
Subgroup	tri-tri	tri-tri	tri-tri	tri-tri	tri-tri	tri-tri	tri-tri	tri-tri	tri-tri	tri-tri	tri-tri	tri-tri	tri-tri	tri-tri	tri-tri	tri-tri	tri-tri	tri-tri
(Zane & Weiss, 1998)	Mg chlorite	Mg chlorite	Mg chlorite	Mg chlorite	Mg chlorite	Mg chlorite	Mg chlorite	Mg chlorite	Mg chlorite	Mg chlorite	Fe chlorite	Fe chlorite	Mg chlorite	Mg chlorite	Mg chlorite	Mg chlorite	Mg chlorite	Fe chlorite
(Wiewiora & Weiss, 1990)	Clinochlore	Clinochlore	Clinochlore	Clinochlore	Clinochlore	Clinochlore	Clinochlore	Clinochlore	Clinochlore	Clinochlore	Chamosite	Chamosite	Clinochlore	Clinochlore	Clinochlore	Clinochlore	Clinochlore	Chamosite
Geothermometer Methods																		
TKML87-AlIV(°C)	173	151	165	178	174	181	178	188	218	221	228	216	230	216	226	168	188	227
TC88-AlIV(°C)	136	102	121	144	142	149	148	163	186	190	199	183	212	188	201	124	152	187
TK90-Si(°C)	107	114	109	106	106	106	106	107	113	114	118	112	124	114	119	108	106	113
TZF95-AlIV(°C)	150	126	136	153	156	157	160	170	166	169	174	164	190	172	179	138	153	157
Average	142	123	133	145	145	148	148	157	171	174	180	169	189	173	181	135	150	171
Standard Deviation	24	18	21	26	25	27	26	30	38	39	40	38	40	37	40	22	29	42

Appendix C. Stable Isotope Analysis

Carbon and Oxygen Isotope Analysis in Calcite

Sample	Type	$\delta^{13}C_{PDB}$ (‰)			$\delta^{18}O_{PDB}$ (‰)			$\delta^{18}O_{SMOW}$* (‰)
		Mean	Standard Deviation	Corrected	Mean	Standard Deviation	Corrected	Mean
BG-209.90	Vein	-8.15	0.02	**-8.15**	-9.71	0.07	**-9.3**	**21.28**
BG-235.80	Vein	-6.08	0.08	**-5.73**	-9.77	0.08	**-9.3**	**21.27**
BG-243.00	Vein	-5.42	0.08	**-5.12**	-11.82	0.06	**-11.42**	**19.09**
BG-260.60	Vein	-5.69	0.13	**-5.37**	-13.7	0.09	**-13.34**	**17.11**
BG-269.50	Vein	-7.75	0.03	**-7.94**	-10.62	0.08	**-9.56**	**21.01**
BG-276.30	Vein	-7.14	0.03	**-7.2**	-21.49	0.05	**-21.18**	**9.03**
BG-293.70	Vein	-8.27	0.04	**-8.58**	-9.3	0.06	**-8.15**	**22.46**
BG-302.50	Vein	-7.53	0.07	**-7.07**	-10	0.09	**-9.55**	**21.02**
BG-303.35	Vein	-6.51	0.07	**-6.43**	-10.21	0.08	**-9.12**	**21.46**
BG-306.35	Vein	-5.6	0.07	**-5.29**	-10.85	0.08	**-10.41**	**20.12**
BG-306.80	Vein	-5.97	0.04	**-5.63**	-21.1	0.05	**-20.95**	**9.26**
BG-307.00	Vein	-6.42	0.05	**-6.04**	-21.15	0.1	**-21.01**	**9.2**
BG-317.50	Amygdule	-5.69	0.06	**-5.37**	-20.19	0.08	**-20.02**	**16.94**
BG-317.50	Vein	-6.32	0.06	**-6.2**	-14.3	0.07	**-13.5**	**10.22**
BG-332.40	Aplite	-6.08	0.09	**-5.9**	-7.87	0.08	**-6.62**	**24.03**

All samples had ten counts each.

*Calculated after $\delta^{18}O_{PDB}$ value by means of the formula: $\delta^{18}OSMOW = (1.03086 \times \delta^{18}O_{PDB}) + 30.86$.

Sulfur analysis in pyrite

Sample	$\delta^{34}S$ (‰)	$\delta^{34}S$ (‰) Corrected
BG-96	2.842	6.639
BG-139	1.683	5.431
BG-140	1.165	4.891
BG-142	-4.495	-1.007
BG-148	-7.622	-4.265
BG-153	2.769	6.563
BG-190	1.92	5.678
BG-202	3.293	7.109
BG-221	4.751	8.628
BG-223	4.362	8.223
BG-283	5.153	9.047
BG-287	-0.381	3.28
BG-297	7.648	11.647
BG-302	-8.043	-4.704
BG-303	-2.254	1.329
BG-306	0.689	4.395
BG-320	-2.621	0.946

All Samples were analysed 10 times each

3. Conclusões

- As rochas reservatório da bacia do Parnaíba apresentam uma história diagenética complexa em que uma importante fase de mineralização autigênica associada a diagênese induzida pela transferência de calor e migração de fluidos hidrotermais causados por rochas ígneas intrusivas
- As alterações diagenéticas e mudanças na composição química total dos sedimentos estudados (i.e. aumento na composição modal de clorita, pirita, albita, calcita, ilita e óxidos de ferro) estão associadas a alta taxa de fluxo de fluidos hidrotermais associadas a convecção e transferência de massa.
- A presença e a ocorrência em quantidades anômalas dos minerais citados acima podem servir de indicativos de uma possível influência térmica e de transferência de massa transferência de massa por meio de fluidos hidrotermais mesmo que não haja evidências de rochas ígneas próximas.
- Análises isotópicas comparativas de enxofre em cristais de pirita hospedados em rochas sedimentares e ígneas se mostraram uma importante ferramenta para a caracterização da origem magmática de sulfetos autigênicos em rochas reservatório.
- Análises isotópicas de carbono e oxigênio em calcita também se mostraram importantes para a caracterização da origem magmática dos isótopos destes elementos, sugerindo uma contribuição secundária associada a dissolução de cimentos ou bioclastos previamente existentes.
- O uso de métodos geotermométricos empíricos de razões de Fe/Fe+Mg em análises de elementos maiores de clorita e de contextos geológicos semelhantes se mostrou válido mesmo tendo sido aplicado como único método

geotermométrico. A sua validação veio pela comparação e semelhança de resultados obtidos em trabalhos anteriores na Bacia do Parnaíba (Cardoso Jr. et al., 2020).

- A ocorrência de intervalos mineralizados com dados geotermométricos de clorita de alta temperatura em níveis alternados e limitados e associados a veios sugere que a migração convectiva de fluidos hidrotermais ocorreu pelos meios de migração mais porosos e permeáveis, sendo limitados por barreiras de baixa permeabilidade adjacentes.
- Apesar da mineralização autigênica induzida pelo fluxo de calor e hidrotermalismo associado às rochas intrusivas diminuir a porosidade e a permeabilidade das rochas reservatório (i.e. qualidade do reservatório), os valores de porosidade e permeabilidade não chegam aos limites inferiores para a produção comercial de gás natural em níveis estratigráficos semelhantes na Bacia do Parnaíba sugerido por Miranda et al. (2018).
- A presença de estruturas de sobrepressão, evidências de um sistema geoquímico aberto com mecanismo transferência de massa associado e os mínimos valores de temperatura máxima obtida pelas temperaturas de formação de clorita sugerem que hipotéticas acumulações prévias de hidrocarbonetos nas rochas reservatório estudadas poderiam ser expulsas e/ou sofrido processo de craqueamento.
- A mineralização hidrotermal de sulfetos ocorre ao longo de camadas sedimentares e veios subverticais e seu modelo genético se assemelha aos sistemas de mineralização clástica do tipo *string* de Pb-Cu-Zn. Sua ocorrência pode ser favorecida por falhas mais profundas e por camadas sedimentares com um certo mergulho, uma vez que estas duas condições favorecem a

migração de fluidos hidrotermais por células convectivas mais longas gerando uma maior extensão lateral deste tipo de mineralização.

- Estudos de petrografia, isótopos estáveis, geotermômetros em minerais autigênicos podem servir como indicadores de mudanças diagenéticas em rochas reservatório causados por hidrotermalismo associado a intrusões ígneas.
- A formação de estruturas de sobrepressão e mudança nas fases minerais dos principais minerais que preenchem o espaço porosos associadas a migração de fluidos hidrotermais sugerem importantes mudanças nos parâmetros utilizados na exploração e produção de hidrocarbonetos.